

---


Electronic Theses and Dissertations, 2004-2019

---

2010

## Response-calibration Techniques For Antenna-coupled Infrared Sensors

Peter Krenz  
*University of Central Florida*

 Part of the [Electromagnetics and Photonics Commons](#), and the [Optics Commons](#)  
Find similar works at: <https://stars.library.ucf.edu/etd>  
University of Central Florida Libraries <http://library.ucf.edu>

This Doctoral Dissertation (Open Access) is brought to you for free and open access by STARS. It has been accepted for inclusion in Electronic Theses and Dissertations, 2004-2019 by an authorized administrator of STARS. For more information, please contact [STARS@ucf.edu](mailto:STARS@ucf.edu).

---

### STARS Citation

Krenz, Peter, "Response-calibration Techniques For Antenna-coupled Infrared Sensors" (2010). *Electronic Theses and Dissertations, 2004-2019*. 4285.  
<https://stars.library.ucf.edu/etd/4285>

RESPONSE-CALIBRATION TECHNIQUES FOR  
ANTENNA-COUPLED INFRARED SENSORS

by

PETER MARTIN KRENZ  
B.S. Oklahoma State University, 2003  
M.S. University of Central Florida, 2008

A dissertation submitted in partial fulfillment of the requirement  
for the degree of Doctor of Philosophy  
in the College of Optics and Photonics: CREOL & FPCE  
at the University of Central Florida  
Orlando, Florida

Summer Term  
2010

Major Professor: Glenn D. Boreman

© 2010 Peter Martin Krenz

## **ABSTRACT**

Infrared antennas are employed in sensing applications requiring specific spectral, polarization, and directional properties. Because of their inherently small dimensions, there is significant interaction, both thermal and electromagnetic, between the antenna, the antenna-coupled sensor, and the low-frequency readout structures necessary for signal extraction at the baseband modulation frequency. Validation of design models against measurements requires separation of these effects so that the response of the antenna-coupled sensor alone can be measured in a calibrated manner. Such validations will allow confident extension of design techniques to more complex infrared-antenna configurations.

Two general techniques are explored to accomplish this goal. The extraneous signal contributions can be measured separately with calibration structures closely co-located near the devices to be characterized. This approach is demonstrated in two specific embodiments, for removal of cross-polarization effects arising from lead lines in an antenna-coupled infrared dipole, and for removal of distributed thermal effects in an infrared phased-array antenna. The second calibration technique uses scanning near-field microscopy to experimentally determine the spatial dependence of the electric-field distributions on the signal-extraction structures, and to include these measured fields in the computational electromagnetic model of the overall device. This approach is demonstrated for infrared dipole antennas which are connected to coplanar strip lines. Specific situations with open-circuit and short-circuit impedances at the termination of the lines are investigated.

*To my family and friends*

## **ACKNOWLEDGEMENTS**

Foremost, I acknowledge Dr. Glenn Boreman for his advice and patience throughout my time as a research assistant in his Infrared Systems Lab at the University of Central Florida. He has provided me with challenging research projects that allowed me to grow professionally and personally.

I would like to acknowledge Dr. Jerry Krassner at Integrity Applications Inc. for funding this research.

I have to thank the members of my committee: Dr. Pieter Kik, Dr. Patrick LiKamWa, and Dr. Brian Lail for their helpful insight into my research. I especially have to thank Dr. Brian Lail for his invaluable help with Ansoft HFSS.

All members of the IR Systems Lab have made this a great place to work and I have to thank each of them for their help and support. Dr. Brian Monacelli, Dr. Charles Middleton, and Dr. Chris Middlebrook have taught me nanolithography and how to characterize infrared detectors. Without Guy Zummo none of the lab equipment would be functioning properly and my dissertation work would have been impossible to complete. All other lab members and visitors that I had the honor to know and work with have made graduate school a unique experience: Dr. Todd du Bosq, Dr. Jeff Tharp, Dr. Tasneem Mandviwala, Dr. James Ginn, Dave Shelton, Wilson Caba, Jeff Bean, Brian Slovick, Lou Florence, Larry Schneider, Sam Wadsworth, Alex Dillard, Jeff Darchangel, Bill Franklin, Dan Mullally, Dr. Jose Manuel Lopez-Alonso, and Dr. Javier Alda. I also have to thank Dr. Ivan Divliansky for his technical help and training with the Leica electron-beam lithography tool.

Dr. Markus Raschke and Rob Olmon at the University of Washington were essential for the completion of my research, since they conducted the scattering-type scanning near-field optical microscope measurements for the experiments described in this dissertation. I have to thank Rob for explaining to me the finer details of the measurement setup.

My family, Heider, Maria, and Stefan, has been a great source of support while I am so far away. I have to thank the Bennett family, especially Joan, Wade, Tara, and Braden for giving me a home away from home and helping me transition from Germany to the USA.

Above all, I have to thank Laura for her support and love.

## TABLE OF CONTENTS

LIST OF FIGURES .....	x
LIST OF TABLES .....	xiv
LIST OF ABBREVIATIONS.....	xv
CHAPTER 1: INTRODUCTION .....	1
1.1 Bolometer .....	2
1.2 Antenna-Coupled Detectors .....	4
1.3 Near-Field Measurements .....	6
1.4 Infrared Transmission Lines.....	7
1.5 Thesis Statement .....	7
1.6 Prior Publication Disclosure.....	9
CHAPTER 2: INFRARED ANTENNA.....	10
2.1 Infrared Measurement Setup .....	11
2.2 HFSS Simulation.....	13
2.2.1 Active antenna .....	14
2.2.2 Receiving antenna.....	16
2.3 Orthogonal Dipole Antennas.....	18
2.3.1 Antenna design .....	19
2.3.2 Device fabrication and readout circuit.....	21
2.3.3 Results.....	24
2.3.4 Stokes parameter measurement .....	27



2.4 Lead-Line Response Calibration .....	28
2.4.1 Antenna design .....	30
2.4.2 Antenna response measurements without lead-line contributions.....	31
2.4.3 Device fabrication.....	34
2.4.4 Measurements and results.....	36
2.4.5 Normalized measurement conditions .....	39
CHAPTER 3: NEAR-FIELD MEASUREMENTS .....	43
3.1 s-SNOM Setup .....	45
3.2 Concept of s-SNOM Operation.....	49
3.3 HFSS Simulation of Near-Field Distribution.....	53
3.4 CPS Characterization .....	54
3.4.1 Validation of measurement approach .....	57
3.4.2 Simulation of near-field distribution along infrared CPS.....	65
3.4.3 Device fabrication.....	75
3.4.4 Measurements .....	76
3.4.5 Data analysis.....	77
3.4.6 Results.....	84
CHAPTER 4: CONCLUSION .....	86
CHAPTER 5: FUTURE WORK .....	88
APPENDIX: RADIATION PATTERN MEASUREMENT .....	90
A.1 Alignment Process for Internal z-Axis.....	92
A.2 Alignment Process for Internal x-Axis.....	95

A.3 Alignment Process for External Goniometer Position .....	97
LIST OF REFERENCES .....	101

## LIST OF FIGURES

Figure 1: Optical train for antenna characterization. ....	11
Figure 2: HFSS layout of an active antenna. ....	15
Figure 3: HFSS layout of a receiving antenna. ....	16
Figure 4: Complex input impedance of dipole antenna in direct contact with bondpads as a function of the dipole length. ....	19
Figure 5: Simulated electric field on dipole which is in direct contact with the bondpads. ....	20
Figure 6: Scanning electron micrograph of orthogonal dipole pair. ....	22
Figure 7: Schematic of on-chip and off-chip wiring. ....	23
Figure 8: Measured polarization response of orthogonal dipole pairs. ....	24
Figure 9: Normalized Stokes parameter $S_1$ obtained from measurements. ....	27
Figure 10: Predicted response of (a) dipole as a function of its length and (b) two-dipole array with varying element separation. ....	30
Figure 11: HFSS layout of a two-dipole array including lead lines (a). The highlighted yz-plane at the center of the two dipoles is where the simulated electric field is shown (b). ....	34
Figure 12: Layout of bond pad and lead line configuration. ....	35
Figure 13: Scanning electron micrographs of one-, two-, three-, and four-dipole array. ....	35
Figure 14: Geometry of a dipole illustrating the H-plane. ....	37
Figure 15: Measured H-plane radiation pattern of four-dipole array and lead-line response contribution device. Difference of these two measurements shows the distributed antenna response. ....	38

Figure 16: Measured radiation patterns without lead-line contributions of one-, two-, three-, and four-dipole arrays and corresponding simulated radiation patterns.....	38
Figure 17: Measured antenna response without lead-line contributions of one-, two-, three-, and four-dipole arrays. The simulated radiation patterns are normalized to the broadside response of the measured 4-element pattern. ....	40
Figure 18: Measured antenna response without lead-line contributions of one-, two-, three-, and four-dipole arrays after normalizing the bias current. The simulated radiation patterns are normalized to the broadside response of the measured four-element pattern.....	42
Figure 19: General s-SNOM setup for detection of TE scattered light. ....	46
Figure 20: General s-SNOM setup for detection of TM scattered light. ....	47
Figure 21: Graphical representation of dithering AFM tip in near-field. ....	50
Figure 22: HFSS setup of s-SNOM simulation .....	53
Figure 23: Cross section of a coplanar strip line.....	55
Figure 24: HFSS layout of low-frequency CPS simulation.....	59
Figure 25: Simulated magnitude of $E_y$ and $E_z$ above CPS at 10 GHz. ....	61
Figure 26: Typical mode structure on CPS.....	61
Figure 27: Magnitude of $E_y$ and $E_z$ along 10 GHz CPS.....	63
Figure 28: Comparison of magnitude and phase of $E_z$ on the two conductors of the CPS.....	63
Figure 29: Standing wave equation fitted to simulated near-field. ....	64
Figure 30: Input impedance of isolated dipole at silicon-air interface. ....	66
Figure 31: Layout of dipole-coupled CPS with open-circuit termination. ....	67
Figure 32: Layout of open-circuit-terminated CPS without dipole antenna.....	68

Figure 33: Simulated magnitude of $E_z$ above one conductor of the open-circuit terminated dipole- and non-dipole-coupled CPS.....	69
Figure 34: Simulated and fitted standing wave on open-circuited CPS. ....	69
Figure 35: Layout of dipole-coupled CPS with short-circuit termination. ....	70
Figure 36: Layout of short-circuit-terminated CPS without dipole antenna.....	70
Figure 37: Simulated magnitude of $E_z$ above one conductor of the dipole- and non-dipole-coupled short-circuit terminated CPS. ....	71
Figure 38: Fitted standing wave on short-circuited CPS. ....	73
Figure 39: AFM topography of dipole-coupled CPS with (a) open- and (c) short-circuit load. Identically terminated transmission lines without dipole antenna (b) and (d).....	76
Figure 40: Measured s-SNOM signal on dipole-couple CPS with (a) open- and (c) short-circuit load and corresponding transmission lines without antenna (b) and (d). ....	76
Figure 41: Measured s-SNOM signal on both conductors of dipole-coupled CPS with open-circuit load. ....	78
Figure 42: Analytical interferometer output fitted to measured s-SNOM signal. ....	80
Figure 43: Measured and simulated near-field distribution along open-circuit terminated CPS. ....	81
Figure 44: Analytical s-SNOM signal fitted to measurements on dipole-coupled CPS with short-circuit termination. ....	82
Figure 45: Measured and simulated near-field distribution along short-circuit terminated CPS. ....	83
Figure 46: Top view of the goniometer indicating the location of the device, axis of rotation, and the laser beam. ....	92
Figure 47: Radiation pattern measurement of misaligned device in x and z. ....	93

Figure 48: Geometrical representation of misaligned device in x and z is shown for  $\theta = \pm \theta_a^\circ$  and  $\theta = 0^\circ$  ..... 93

Figure 49: Position along internal x-axis to maximize response of device is determined for (a)  $\theta = 40^\circ$  and (b)  $\theta = -40^\circ$  ..... 94

Figure 50: Adjusting (a) x and (b) z position of device. .... 95

Figure 51: Radiation pattern measurement of misaligned device in x ..... 96

Figure 52: Geometrical representation of a misaligned device in the x direction is shown for  $\theta = \pm \theta_a^\circ$  and  $\theta = 0^\circ$  ..... 96

Figure 53: (a) Determine position along internal x-axis to maximize response of device at  $\theta = 0^\circ$  and (b) adjusting device's location to coincide with axis of rotation ..... 97

Figure 54: External goniometer adjustment (a) along external x-axis and (b) resulting irradiance illuminating device during measurement ..... 98

Figure 55: (a) External goniometer adjustment along external z-axis and (b) resulting irradiance illuminating device during measurement (b) ..... 99

## LIST OF TABLES

Table 1: Room temperature TCR values of gold and nickel. ....	4
Table 2: Dielectric constants.....	14
Table 3: Parameters obtained by fitting Eq (5) to measured data.....	25
Table 4: Values of $\Re_0$ and $\Re_{\text{offset}}$ calculated from measured responses of individual dipoles.....	26
Table 5: Dimensions of fabricated dipole arrays. ....	36
Table 6: Parameters characterizing the 10 GHz CPS. ....	64
Table 7: Parameters determined by fitting standing-wave equation to simulation results. ....	73
Table 8: Fitted standing wave parameter to demonstrate finite extent of load.....	75
Table 9: Fitting parameters of dipole-coupled open-circuit terminated CPS. ....	80
Table 10: Fitting parameters of dipole-coupled short-circuit terminated CPS.....	83
Table 11: Parameters characterizing the CPS.....	84

## LIST OF ABBREVIATIONS

AFM	atomic force microscope
BCB	benzocyclobutene
BS	beam splitter
CO <sub>2</sub>	carbon dioxide
CPS	coplanar strip line
FEM	finite element method
IPA	isopropanol alcohol
IR	infrared
MCT	mercury-cadmium-telluride
MIBK	methyl-isobutyl-ketone
NDF	neutral density filter
PEC	perfect electric conductor
PML	perfectly matched layer
RF	radio frequency
s-SNOM	scattering-type scanning near-field optical microscope
SSE	sum square of errors
TCR	temperature coefficient of resistance
VNA	vector network analyzer



## CHAPTER 1: INTRODUCTION

Infrared (IR) radiation was discovered by the astronomer Sir William Herschel in 1800 [1]. Using a Newtonian telescope he gathered solar radiation and separated its spectrum using a prism to experiment with the invisible radiation beyond the red end of the visible spectrum. Using thermometers and mirrors with aperture stops, he proved that this invisible part of the spectrum obeys the laws of reflection and refraction.

For the following 120 years, all detectors that were developed to measure infrared radiation were thermal detectors. For this type of detector, the incident radiation changes the temperature of the device and some temperature-dependent property is measured. The thermometer used by Herschel in his experiments is the earliest type of thermal detector and its observed temperature-dependent property is the change in volume of the mercury inside the thermometer. Other types of thermal detectors include thermopiles, which create a voltage due to thermoelectric effect, Golay cells, which increase the pressure of gas in a confined space, bolometers, which change their electrical resistance, and pyroelectrics, which change their dipole moment [2]. These types of detectors can operate at room temperature, but their response is slow since their thermal mass has to experience a rise and fall in temperature.

The photon detector, which is composed of semiconductors, was developed during World War I and World War II. The mode of operation of these detectors is fundamentally different from the thermal detectors. The incident radiation is absorbed and causes a change in the free carrier density in the semiconductor, which is then measured. These detectors were developed to operate in the atmospheric windows from 3 - 5  $\mu\text{m}$  and 8 - 12  $\mu\text{m}$ .

A change in the free carrier-density of a photon detector due to incident radiation occurs quickly and thus photon detectors operate much faster than the thermal detectors. A drawback of the photon detectors is that ambient temperature can thermally excite electrons into the conduction band. The detector has to be cryogenically cooled in order to detect photo-generated electrons at long wavelengths [3].

The work in the experiments presented herein concentrates on uncooled bolometers operating at the main emission line of the carbon dioxide (CO<sub>2</sub>) laser at 10.6  $\mu\text{m}$ .

## **1.1 Bolometer**

The bolometer was developed by the astronomer Samuel Langley in 1880 [4]. He used a parallel connection of several thin iron strips to form the bolometer, which was electrically connected to form a balanced Wheatstone bridge. Incident radiation caused the iron strips to heat up and increased their resistance, which caused the bridge to be unbalanced. The resulting current flow was measured with a galvanometer.

The bolometer consists of several fundamental elements [5]: radiation absorber, thermometer, heat sink, supporting substrate, and thermal links connecting these elements. The radiation absorber has an appropriate size to intercept the incident radiation to be measured and a large absorptance over the frequency range of interest, which implies that the incident radiation is absorbed rather than reflected or transmitted. Ideally it also has a low heat capacity, such that not a lot of radiation needs to be absorbed to cause a change in its temperature. The thermometer is the element that measures the change in temperature due to the incident radiation. It is thermally attached to the radiation absorber and it also has a low heat capacity and a high

temperature dependence of its electrical resistance. The heat sink remains at a stable temperature. When the bolometer is not illuminated, it will return to the temperature of the heat sink. Thermal links connect the thermally active portions of the bolometer to the heat sink. These links have a low thermal conductance and thus do not easily conduct heat and they keep the active elements of the bolometer thermally isolated. The substrate that mechanically supports the bolometer has a low heat capacity and large thermal conductivity. During the bolometer operation, the substrate will remain at a constant temperature in order not to affect the temperature of the bolometer. The mechanical support structures for the thermally active portion of the bolometer must have a low thermal conductance to keep the active elements of the bolometer isolated.

A bolometer design can combine several of these functions into single elements. The equation relating a change in temperature,  $\Delta T$ , to a change in resistance is expressed as [2]

$$R = R_0(1 + \alpha\Delta T). \quad (1)$$

$R_0$  is the resistance of the bolometer when it is not illuminated. The temperature coefficient of resistance (TCR) is given as

$$\alpha = \frac{1}{R_d} \frac{dR_d}{dT_d}, \quad (2)$$

where  $R_d$  is the resistance of the detector and  $T_d$  is its temperature. In the following experiments gold and nickel are used as bolometers. Their TCR values at room temperature [6] are listed in Table 1. Nickel has a larger TCR than gold, making it the preferred candidate material for a bolometer. Gold is used as bolometer only to simplify the fabrication process.

Table 1: Room temperature TCR values of gold and nickel.

Material	TCR (%/K)
gold	0.37
nickel	0.55

The bolometers are operated by passing a constant current through the device and monitoring the output voltage. Absorbed incident radiant power produces a change of temperature within the material, which in turn produces a change in resistance. The voltage responsivity of a bolometer is expressed as

$$\mathfrak{R}_v = \frac{i_{\text{bias}} R \alpha \eta}{G [1 + \omega^2 \tau_{\text{th}}^2]^{1/2}}. \quad (3)$$

The bias current  $i_{\text{bias}}$  flows through the bolometer with resistance  $R$  and a TCR,  $\alpha$ .  $\eta$  is the optical absorption coefficient,  $G$  is the thermal conductance of the bolometer, and  $\tau_{\text{th}}$  is its time constant defined as  $\tau_{\text{th}} = C/G$  where  $C$  is the bolometer's heat capacity. The incident radiation is modulated at the angular frequency  $\omega$ .

Commercially available bolometers in focal plane arrays are commonly sized to fill up an entire pixel, which can range from  $12 \times 12 \mu\text{m}$  up to  $50 \times 50 \mu\text{m}$  [3]. Reducing the size of the bolometer would decrease its thermal mass, which would facilitate a faster response time. This comes at the price that the bolometer intercepts a smaller amount of the incident radiation.

## 1.2 Antenna-Coupled Detectors

An antenna is the transitional structure that converts guided electromagnetic energy to radiation propagating in free space or vice versa [7]. The guiding structure can be characterized

by an effective index of refraction,  $n_{\text{eff}}$ . At the terminals of the antenna, where it is connected to the guiding structure, the guided wave encounters a different index of refraction,  $n = \sqrt{\epsilon_r \mu_r}$ . In radio frequency (RF) designs the terminals of the antenna are not characterized by its index of refraction, but by its impedance,  $Z = \sqrt{\mu_0 \mu_r / \epsilon_0 \epsilon_r}$ . The antenna can be thought of as an index matching structure between the guiding structure and free space.

An antenna can be used to transmit or receive radiation. A graphical representation of how well the antenna receives or transmits radiation in any direction is defined as its radiation pattern. By properly designing an antenna, it can be sensitive to only certain wavelengths and polarization states. The measurement of a radiation pattern, or its spectral or polarization dependence, are methods of characterizing the antenna and validating its design.

In common bolometer designs, the same element is used to intercept and to detect radiation. These functions can be separated by coupling the bolometer to an antenna. The antenna provides a sufficient capture cross section for the radiation, while detector itself can be made very small [8]. Coupling an antenna to an infrared detector was first demonstrated by characterizing a cat-whisker diode. This diode uses a thin wire with a sharpened tip, which is pressed into contact with the flat surface of another metal that is coated with a native oxide layer. This configuration forms a metal-oxide-metal diode. The polarization dependence [9], radiation pattern [10], and source impedance [11] were measured and showed agreement with RF antenna theory.

The reduced size of the bolometer results in a faster response time. Coupling the small bolometer, which is referred to as a microbolometer [12], to an antenna results in a detector that can be designed to meet certain directional, spectral, and polarization requirements.

### 1.3 Near-Field Measurements

In optical microscopy, a sample of interest is illuminated and the scattered light is collected by the microscope objective. The resolution limit is caused by only the propagating waves contributing to the image formation, resulting in a diffraction limited image [13]. By measuring the evanescent near-field component, the resolution limit of the image can be reduced. This can be accomplished by using a sharp metal tip [14, 15] to locally scatter the evanescent field and converting it to a propagating wave. The near-field measurement conducted in the described experiments use a scattering-type scanning near-field optical microscope (s-SNOM), where an atomic force microscope (AFM) is used to scan a sharp tip across an illuminated sample. The s-SNOM measurements create a high resolution map of the electric field distribution in close proximity,  $\sim 20$  nm, of the investigated structure.

Since the s-SNOM measurement images the evanescent near-field on a structure, samples that interact strongly with incident radiation, such as antennas [16], are of interest. Optical antennas have been extensively studied, since they convert light into nanoscale confined and strongly enhanced optical fields, which can be used for localized spectroscopy [17]. In molecular spectroscopy antennas are used to locate molecules and perform field-enhanced spectroscopy on them. The understanding of these antennas is therefore important in order to identify and detect molecular fingerprints using vibrational spectroscopy [18]. However, the near-field measurements in the experiments presented are not used to investigate antennas, but to characterize an infrared transmission line, which can be used to create more complex detector layouts.

## **1.4 Infrared Transmission Lines**

Dielectric waveguides are commonly used in integrated optics. The cross-sectional dimension of the waveguide is approximately equal to the size of the guided wavelength [19]. At RF, metallic transmission lines are used and their size is much smaller than the guided wavelength [20]. Using RF concepts, it has been proposed to fabricate a transmission line composed of nanoinductors and nanocapacitors based on metamaterials at optical frequencies [21]. At IR, coplanar strip lines (CPS), which are two parallel conductors, and microstrips, which is a conductor above a ground plane, have been investigated [22, 23].

Experimental characterization of these transmission lines at infrared frequencies is important to increase the understanding of their properties which can later lead to an optimization of their performance. Detector designs will benefit from improved transmission line designs. The detection element can be completely separated from the antenna element. This type of detector configuration enables the creation of phased-antenna arrays [24], which allows the modification of the array's radiation pattern by adjusting the properties of the transmission line interconnects.

## **1.5 Thesis Statement**

In antenna-coupled bolometers, not all of the measured response is caused by the antenna, but several additional sources contribute to the response. These sources are distributed throughout the detector and stem from electromagnetic coupling of the incident radiation with the bias and readout circuit, joule heating of the bolometer due to the bias current, and thermal heating of the substrate.

In Chapter 2, two experiments are described that demonstrate how the measured detector response is calibrated to remove these distributed response contributions. Two dipoles are oriented perpendicular to each other in the first experiment. This antenna configuration in combination with the readout circuit, which forms a Wheatstone bridge, allows the cancellation of the non-antenna-coupled response contributions. The calibration of these response contributions is demonstrated by the measured polarization response showing agreement with theoretical predictions of the antenna response.

The second experiment demonstrates the calibration of the measured response to remove contributions by the readout and bias circuit. The measured response of dipole arrays are a summation of the desired antenna response and the undesired readout circuit response. An additional device is fabricated that only measures the response of the readout circuit, and the difference of these two measured responses is the antenna response. The measured radiation patterns of only the antenna response of various dipole arrays show excellent agreement with the simulated patterns.

The analysis of the electric field in close proximity to the detector can provide insight in the origins of the non-antenna-coupled response contributions. In the experiment described in Chapter 3, a dipole antenna is used to couple far-field radiation into a CPS. The resulting near-field distribution along the transmission line is measured using a s-SNOM and analyzed to determine the attenuation and propagation constants of the CPS. To accurately characterize the CPS, it is important to know if other mechanisms, besides the dipole antenna, couple radiation into the transmission line. These additional sources are first discovered in simulations of the dipole-coupled CPS and then confirmed by near-field measurements of the fabricated devices.



In the characterization procedure of the CPS, these additional signal sources are calibrated out by incorporating them into the analysis process. The measured transmission line properties agree with the simulated ones.

### **1.6 Prior Publication Disclosure**

Portions of Chapter 2 were originally published in [25] and [26]. Parts of the appendix can be found in [27].

## CHAPTER 2: INFRARED ANTENNA

Two experiments using infrared antennas are described. The first one uses two dipole-coupled bolometers oriented orthogonal to each other. This antenna configuration enables electronic cancellation of the non-antenna-coupled thermal response of the antenna-coupled bolometer. The calibration of these response contributions is successful and the measured polarization dependent response shows excellent agreement with theoretical predictions.

The second experiment does not use an antenna-coupled bolometer, but instead a bolometer that is in the shape of an antenna. It is shown that this distributed bolometric antenna device still possesses directional sensitivity similar to an antenna-coupled bolometer. The lead-lines, which are necessary for signal extraction, also contribute to the measured response. An additional device is designed to measure this contribution and remove it from the measured antenna response. The measured radiation pattern shows excellent agreement with the simulated pattern indicating that this calibration is successful.

The optical setup used to characterize the antenna-coupled detectors is described below. The polarization dependent response is measured by rotating the polarization of the incident radiation using a half-wave plate. The same setup is used to measure the radiation pattern of a detector. To measure an accurate radiation pattern, the device has to be spatially co-aligned with the focus of the incident radiation and the axis of rotation. A procedure for this alignment is outlined in the appendix.

Two approaches are used to simulate these antenna devices. The first one assumes that the antenna is transmitting; it is the source of radiation. From this simulation insight about the impedance at the feed point of the antenna as well as the shape of the radiation pattern can be

gained. The second approach follows the measurement setup more closely. The antenna is excited with a beam of incident radiation and a quantity proportional to the expected response is computed. This simulation approach is used to determine the radiation pattern of the distributed bolometric antenna devices.

## 2.1 Infrared Measurement Setup

The measurement setup used for radiation pattern and polarization dependent response measurements is shown in Figure 1.

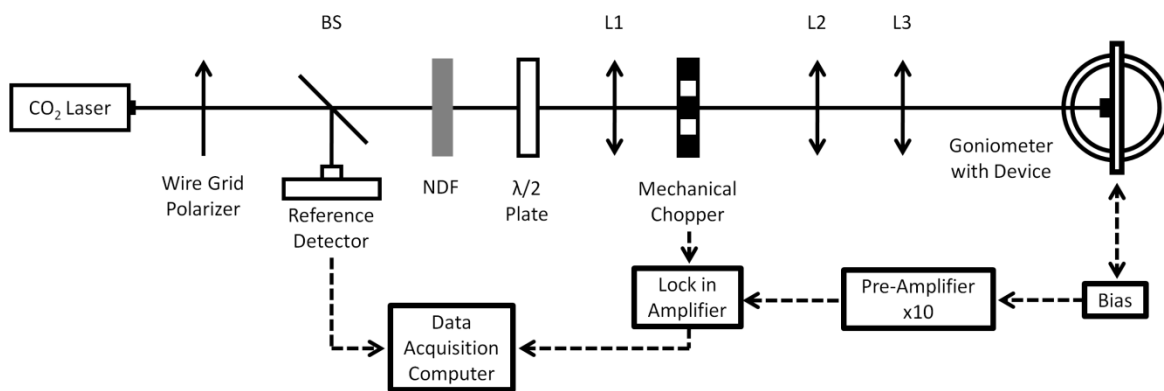


Figure 1: Optical train for antenna characterization.

The source of radiation for the measurements is a CO<sub>2</sub> laser operating at its main emission wavelength of 10.6 μm. A wire grid polarizer is used to reduce the amount of power incident onto the optical train. A beam splitter (BS), directs a portion of the radiation to a reference detector to monitor fluctuations in the laser power. The power in the optical train can further be adjusted using a set of neutral density filters (NDF). These filters are mounted on a filter wheel, which allows for quick exchange of the filter and convenient adjustment of the laser power propagating in the optical train. The polarization angle of the linearly polarized light can be adjusted using a half-wave plate. A telescope system consisting of two lenses, L1 and L2, is

used to expand the beam. A mechanical chopper is located at the focus point of the telescope. The third lens, L3, focuses the collimated beam onto the device at F/8. A knife-edge test showed that the spot size is approximately 230  $\mu\text{m}$  in diameter. The beam spot is large compared to the investigated detectors, which are smaller than  $\sim 20 \mu\text{m}$ . This ensures that the investigated devices are quasi-uniformly illuminated.

The device under test is mounted on a goniometer and positioned at the focus of the laser beam. The goniometer has 5 axes of freedom which allow modification of the x, y, z position of the device as well as rotating and tilting it. The device is externally biased and the measured signal is amplified ten times before it is passed into a lock-in amplifier. The lock-in amplifier is synchronized to the frequency of the mechanical chopper modulating the laser beam. A data acquisition computer controls the movement of the goniometer and records the signal and position of the device, as well as the reference power level of the laser. The recorded response is normalized by the reference power level to remove fluctuations in the recorded device response stemming from fluctuations in the laser power. The normalization is possible for the investigated devices, since an uncooled metal bolometer has a constant TCR [28] and therefore its response depends linearly on a change in temperature caused by the incident irradiance [2].

A calibration was performed to determine the power illuminating the device under test based on the reference power level for each of the possible ND filters used. The irradiance on the device is computed using an approximation, which assumes that the power in the focused spot is evenly distributed within its area with a 230  $\mu\text{m}$  diameter.

In order to accurately measure a radiation pattern, the device, the rotational axis of the goniometer, and the focus of the laser have to be co-aligned. At high operating frequencies as in

the infrared, the antenna dimension and the probe beam size are small and the alignment becomes difficult. Reference [29] points out that this alignment is the limiting factor when measuring radiation pattern. Measurements of radiation patterns at 28.3 THz were attempted before, but only with mixed results [9, 24, 29]. The alignment procedure used to measure the radiation patterns of the distributed bolometric antennas in section 2.4 is outlined in the appendix.

## **2.2 HFSS Simulation**

Ansoft HFSS is used to simulate the infrared antennas. This electro-magnetic simulation tool is based on the finite element method (FEM). The software subdivides a predefined volume, which includes the antenna and its surrounding environment such as a substrate and vacuum, into smaller subsections which are referred to as finite elements. The collection of these elements, in HFSS they are tetrahedra, forms a mesh. HFSS solves for the electric field on the nodes of this mesh while making sure that Maxwell's equations are satisfied. The magnetic field is calculated from the electric field. All other quantities are derived from these two fields [30].

HFSS is useful for the simulation of infrared antennas, since it allows the incorporation of complex dielectric constants describing the materials. The materials used for the orthogonal dipoles are high resistivity silicon as the substrate, and electron-beam evaporated gold and nickel. The distributed bolometric antenna uses electron-beam evaporated gold, the spin-on dielectric benzocyclobutene (BCB) [31], which exhibits low loss at 10.6  $\mu\text{m}$ . The aluminum ground plane in the simulation of the distributed bolometric antenna is approximated by a perfect electric conductor (PEC), since the thickness used is multiple skin depths [32]. A J. A. Woollam

IR-VASE ellipsometer [33] is used to measure the relative permittivity of the appropriate thin film thicknesses at 28.3 THz. The values used in the HFSS simulations are listed in Table 2.

Table 2: Dielectric constants.

Material	$\epsilon_r'$	$\epsilon_r''$
silicon (high resistivity)	11.7	$1.52 \cdot 10^{-5}$
BCB	2.36	0.071
gold	-4787	1630
nickel	-1424.8	740.45

Two different approaches are used to determine information about antennas. The first one is to simulate the antenna as a transmitting element, referred to as an active antenna. The transmitting and receiving radiation pattern of an antenna is identical due to reciprocity [7]. This property is true if the materials used for the antenna and the detector at its feed point are linear. A bolometer is essentially only a resistor and therefore meets this requirement. Non-linear devices such as diodes would make the antenna nonreciprocal. The second approach is to simulate the antenna as a receiving element. This simulation follows much more closely the measurement conditions where the antenna is excited by an incident beam.

### 2.2.1 Active antenna

To simulate a radiating antenna, the bolometer of the antenna-coupled bolometer is replaced by a "lumped port," which is used to excite the antenna. It is analogous to a current-sheet source and forces an oscillating current onto the feed point of the antenna. Figure 2 shows the general layout of an active antenna in HFSS. The simulation volume encloses a substrate, a

region of vacuum, and an antenna, which is located at the interface between the substrate and vacuum. The antenna consists of two dipole arms that are connected by the lumped port.

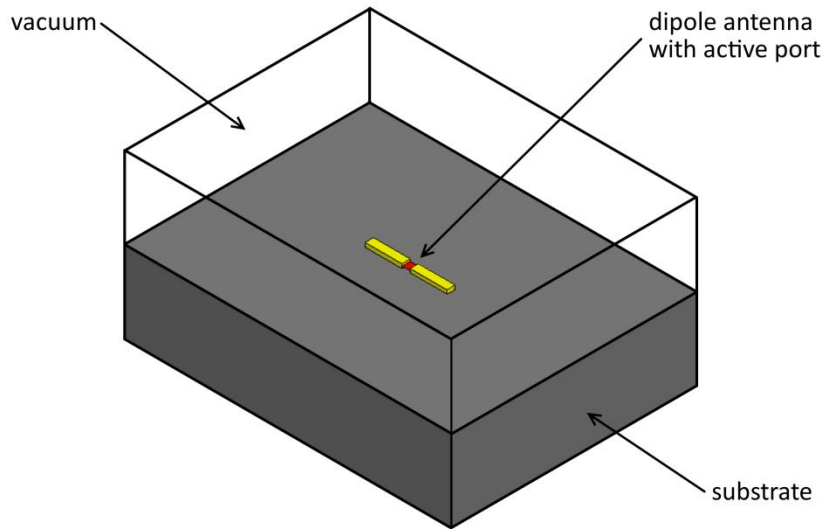


Figure 2: HFSS layout of an active antenna.

A "radiation boundary" is assigned to the outside surfaces of the simulation volume. This boundary must be separated by at least a quarter wavelength from any object from which the radiation emanates, i.e. the arms of the dipole antenna. The radiation boundary is used to simulate an open problem that allows waves to radiate infinitely far into space. This is accomplished by HFSS absorbing the waves at the two dimensional surface of the radiation boundary. The boundary conditions used when assigning the radiation boundary assume that the incident wave is propagating in free space. This may not be a good approximation of the antenna design, especially if the antenna is located on a large substrate. This type of boundary condition is usually used in an initial simulation to determine characteristics of an antenna design.

Using this type of simulation setup, HFSS determines the electric and magnetic field inside the simulation volume. The radiation pattern as well as the input impedance at the feed point of the antenna are computed by default.

### 2.2.2 Receiving antenna

The simulation of a receiving antenna emulates the measurement setup much closer than the simulation of the active antenna. Figure 3 shows the general layout of a receiving antenna. It is very similar to the one of an active antenna. Again, the antenna is located at the interface between a substrate and vacuum. In the illustrated case, the dipole antenna is terminated by a bolometer.

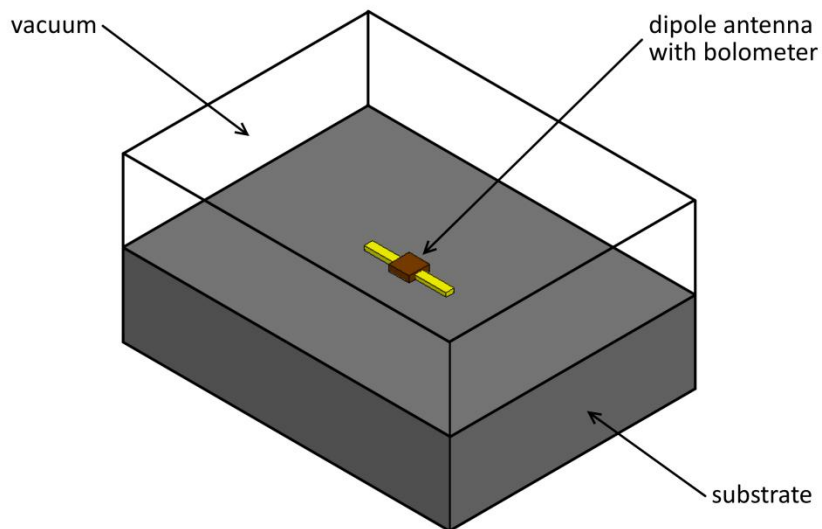


Figure 3: HFSS layout of a receiving antenna.

The surfaces of the simulation volume are not assigned the previously described radiation boundary, but a more general termination, the "perfectly matched layers" (PML). This boundary will, like the radiation boundary, absorb any radiation traveling towards it. To create the PML, HFSS creates a volume and places it in direct contact with the surface to which the boundary is



assigned. The material properties of the PML are computed such that a wave traveling inside the solution volume is transmitted into the PML without any reflections. Once the wave propagates inside the PML, it is attenuated to a negligible magnitude. In contrast to the radiation boundary, the PML can be matched to any material, not only vacuum. The gained accuracy in the simulation comes at the price of an increase in required computation resource and computation time.

The antenna is illuminated by an incident field, which can be plane wave or a Gaussian beam. The direction, polarization, and field strength of the incident beam can be specified. This type of simulation solves for the electric and magnetic field everywhere within the simulation volume. Derived field quantities such as the current density can also be computed.

The bolometric response is proportional to the power dissipated in the bolometer volume due to ohmic loss [5]. Computations using the simulated field quantities can be performed in two ways. The electric field and current density inside the bolometer volume can be exported and the ohmic loss is computed manually by integrating the dot product of the electric field and complex conjugate of the current density over the bolometer volume

$$P_{\text{ohmic}} = \frac{1}{2} \text{Re} \left[ \int_{\text{vol}} \mathbf{E} \cdot \mathbf{J}^* dv \right]. \quad (4)$$

Alternatively, the "fields calculator" feature in HFSS can be used. By selecting to integrate the "volume loss density" over the volume of the bolometer Eq. (4) is evaluated. The radiation pattern of the antenna are simulated by varying the angle of incidence of the illuminating plane wave or Gaussian beam. For each angle, the power dissipated in the bolometer volume is computed. Following this method the simulation of radiation patterns can be time consuming, since the simulation is re-evaluated multiple times, depending on the angular

resolution of the radiation pattern. To decrease computation time, the incident wave can be defined in spherical coordinates. For this type of excitation setup, it is possible to specify multiple incident waves on a user-defined angular grid. All of the specified incident waves are simulated at once. When calculating the ohmic loss in the bolometric volume in the fields calculator, the angle of the incident wave can be selected from the user-defined angular grid.

### **2.3 Orthogonal Dipole Antennas**

The polarization response of an infrared antenna-coupled thermal sensor is strongly affected by the thermal and electrical characteristics of the surrounding structures, such as the substrate, lead lines, and bondpads [34-38]. For linearly polarized antennas such as dipoles, bowties, and log periodics, the co-polarized response is commonly identified with the antenna-coupled signal. The cross-polarized response originates from the electromagnetic coupling of signal extraction structures such as bondpads and lead lines, as well as from Joule heating of the bolometer due to the bias current, or from heating of the structural substrate by laser irradiation. However, these additional effects also contribute to the measured co-polarized signal, and a method to accurately remove these response contributions is desirable. This is especially necessary when quantitatively assessing the sensor-response mechanisms, when several response modes operating simultaneously [39].

In this experiment the operation of a pair of infrared dipole antennas is demonstrated. The dipoles are aligned orthogonal to each other and their electrical outputs are wired to form a Wheatstone bridge. The combination of the geometrical arrangement of the antennas and their internal and external electrical connections allows the calibration of the co-polarized response

contribution and its isolation from the measured signal. Additionally, it is shown that the recorded signal of this detector is proportional to the  $S_1$  Stokes parameter [40].

### 2.3.1 Antenna design

The lead lines in this antenna design are omitted and the dipole antenna is directly connected to the bondpads. The length of the dipole is chosen to maximize the response at a wavelength of  $10.6 \mu\text{m}$  [41]. The antenna is simulated as an active antenna and the input impedance is determined as a function of the dipole length. The result is shown in Figure 4. Parts of the bondpads are included in the simulation.

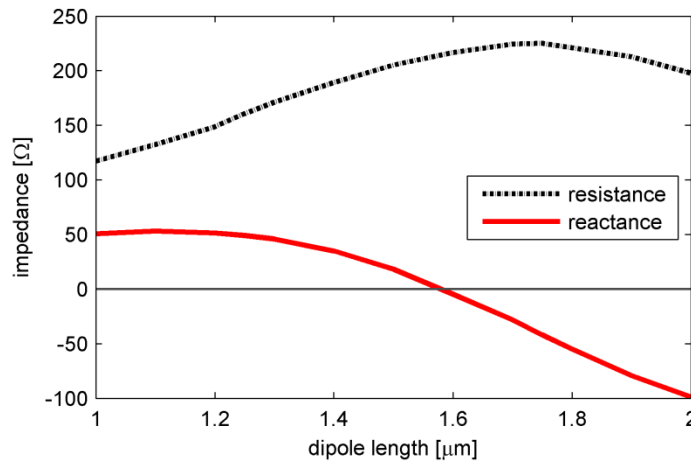


Figure 4: Complex input impedance of dipole antenna in direct contact with bondpads as a function of the dipole length.

The dipole is predicted to be resonant at a length of  $1.55 \mu\text{m}$ , where the imaginary part of the dipole impedance vanishes [7]. In this definition of resonance, all energy presented to the antenna is transmitted, since the impedance at the feedpoint of the antenna is completely real. If the input impedance includes an imaginary part, some of the available energy is not transmitted, but stored in the reactive near field.

The layout of the dipole antenna differs significantly from its common layout, since its ends are directly terminated in the bondpads. The bondpads are fabricated during the same fabrication step as the antenna and are therefore composed of the same material as the dipole. This has the result that the bondpads become part of the radiating antenna as shown in Figure 5.

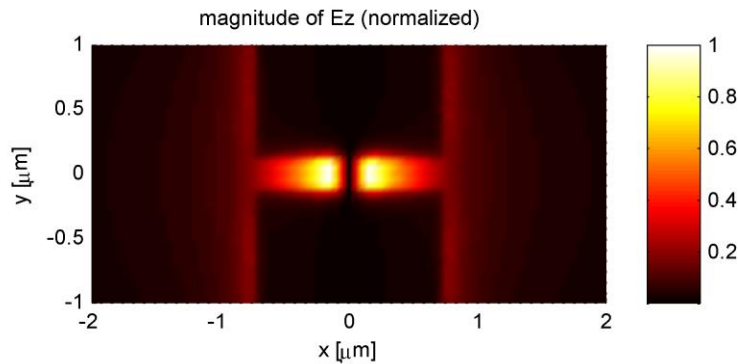


Figure 5: Simulated electric field on dipole which is in direct contact with the bondpads.

The magnitude of the electric field component perpendicular to the plane containing the antenna and bondpads is shown in Figure 5. The darkest area in the center of the figure ( $-0.775 < x < 0.775 \mu\text{m}$ ) corresponds to zero field distribution on the silicon substrate, while areas with a visible field distribution correspond to either the dipole or the bondpads. The dipole arms, especially closest to the excitation source at the center of the antenna, show the largest field distribution. The field distribution does not vanish at the ends of the antenna arms, and a small, but still significant, field component is present and extends onto the bondpads. This confirms that the bondpads are part of the radiating structure. The resonant dipole length between the bondpads of this antenna configuration is therefore shorter than expected for an isolated dipole located at a silicon-air interface as determined by an effective medium approximation:  $\epsilon_{\text{eff}} = \frac{\epsilon_{\text{sub}} + 1}{2}$ , where  $\epsilon_{\text{sub}}$  is the permittivity of the substrate and  $\epsilon_{\text{eff}}$  the effective permittivity at the interface [42]. Using the permittivity value for silicon value from Table 2, the free space

wavelength of 10.6  $\mu\text{m}$  scales to an effective wavelength of 4.2  $\mu\text{m}$  at the silicon-air interface. The resulting half-wave dipole length obtained by this method is 2.1  $\mu\text{m}$ .

### 2.3.2 Device fabrication and readout circuit

A high resistivity (3–6  $\text{k}\Omega\cdot\text{cm}$ ) silicon wafer is coated with 400 nm of ZEP 520A-7 electron-beam resist. The dipoles and bondpads are exposed using the Leica ebpg 5000+ at a dose of 120  $\mu\text{C}/\text{cm}^2$ , a beam current of 25 nA, and a spot size of 25 nm. The wafer is then developed in ZEP-RD for 90 seconds. The dipole antenna and bondpads are 75-nm-thick electron-beam evaporated gold with a 5 nm titanium adhesion layer. The excess resist and metal are lifted off in a methylene chloride bath. The bolometers are fabricated of a different metal and require a second lithography exposure. The wafer is now coated with a electron-beam resist bi-layer consisting of a 350-nm-thick EL9 MMA-copolymer layer and a 150-nm-thick 950 PMMA A4 layer. A different electron-beam resist has to be used for this second fabrication step, since the resist used in the previous step, ZEP 520A-7, exhibits poor adhesion to the gold bondpads and does not protect them during the subsequent processing steps. The bolometers are exposed with a dose of 600  $\mu\text{C}/\text{cm}^2$ , a beam current of 25 nA, and a spot size of 25 nm. The electron-beam resist is developed in a 3:1 mixture of isopropanol alcohol (IPA) and methyl-isobutyl-ketone (MIBK) for 120 seconds followed by a 60 second descum etch in an oxygen plasma. The descum etch removes any remains of the developed resist, resulting in a clean surface onto which the metal is deposited, promoting adhesion and electrical contact between the bolometer and the terminals of the dipole antenna. 80 nm of electron-beam evaporated nickel is used to form the bolometer. The excess resist and metal is removed in a methylene chloride bath. One of the three fabricated device designs is shown in a scanning electron micrograph in Figure 6.

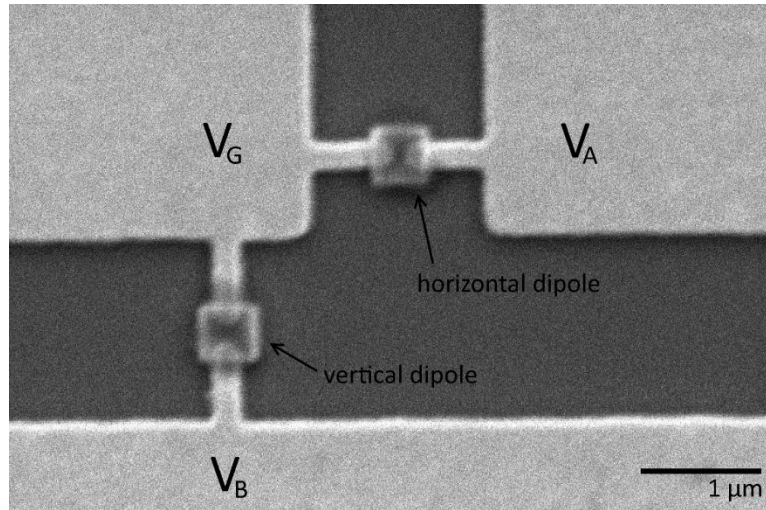


Figure 6: Scanning electron micrograph of orthogonal dipole pair.

The lightly colored large areas in Figure 6 are the gold bondpads. The dipoles are of the same color and connect the bondpads. They are  $1.55 \mu\text{m}$  long and  $240 \text{ nm}$  wide. The nickel bolometers are located at the center of the dipoles and are squares of  $520 \text{ nm}$  width. The dark gray areas in the scanning electron micrograph represent the silicon substrate. The two dipole antennas share a common bondpad, which is labeled  $V_G$ . The horizontally oriented antenna, referred to as dipole A, is connected to the bondpad  $V_A$  and the vertical antenna, dipole B, is connected to bondpad  $V_B$ .

The distance between the centers of the two orthogonal dipoles is varied ( $1.33$ ,  $1.78$ , and  $2.05 \mu\text{m}$  in devices 1, 2, and 3, respectively), to examine any influence of this distance on the overall behavior of the detector. A smaller separation of the dipoles might be expected to exhibit a higher electromagnetic crosstalk, at the cost of a more compact measurement aperture. The DC resistance of each bolometer is different due to lithographic differences. The resistances of the devices that were investigated vary from  $24.4$  to  $40.3 \Omega$ .

The configuration of the readout circuit is modified from the one described in section 2.1. Figure 7 shows that the interconnection between the two antenna-coupled sensors, along with the external biasing electronics, configures a Wheatstone bridge. The response of each sensor consists of several contributions: the dipole-antenna-coupled response, a polarization insensitive substrate-heating thermal response, residual electromagnetic crosstalk between the antennas themselves and between the antennas and the bondpads. The response contribution of interest is the dipole-coupled response. The Wheatstone bridge arrangement is able to calibrate the thermal response contribution to each element. Any electromagnetic crosstalk will be the same for both antennas due to the geometrical symmetry of the layout.

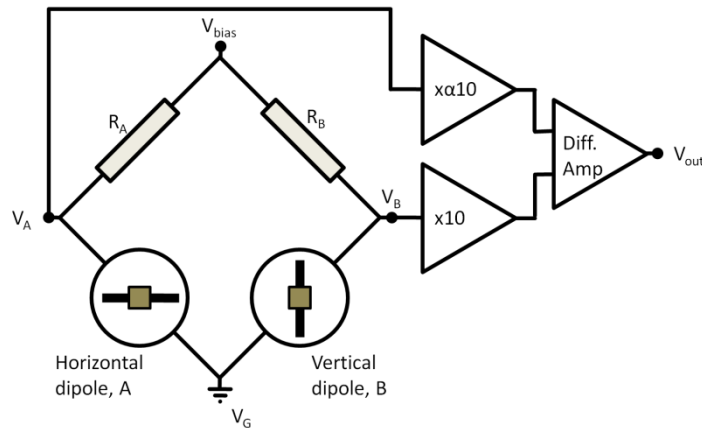


Figure 7: Schematic of on-chip and off-chip wiring.

Both bolometers (A and B) are biased using the same voltage,  $V_{bias} = 150$  mV, and biasing resistors of equal value are used,  $R_A = R_B$ . The DC resistances of the individual bolometers are slightly different, which unbalances the Wheatstone bridge, even when the antennas are not illuminated. The voltage signals  $V_A$  and  $V_B$  obtained from the bridge are fed to two independent amplifiers. The gain of one amplifier is variable ( $\alpha$ ), which allows the output of the bridge to be externally balanced, yielding a differential voltage,  $V_{out} = 10 \times (\alpha V_A - V_B)$ . A

dual-channel lock-in amplifier operating in differential mode is used to measure  $V_{\text{out}}$ . This configuration allows cancellation of the cross-polarized response of the antenna. The remaining signal will be the dipole-antenna-coupled portion of the response, which should be proportional to the projection of the electric field along the dipole direction.

The polarization of the laser is linear with an azimuth angle  $\theta$ , which can be rotated using a half-wave plate. An incident beam polarized in the horizontal direction is defined as  $\theta = 0^\circ$ . The differential voltage signal obtained from the detectors,  $V_{\text{out}}$ , is normalized to the reference laser power,  $P$ , to produce the responsivity  $\mathfrak{R}_{\text{out}} = V_{\text{out}}/P$ , having dimensions of [V/W]. To balance the Wheatstone bridge, the polarization of the incident light is set to  $45^\circ$ . The gain  $\alpha$  of the variable amplifier is then adjusted to cancel the differential signal.

### 2.3.3 Results

The investigated devices are the three pairs of orthogonal dipoles, for which the distance between the centers of the dipoles is varied as noted earlier. The responsivity  $\mathfrak{R}_{\text{out}}$  vs.  $\theta$  is expected to follow the polarization angle,  $\theta$ , as a harmonic function, and is plotted in Figure 8.

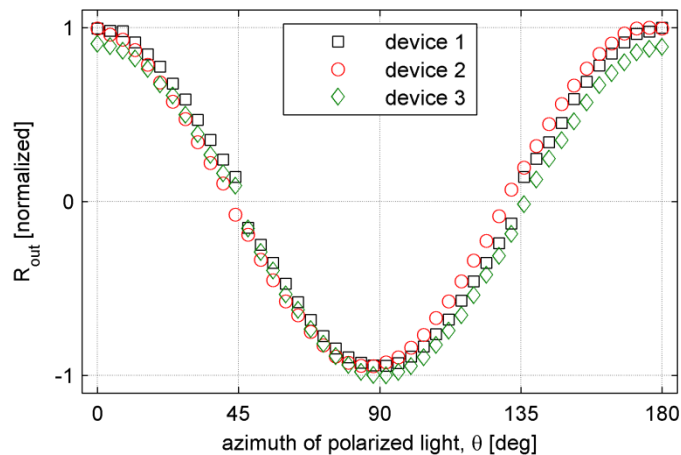


Figure 8: Measured polarization response of orthogonal dipole pairs.



The measured responsivity  $\mathfrak{R}_{\text{out}}$  is normalized to the maximum magnitude of each device. The distance between the centers of the dipoles does not seem to produce a noticeable effect on the measured response of the dipole pairs. This is possibly due to the small size of the variation in the distance between the dipoles, which is limited to the sub-wavelength range. The variation of  $\mathfrak{R}_{\text{out}}$  with respect to the azimuth angle can be modeled as

$$\mathfrak{R}_{\text{out}} = \mathfrak{R}_0 \cos[2(\theta - \theta_0)] - \mathfrak{R}_{\text{offset}}, \quad (5)$$

where  $\mathfrak{R}_0$  accounts for the amplitude of  $\mathfrak{R}_{\text{out}}$ ,  $\theta_0$  represents a small shift due to angular misalignments and angular positioning errors in the polarization elements, and  $\mathfrak{R}_{\text{offset}}$  represents a constant residual level. This  $\mathfrak{R}_{\text{offset}}$  should be as small as possible and can be minimized by properly balancing the outputs of the Wheatstone bridge. A non-linear fitting algorithm is used to fit Eq. (5) to the measured data while minimizing the sum square of errors (SSE) [43]. The values of the parameters that best fit the experimental data are listed in Table 3.

Table 3: Parameters obtained by fitting Eq (5) to measured data.

Device	$\mathfrak{R}_0$	$\mathfrak{R}_{\text{offset}}$	$\theta_0$ (deg)
1	0.979	-0.028	-0.068
2	0.974	-0.029	-3.677
3	0.951	0.049	0.537

Alternatively, the values for  $\mathfrak{R}_0$  and  $\mathfrak{R}_{\text{offset}}$  can be obtained from the measurements of the individual elements forming the orthogonal dipole pair.  $\mathfrak{R}_{0,\text{exp}}$  is computed as

$$\mathfrak{R}_{0,\text{exp}} = \frac{1}{2} [(\mathfrak{R}_{\text{hor,max}} - \mathfrak{R}_{\text{ver,min}}) + (\mathfrak{R}_{\text{ver,max}} - \mathfrak{R}_{\text{hor,min}})]. \quad (6)$$

$\mathfrak{R}_{\text{hor,max}}$  and  $\mathfrak{R}_{\text{hor,min}}$  are the maximum and minimum responses of the horizontal dipole (dipole A) corresponding to the orientation of the incident light at  $0^\circ$  and  $90^\circ$ .  $\mathfrak{R}_{\text{ver,max}}$  and  $\mathfrak{R}_{\text{ver,min}}$  are the responses of the vertical dipole (dipole B) when the incident polarization is oriented at  $90^\circ$  and  $0^\circ$  respectively. The same values are used to compute the offset in the response

$$\mathfrak{R}_{\text{offset,exp}} = \frac{1}{2} [(\mathfrak{R}_{\text{hor,max}} - \mathfrak{R}_{\text{ver,min}}) - (\mathfrak{R}_{\text{ver,max}} - \mathfrak{R}_{\text{hor,min}})]. \quad (7)$$

Table 4 lists the maximum and minimum values of the measured response obtained from the individual horizontally and vertically oriented dipoles. These values are normalized by the same factor as the measured response shown in Figure 8. The minimum value is assumed to be caused by the polarization independent thermal response of the device. These values are not equal for both elements in a given dipole pair due to slight variations in the impedance of the elements resulting from fabrication tolerances.

Table 4: Values of  $\mathfrak{R}_0$  and  $\mathfrak{R}_{\text{offset}}$  calculated from measured responses of individual dipoles.

Device	$\mathfrak{R}_{\text{hor,max}}$	$\mathfrak{R}_{\text{hor,min}}$	$\mathfrak{R}_{\text{ver,max}}$	$\mathfrak{R}_{\text{ver,min}}$	$\mathfrak{R}_{0,\text{exp}}$	$\mathfrak{R}_{\text{offset,exp}}$
1	3.79	2.54	3.52	2.91	0.933	-0.046
2	2.06	1.25	2.21	1.12	0.945	-0.010
3	2.00	0.77	1.64	1.05	0.912	0.0390

The values for  $\mathfrak{R}_0$  and  $\mathfrak{R}_{\text{offset}}$  are calculated using Eq. (6) and (7). The results are also shown in Table 4.

### 2.3.4 Stokes parameter measurement

Using the signals obtained from the devices, it is possible to obtain an experimental value of the normalized  $S_1$  Stokes parameter. Following the definition of the  $S_1$  Stokes parameter in terms of the electric field amplitudes,  $S_1 = |E_x|^2 - |E_y|^2$ , the output obtained from the lock-in amplifier working in differential mode,  $V_{\text{out}}$ , is directly proportional to  $S_1$ . Also, since  $\mathfrak{R}_{\text{out}}$  contains a normalization to the total power of the beam, and considering the definition of the Stokes parameter  $S_0 = |E_x|^2 + |E_y|^2$ ,  $\mathfrak{R}_{\text{out}}$  is proportional to the normalized  $s_1 = S_1/S_0$  parameter. The value of the amplitude  $\mathfrak{R}_0$  in Eq. (5) can be regarded as the proportionality constant between  $\mathfrak{R}_{\text{out}}$  and  $s_1$ .  $\mathfrak{R}_{\text{offset}}$  can be reduced to zero by properly balancing the Wheatstone bridge.

Figure 9 shows the value of  $s_1$  evaluated from the measurements compared to the expected value calculated analytically from the polarization state illuminating the devices.

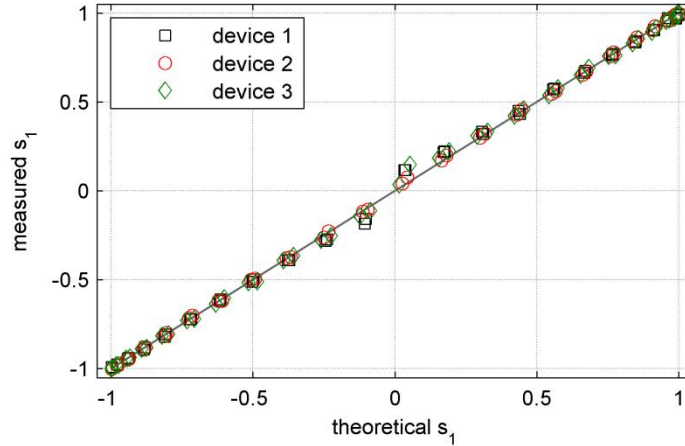


Figure 9: Normalized Stokes parameter  $S_1$  obtained from measurements.

The measured values are corrected for  $\mathfrak{R}_{\text{offset}}$  and  $\theta_0$  since a careful alignment can reduce these errors. The poorest experimental evaluation of  $s_1$  appears around  $s_1 = 0$ , which

correspond to values of the signal closest to zero. This is caused by the noise level of the devices and external electronics, as well as the uncertainties associated with the balancing of the Wheatstone bridge.

In order to measure the remaining Stokes parameters,  $s_2$  and  $s_3$  [40], the device has to be modified. The inclusion of an additional pair of orthogonal dipoles oriented at  $45^\circ$  with respect to the horizontal direction can be used to determine  $s_2$  [44]. The integration of a quarter-wave plate [45] properly oriented with respect to the dipoles can be used to determine the fourth Stokes parameter,  $s_3$ .

## **2.4 Lead-Line Response Calibration**

The antenna element of the orthogonal dipole pairs is in direct contact with bondpads. It was shown that the bondpads become part of the radiating structure and the behavior of the antenna is altered. It is of interest to minimize the effects of the bondpads on the antenna. This is achieved by using lead lines, which are narrow metal strips that connect the antenna to the bondpads and facilitate biasing of the antenna and reading out of the measured response. For the following investigated devices, the antenna layout is simplified from the orthogonal dipoles. Instead of using an antenna-coupled bolometer, the bolometer is shaped to form an antenna. This simplification of the antenna layout enables a straightforward and rapid fabrication process and has the consequence that the response is not measured by a discrete sensor element at the feed point of the antenna, but incident power that is dissipated in any sections of the antenna will contribute to the measured response. In the previous antenna-coupled bolometer design, each section of the antenna also contributed to the measured response. These contributions were not

equal, since the material of the antenna was chosen to respond less to a change in temperature than the material of the bolometer as indicated by the TCR values listed in Table 1. A distributed bolometer antenna can be designed to exhibit the spectral, polarization, and directional properties that make antenna-coupled bolometers desirable.

The investigated receiving antennas are one-, two-, three-, and four-dipole arrays that are separated from a ground plane by a dielectric standoff layer. This substrate configuration is chosen due to previous investigations where antenna-coupled bolometers on substrates with a ground plane showed a threefold increase in the measured response when compared to identical detectors on the substrate that was lacking the ground plane [35]. Another method used to increase the measured response is to place the antenna at the flat interface of a hemispherical lens. The measured response when illuminating the device through the substrate is much greater than when the device is illuminated from the air side. However, the radiation pattern for this substrate configuration shows dips around broadside illumination [46]. The theoretically predicted radiation pattern of a dipole located above a ground plane does not display these dips and it has a maximum at broadside [7].

The biasing and readout circuits also respond to the incident radiation. This contribution is measured by a reference device and subtracted from the distributed antenna response. Excellent agreement between the measured and simulated radiation pattern of only the antenna elements is demonstrated, indicating the success of the presented method for lead-line response calibration and that the presented simulation technique can be used to design and optimize a distributed-antenna design.

### 2.4.1 Antenna design

The antenna arrays, which are designed to operate at the main CO<sub>2</sub> laser line of 28.3 THz, are simulated as receiving antennas in HFSS. Details of this simulation are explained in chapter 2.2.2. The device layout has several dimensions that can be varied to optimize the distributed antenna response. To ensure a successful fabrication process, most of these dimensions are fixed and only the dipole length and element separation are optimized. The gold dipoles are 200 nm wide and 75 nm thick and the dielectric standoff layer, which is BCB, is 1.6 μm thick. The standoff layer separates the antenna elements from a ground plane. In the simulation, the measured at-frequency dielectric constants from Table 2 are assigned to the antenna and the standoff layer.

The optimum length of the dipole is determined by simulating an isolated single dipole, which is illuminated by a plane wave from normal incidence with the polarization parallel to the axis of the antenna. The length of the dipole is varied and the response is computed by determining the power dissipated in the entire dipole as discussed in Chapter 2.2.2. As indicated in Figure 10 (a), the predicted bolometer response is largest at a dipole length of 3.2 μm.

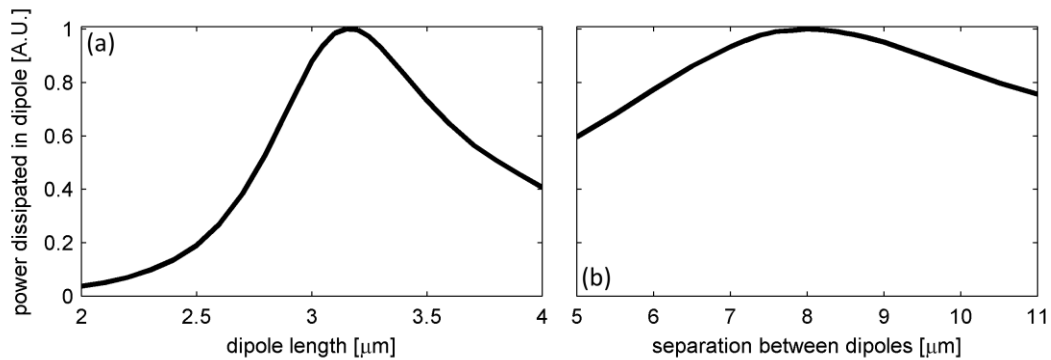


Figure 10: Predicted response of (a) dipole as a function of its length and (b) two-dipole array with varying element separation.

The optimum spacing between array elements is determined in a similar fashion. Two dipoles are illuminated from broadside and the power dissipated in the gold of both antennas is computed as a function of their separation. Figure 10 (b) indicates that the largest response of two 3.2  $\mu\text{m}$  long dipoles is expected for a separation of 8  $\mu\text{m}$ . The same separation is used for the three- and four-element arrays. Simulations completed after finalizing the device fabrication show that a slight adjustment in the element spacing may be preferred. The simulated response of the three- and four-dipole array is maximized when the elements are separated by 8.5  $\mu\text{m}$  and 8.75  $\mu\text{m}$  respectively.

#### 2.4.2 Antenna response measurements without lead-line contributions

The simulation used to optimize the distributed bolometric antennas omits the lead lines for the biasing and readout circuit due to a primary interest in only the antenna response. A secondary advantage of the omission of the lead lines in the simulation is that the simulation volume in which HFSS computes the electric field is small, which reduces required computational resources and time. The lead lines are necessary to measure the response and have to be included in the fabricated devices. This part of the device is created during the same fabrication step as the antennas and it is also composed of gold. The lead lines are oriented perpendicular to the dipole antenna and therefore also perpendicular to the polarization of the incident radiation. The incident beam is focused to a spot with a diameter of 230  $\mu\text{m}$ . While measuring the radiation pattern, the goniometer is rotated to  $\pm 70^\circ$ . At these large angles, the beam illuminating the antenna is elliptical with an approximate width of 670  $\mu\text{m}$  along the direction of the lead lines. The fabricated lead lines are long enough to ensure that the bond pads are not significantly illuminated during the radiation pattern measurement.

Similar to the distributed dipole antennas, these gold lead lines respond bolometrically to the incident radiation. The orientation of the lead lines is chosen to minimize their interaction with the incident polarized laser beam. Although the lead lines should not respond to the incident radiation, each incremental section of the lead lines will contribute a finite amount to the measured response. Due to the extensive length of the lead lines, the sum of these contributions is comparable in magnitude to the response of the distributed bolometric antenna. The presence of this response contribution removes predictive power of the simulated response, which does not include the lead lines, when comparing it to the measured response of the investigated device.

To calibrate this response contribution, a second device is fabricated on the same substrate as the dipole arrays. This additional device is similar to the array device, but the dipoles are removed. The measured response from this device is equivalent to the response contribution of the lead lines to the antenna response in the dipole-array device. To ensure the same irradiance illuminating both devices, they are placed  $4\ \mu\text{m}$  apart from each other. Simulations indicate that the addition of the second device at the specified distance does not alter the radiation pattern of the antenna array.

In the simulation, the shape of the radiation pattern is created by mutual coupling of the isolated elements in the array. The incident radiation causes a current to flow in each array element, which reradiates parts of the incident wave toward the other array elements. The amount of radiation received by each array element is the vector sum of the incident wave and the reradiated waves from the surrounding array elements [7]. The measured response is the summation of the contributions by the antenna and the lead-line only if the presence of the lead



lines does not alter the coupling mechanism between the array elements. This independence has to be shown.

The lead lines connect the dipoles with a narrow strip at the center of the antenna. A microstrip waveguide configuration is formed, since the lead lines are located above a ground plane. This microstrip serves only as a signal extraction interconnect rather than as a waveguide, since the contact with the dipole is not designed to couple a propagating waveguide mode. Only if the device geometry does not support a propagating mode in this waveguide, no additional coupling between the array elements will occur. This indicates that the simulated response of the isolated antenna-array elements is equivalent to the simulated antenna-array elements in the presence of the lead lines.

A two-dipole array including a 30  $\mu\text{m}$  long section of the lead lines is simulated to show that the response of the antenna elements is not affected by the presence of the lead lines. The array is illuminated by a plane wave, polarized along the y-axis, and propagating along the z-axis. The layout of the array including the lead lines is shown in Figure 11 (a). The yz-plane located at the center of the two dipoles is highlighted and the real part of the electric field in this plane is shown in Figure 11 (b). The field lines in Figure 11 (b) are not oriented between the ground plane and the conducting strip as expected for a microstrip [20], but instead, they are parallel to the incident radiation. This validates that the design of this microstrip configuration does not support a propagating waveguide mode and can only serve for signal extraction. Therefore, the presence of the lead lines has no impact on the antenna array response. Further, the response of the array elements can be determined by subtracting the measured lead-line contribution from the measured array response.

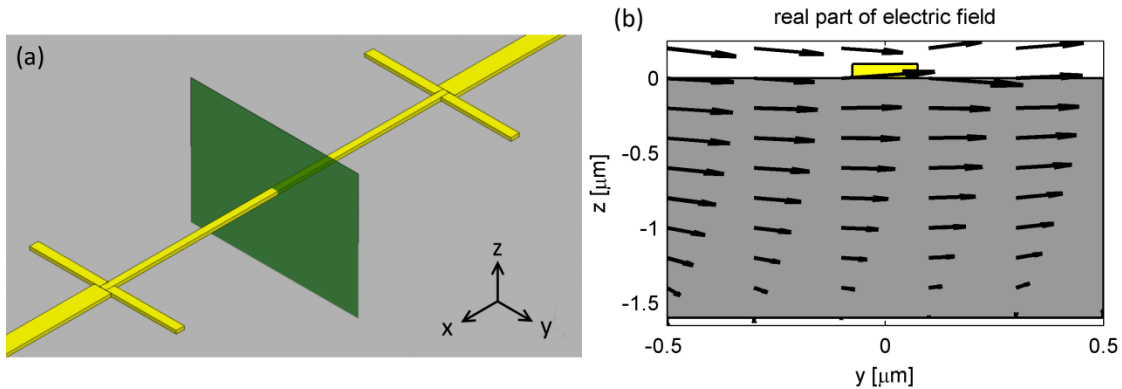


Figure 11: HFSS layout of a two-dipole array including lead lines (a). The highlighted yz-plane at the center of the two dipoles is where the simulated electric field is shown (b).

### 2.4.3 Device fabrication

The distributed bolometric antenna arrays are fabricated by first creating the substrate. A low resistivity prime grade silicon wafer is coated with 80 nm of thermally evaporated aluminum to create the ground plane. A 1.6 μm thick layer of BCB is spun onto the wafer, which forms the dielectric standoff layer.

The pattern of the antenna arrays is exposed using electron-beam lithography. The layout of the bond pads and lead lines of each fabricated device is identical and it is shown in Figure 12. The bond pads are the large tapered structures located on either end of the narrow lead lines. The outside edge of the bond pads is 150 μm long and the edge where the bond pad is connected to the lead lines is 3 μm long. The bond pads are 250 μm wide. The lead lines are also tapered. Their edge close to the antenna array is 0.3 μm long. The distance between the bond pads and the antenna array is 250 μm. The lead line and bond pads of the antenna array and the device used to measure the lead-line-response contribution are symmetric about the axis along the lead lines. They are separated by 4 μm. The antenna array is too small in this figure and it is therefore not visible.

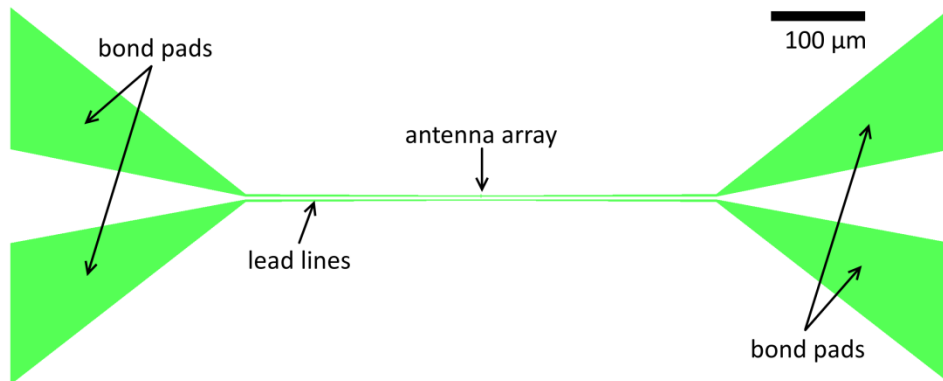


Figure 12: Layout of bond pad and lead line configuration.

The substrate is coated with 400 nm of an electron-beam sensitive resist, which in this case is ZEP 520A-7. The antenna pattern is exposed using the Leica ebpg 5000+ at a dose of  $120 \mu\text{C}/\text{cm}^2$ . The beam current is 25 nA and the spot size is 25 nm. The areas of the resist that were exposed to the electron beam are removed by submerging the wafer in a bath of ZEP-RD for 90 seconds followed by a 60 seconds oxygen plasma descum etch. The devices are metalized with a 5-nm-thick titanium adhesion layer and 75 nm of electron-beam-evaporated gold. The remaining resist and excess metal are lifted off in a methylene chloride bath. A magnified view of the fabricated devices is shown in the scanning electron micrographs in Figure 13.

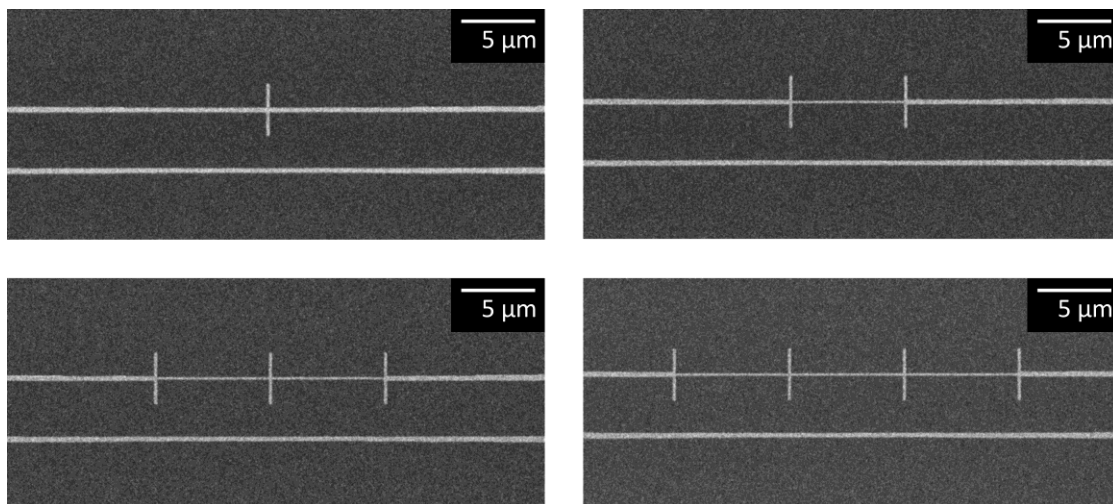


Figure 13: Scanning electron micrographs of one-, two-, three-, and four-dipole array.

The large dark gray areas in Figure 13 indicate the BCB substrate and the lighter, smaller areas are the gold devices. The straight line adjacent to the antenna arrays is the device that is used to measure the response contribution of the lead lines. Analyzing the fabricated devices in the scanning electron micrographs revealed that their dimensions vary from the designed devices due to fabrication tolerances. The dimensions of the fabricated devices that are different from the designed dimensions are listed in Table 5.

Table 5: Dimensions of fabricated dipole arrays.

Number of dipoles in array	Dipole length ( $\mu\text{m}$ )	Dipole separation ( $\mu\text{m}$ )
1	3.61	-
2	3.49	7.8
3	3.47	7.8
4	3.48	7.8

The listed dimensions of the fabricated devices are incorporated in the simulations in following two sections.

#### 2.4.4 Measurements and results

To demonstrate that the removal of the lead-line response contribution from the measured response of a distributed bolometric antenna array is possible, the H-plane radiation pattern is measured and compared to the simulated one. The H-plane is defined as the plane containing the magnetic-field vector and the direction of maximum radiation [7]. This is illustrated for an individual dipole antenna in Figure 14. To complete the radiation pattern measurement, the

goniometer scans the H-plane from  $-70^\circ$  to  $+70^\circ$ , stopping every  $1^\circ$  to record five data points, which are averaged to result in a single measurement.

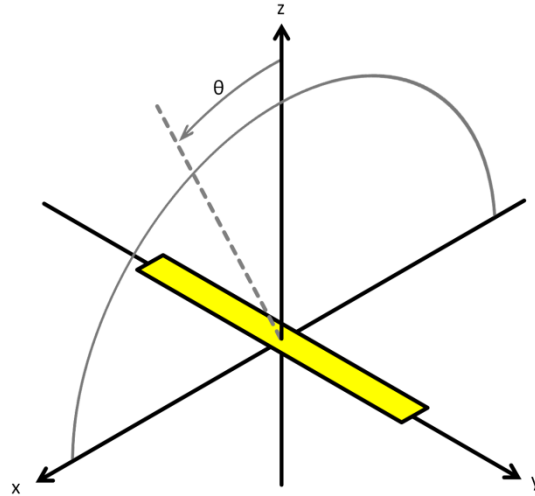


Figure 14: Geometry of a dipole illustrating the H-plane.

The measured response  $V_{\text{out}}$  [V] is normalized to the irradiance of the incident laser beam  $E_{\text{in}}$  [W/cm<sup>2</sup>]. The resulting responsivity  $\mathfrak{R} = V_{\text{out}}/E_{\text{in}}$  has the dimensions [V/(W/cm<sup>2</sup>)]. As stated in Chapter 2.1, this normalization is used to remove fluctuations in the response caused by fluctuations in the incident laser power.

The four-element array is biased at 100 mV and it is aligned following the procedure outlined in the appendix. Its H-plane radiation pattern is measured and plotted in Figure 15. Without adjusting the position of the device, the adjacent device used to determine the lead-line response contribution is also biased at 100 mV and its radiation pattern is measured. The measured radiation pattern of the four-dipole array is a superposition of the distributed antenna response and lead-line response. The distributed antenna response is determined by subtracting the two measurements from each other. The measured antenna response without lead-line contributions is also shown in Figure 15.

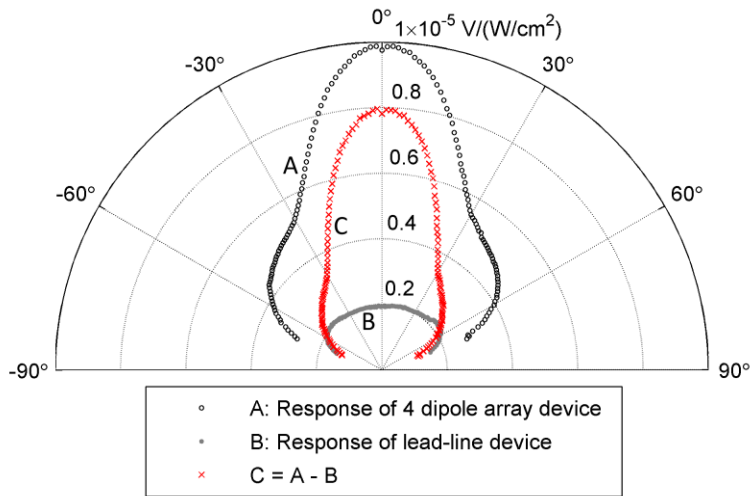


Figure 15: Measured H-plane radiation pattern of four-dipole array and lead-line response contribution device. Difference of these two measurements shows the distributed antenna response.

The radiation patterns of the remaining one-, two-, and three-dipole arrays and their corresponding lead-line response contribution devices are measured. The radiation patterns of only the distributed antenna responses are computed and are shown in Figure 16.

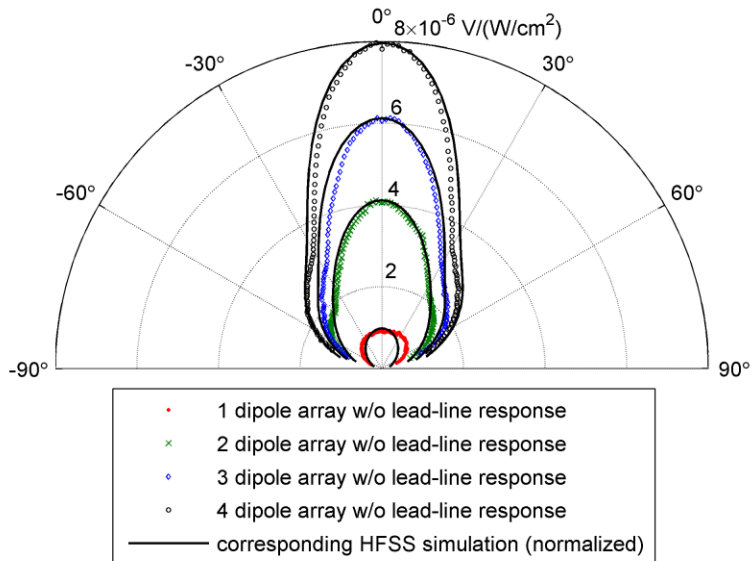


Figure 16: Measured radiation patterns without lead-line contributions of one-, two-, three-, and four-dipole arrays and corresponding simulated radiation patterns.

The measured radiation pattern of only the distributed antenna response are compared to the simulated radiation pattern in Figure 16. The magnitude of the simulated radiation patterns are proportional to the measured ones and each simulated pattern is normalized to the corresponding measured radiation pattern at broadside. The shape of the measured and simulated patterns show excellent agreement.

The measurement process outlined is time consuming since the measurement of two individual radiation patterns is required followed by the subtraction of the measured patterns. In the future, it may be more convenient to bias the two device simultaneously and connect their output to the difference input of a lock-in amplifier. The external electrical circuit would be similar to the one used in the measurement setup for the characterization of the orthogonal dipole in Chapter 2.3.2. This reduces the time requirement of the measurement process since the radiation pattern of the antenna response without the lead-line contributions is measured directly.

#### 2.4.5 Normalized measurement conditions

The previous section showed that using the method of subtracting the lead-line contribution from the measured antenna-array response yields excellent agreement with the predicted shape of the H-plane radiation pattern in HFSS. The simulation can be used to optimize the directional sensitivity of the antenna design. Figure 17 shows the same measured radiation patterns of the four investigated dipole arrays without the lead-line response contribution. The simulated patterns are similar to the previously shown ones in Figure 16, but they are normalized to the broadside response of the 4-dipole array, not the broadside response of each array. This normalization conserves the relative difference in magnitude of the one-, two-, three-, and four-dipole arrays as predicted by the HFSS simulation. The magnitudes of the

measured radiation patterns in Figure 17 show only modest agreement with the magnitude of the simulated patterns.

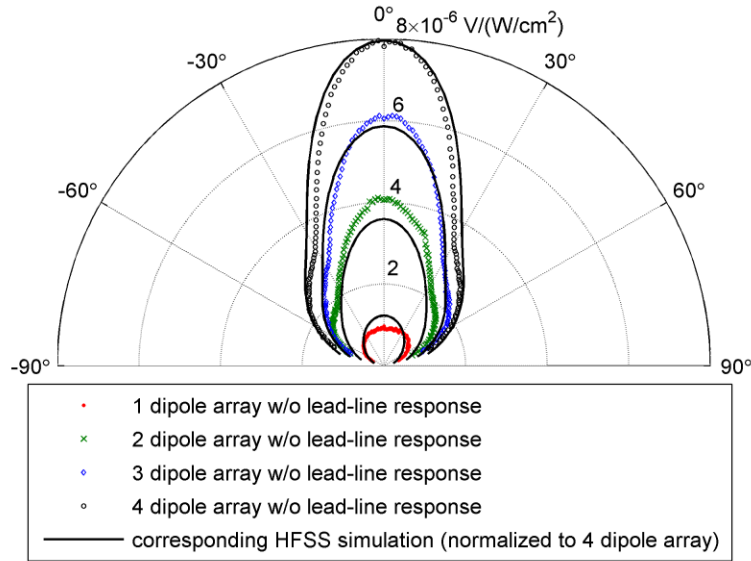


Figure 17: Measured antenna response without lead-line contributions of one-, two-, three-, and four-dipole arrays. The simulated radiation patterns are normalized to the broadside response of the measured 4-element pattern.

The conditions under which the H-plane radiation pattern of each device is measured are similar, but not identical. Due to fabrication tolerances, the resistance of each investigated device is not identical and varies from  $420 \Omega$  to  $516 \Omega$ . The goal of this section is to normalize the measured antenna response by accounting for the variations in the device resistance. The resistance of a bolometer is stated in Eq. (1), but can be simplified to

$$R = R(T_0) + \Delta R(\omega) , \quad (8)$$

where  $R(T_0)$  is the DC resistance of the investigated device.  $\Delta R(\omega)$  is the change in resistance caused by fluctuation in temperature due to illumination which is modulated at frequency  $\omega$ .

The measured voltage signal is caused by the change in the resistance of the device

$$V_s(\omega) = i_{\text{bias}} \cdot \Delta R(\omega) . \quad (9)$$



The temperature dependent part of the resistance is much smaller than the DC resistance of the device. Using this assumption, the bias current can be approximated as

$$i_{\text{bias}} \approx \frac{V_{\text{bias}}}{R(T_0)}. \quad (10)$$

Bolometers are commonly biased with a constant current source. The investigated devices, however, are biased with a constant voltage of 100 mV. Due to the variations of the resistance from device to device, the bias voltage is turned into a bias current that is not identical for each device. Using the median resistance of all measured devices,  $R_{\text{median}}(T_0)$ , the median bias current,  $i_{\text{median}}$ , can be expressed as

$$i_{\text{median}} \approx \frac{V_{\text{bias}}}{R_{\text{median}}(T_0)}. \quad (11)$$

The measured voltage signal of each individual device is then normalized to the median bias current. This calculation is performed by normalizing the device resistance

$$V_{s,\text{normalized}} = V_s \frac{i_{\text{median}}}{i_{\text{bias}}} = V_s \frac{R(T_0)}{R_{\text{median}}(T_0)}. \quad (12)$$

The measured radiation patterns of each antenna array and the corresponding lead-line contribution device are normalized using Eq. (12) before subtracting them from each other. The resulting radiation patterns are plotted in Figure 18. The simulated patterns are again normalized to broadside response of the four-element array and the relative difference in magnitude of the simulated patterns is preserved when comparing the four devices. Good agreement in shape and size of the radiation patterns for the four different array configurations is shown. The measured radiation pattern of the single dipole and three-dipole array show a small disagreement in the magnitude of the broadside response when compared to the corresponding simulated pattern. This difference is most likely caused by a small alignment error during the measurement process.

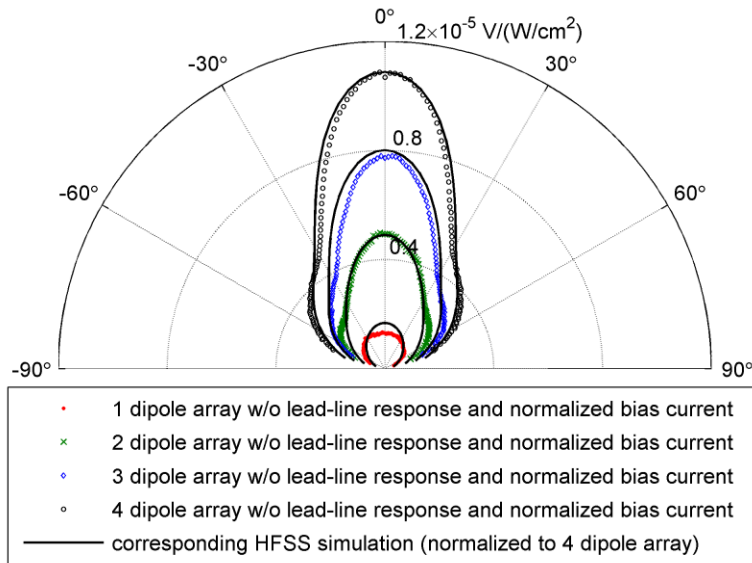


Figure 18: Measured antenna response without lead-line contributions of one-, two-, three-, and four-dipole arrays after normalizing the bias current. The simulated radiation patterns are normalized to the broadside response of the measured four-element pattern.

When accounting for the slight variations in the measurement setup, the simulation can be used to not only predict the shape of the radiation pattern, but also the relative difference in the magnitude of the response when comparing distributed bolometric antenna designs. This simulation approach can therefore be used to optimize a distributed antenna configuration by maximizing its response.

### CHAPTER 3: NEAR-FIELD MEASUREMENTS

The response of antenna-coupled detectors was measured and successfully calibrated to remove undesired response contributions in Chapter 2. The analysis of the electric field in close proximity to the detector can provide insight in the origins of the non-antenna-coupled response contributions. In the following experiment, a dipole antenna is used to couple far-field radiation into a CPS, which is then characterized by analyzing the measured near-field distribution along the transmission line. To accurately characterize the CPS, it is important to know if other mechanisms, besides the dipole antenna, couple radiation into the transmission line. These additional sources are first discovered in simulations of the dipole-coupled CPS and then confirmed by near-field measurements of the fabricated devices. In the characterization procedure of the CPS, these additional sources are calibrated by incorporating them into the analysis process.

The near-field measurement technique used in this experiment was originally developed to overcome the resolution limit of an optical microscope [47]. The electrical fields in close proximity to a structure, such as an infrared antenna, are composed of propagating and evanescent waves. Only the propagating fields can be analyzed in the far-field by an optical microscope and contain resolution limited information about the structure of interest. The evanescent waves contain more information, but decay quickly and do not propagate to the far-field. By positioning a sharp tip in close proximity of the structure of interest, the evanescent waves are locally scattered and converted into propagating waves that can then be analyzed in the far-field. In the experiments outlined, a s-SNOM is used to measure the near-field distribution on dipole-coupled infrared transmission lines. The operation principles of a s-

SNOM and the relation between the measured signal and the probed near-field distribution is explained.

The near-field measurements are used to determine the attenuation and propagation constants of an infrared CPS. The characterization of an infrared transmission line is of interest, since it can be used to separate the detector element from the antenna or as an interconnect between multiple antennas to form a phased-antenna array. The CPS is investigated, since its fabrication is straightforward and it can be integrated with planar detector designs.

Before the measured electrical near-field can be used to determine the attenuation and propagation constants of the infrared transmission lines, this analysis method has to be validated. At RF an analytical model has long been established and experimentally validated to characterize a CPS [48]. This analytical model and a HFSS simulation are used to determine the attenuation and propagation constants of the transmission line. The simulated near-field is then analyzed to determine the same constants. Agreement between these three methods shows that the CPS can be characterized by analyzing its near-field distribution.

In the experiment presented, an antenna is used to couple far-field radiation into the CPS to create a wave that propagates along the transmission line. The transmission line is terminated by an open- or a short-circuit load. The forward propagating wave is reflected at the termination and creates a standing wave. The attenuation and propagation constants are determined by fitting an analytical expression of the standing wave to the measured near-field distribution.

### 3.1 s-SNOM Setup

The s-SNOM measurement setup consists of two components: a Michelson interferometer and an AFM (CP-Research, Veeco Inc.) [49, 50]. The light source of the interferometer is a CO<sub>2</sub> laser operating at its main emission line of 10.6 μm. The one arm of the interferometer contains a movable mirror, which can adjust the phase of the reference light,  $E_{\text{ref}}$ . The other arm is illuminating the AFM, whose tip is locally scattering the near-field while raster scanning in non-contact mode across the device of interest.

The interferometer is not only used to illuminate the sample, but also to detect the scattered near-field. The interferometrically detected signal is amplified, since the interference of the scattered and reference fields,  $E_{\text{scat}}$  and  $E_{\text{ref}}$ , generates a signal that is proportional to  $(E_{\text{scat}} \cdot E_{\text{ref}})^{1/2}$ . A larger reference field can therefore amplify a smaller scattered signal. Since the signal amplification is facilitated by reference light with the same optical frequency, it is referred to as a homodyne optical system [51]. The light is detected with a mercury-cadmium-telluride (MCT) photodetector and the general s-SNOM measurement setup is shown in Figure 19 and Figure 20.

The plane of incidence of the light illuminating the dipole-coupled CPS is the xz-plane. The propagation vector of the incident light,  $E_{\text{in}}$ , forms a 60° angle with respect to the surface normal and it is focused to a spot with a diameter of about 30 μm using a Cassegrain objective with a numerical aperture of 0.5. Polarizing optics are used to ensure that  $E_{\text{in}}$  is polarized parallel to the axis of the dipole, which is the y-axis. As shown in Figure 19 and Figure 20, this corresponds to TE polarized incident light. The AFM records the topography of the investigated structure and synchronizes the recorded s-SNOM signal to it to create a spatial near-field map.

The incident light interacts with the dipole-coupled CPS and the AFM tip positioned directly above the antenna scatters light from the near-field,  $E_{nf}$ . The scattering locally converts the evanescent field components into propagating wave. Both TE and TM polarized light is scattered back into the Michelson interferometer,  $E_{scat}$ . The interferometer itself can only detect one polarization state at a time.

The configuration of the interferometer to detect the TE polarized light is shown in Figure 19.

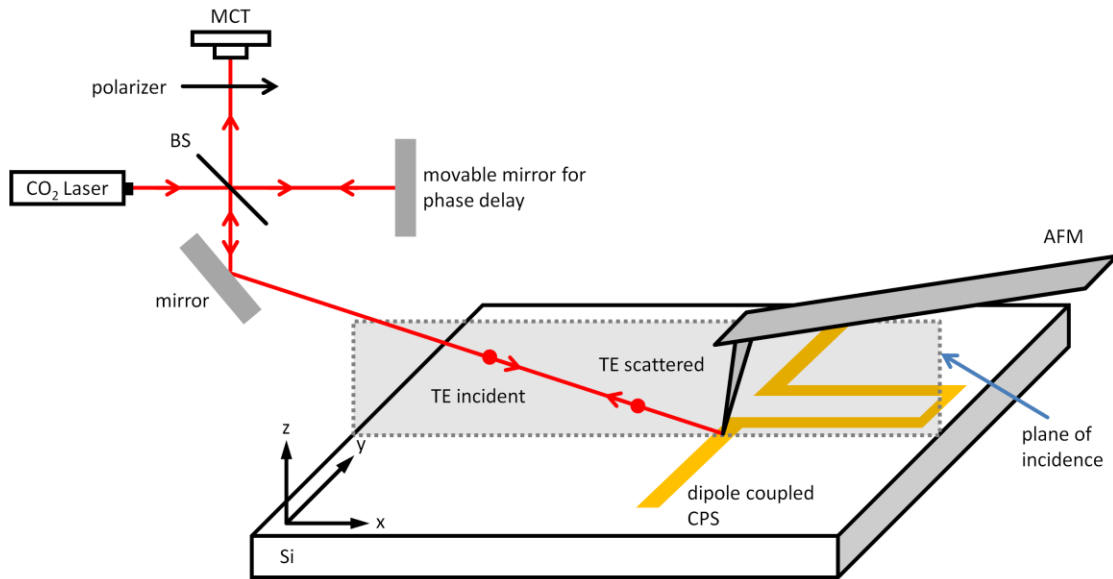


Figure 19: General s-SNOM setup for detection of TE scattered light.

The light incident on the interferometer is TE polarized. The beam splitter has no effect on the polarization and so the light illuminating the dipole-coupled CPS is still TE polarized, i.e. parallel to the axis of the dipole. The TE and TM polarized components of the near-field are scattered by the AFM tip back into the interferometer. The light in the reference arm is also polarized in the TE direction and the polarizer in front of the MCT is oriented to only pass this

polarization state and attenuate the scattered light with any other polarization state. The interference of the TE polarized light from the two arms of the interferometer is detected.

The interferometer has to be modified to detect the TM scattered near-field as illustrated in Figure 20. Once again, the light incident on the interferometer is TE polarized, such that the light transmitted to the dipole-coupled CPS is polarized parallel to the axis of the dipole. The near-field scattered back into the interferometer is TE and TM polarized. A quarter-wave plate is inserted in the reference arm and the reference light passes through it twice, effectively rotating its polarization by  $90^\circ$  to the TM state. The light from the two arms of the interferometer are combined at the beam splitter and only the TM polarized components pass through the properly oriented polarizer and interfere at the MCT.

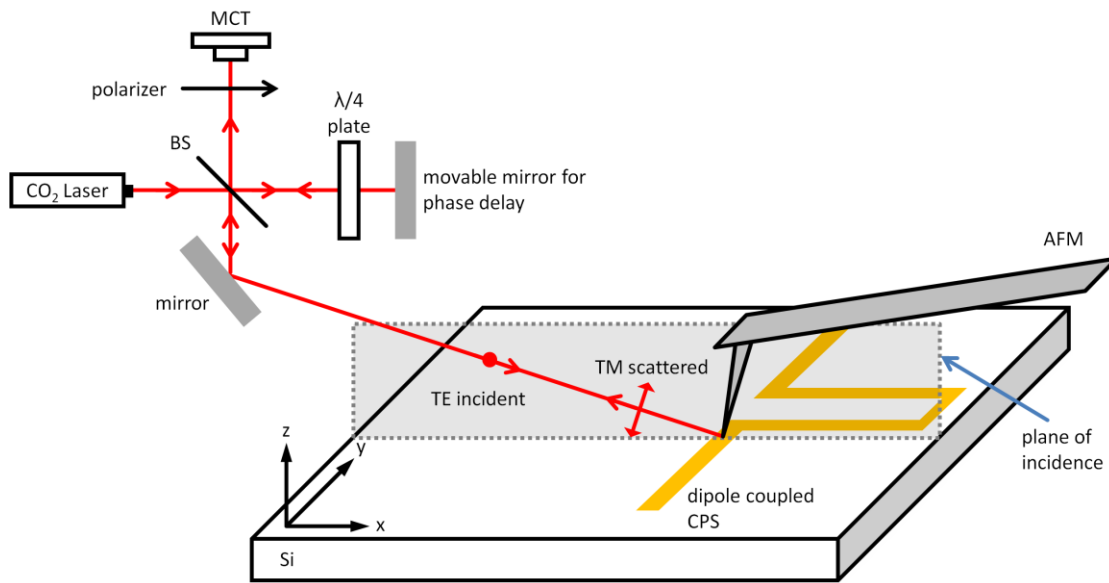


Figure 20: General s-SNOM setup for detection of TM scattered light.

The light that is returned back into the interferometer is not only composed of the near-field distribution that is scattered by the AFM tip. Some of the incident radiation is also reflected off the tip, its shaft, or directly off the sample. Of these field distributions, only the near-field

component varies rapidly in the z-direction. The tip of the AFM is oscillating in the z-direction over a short range of about 30 nm [52]. A lock-in amplifier is used to record the optical signal from the MCT. In the experiments presented, the lock-in amplifier is referenced to the second harmonic of the tip dither frequency allowing the suppression of the background radiation and recording of only the near-field component [53]. Details of this background suppression are discussed in Chapter 3.2.

The electric near-field in the following experiments is scattered with platinum coated silicon tips (NanoWorld Arrow<sup>TM</sup> NCPt). Due to their long and narrow geometry, these tips scatter predominately the TM polarized light, which corresponds to the  $E_z$  field component. To perform a s-SNOM measurement, it is necessary to perturb the electrical near-field. Ideally, this perturbation is kept to a minimum, while still scattering enough of the near-field to detect a signal. Dielectric tips are ideal candidates, since they do not greatly perturb the near-field surrounding the sample [14]. The metallized tips scatter the light more efficiently, resulting in a larger response, but at the price of a larger field perturbation. Measurements of antenna structures using silicon and metallized AFM tips yielded identical field distributions [49, 50], indicating that the metallized tips scattered the near-field more efficiently, while not greatly altering the near-field distribution and therefore not affecting the behavior of the investigated antennas.

The measurement of the TE field component requires a modified tip with an appropriate scatter function to access this field component selectively. This has been accomplished by attaching a gold nanoparticle to the apex of a AFM tip [54]. A different approach is to truncate a silicon-AFM tip using focused ion beam milling and depositing platinum by chemical vapor



deposition on the newly created plateau. This platinum disk has an approximate diameter of 200 nm and it is oriented perpendicular to the axis of the AFM tip. This modified tip is capable of scattering the TE field component more efficiently than the unmodified tip. Details of this modification and measurements will be discussed elsewhere.

The scanning of the s-SNOM measurement is accomplished by moving the sample in the xy-plane with respect to the tip, which dithers minutely in the z-direction. The incident beam is large compared to the sample and illuminates it quasi-uniformly. The scattered light is collected by the Cassegrain objective, which is aligned to image the AFM tip. By not moving the tip in the xy-plane, the Cassegrain objective does not have to be constantly realigned throughout the near-field measurement to continually image the AFM tip.

### **3.2 Concept of s-SNOM Operation**

The near-field measurement is made feasible by locally converting the evanescent field components surrounding the structure of interest into propagating fields using an AFM tip. The interferometer is used to perform homodyne amplification to determine the amplitude and phase of the scattered field, which is proportional to the near-field. Due to the modulation of the AFM tip, the detected signal is related to the gradient of the optical near-field in the z-directions. A simple approximation is that a measured signal with a large magnitude indicates a region with a high optical field gradient which corresponds to a region with a large electrical near-field distribution. Since the near-field distribution decays exponentially in the z-direction away from the sample, this approximation can be used, but a more detailed description of the interaction of the oscillating AFM tip with the near-field distribution is of interest. In the following section,

the exponentially decaying near-field is related to the detected signal at the output of the Michelson interferometer. This mathematical description follows [55].

Let us assume an illuminated structure that extends in the  $xy$ -plane. The magnitude of the electric near-field surrounding this structure decays exponentially in the  $z$ -direction.

$$E_z(z) = E_0 e^{-\left(\frac{z}{d_0}\right)}. \quad (13)$$

The AFM tip dithers at frequency  $\omega_d$ . Its position in the  $z$ -direction varies sinusoidally over time

$$z(t) = d + a(1 + \cos(\omega_d t)). \quad (14)$$

The tip is oscillating at an average height of  $d + a$  above the illuminated structure with an amplitude of  $a$ . During the oscillations, the tip never approaches the surface closer than the distance  $d$ . This motion of the AFM tip is illustrated in Figure 21.

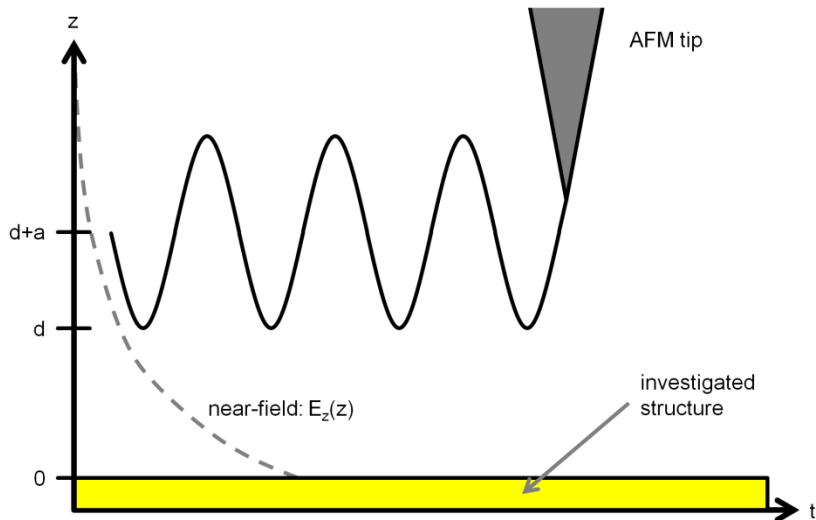


Figure 21: Graphical representation of dithering AFM tip in near-field.

The scattered field is proportional to the near-field under the condition that the amplitude of the AFM tip oscillation remains within the decaying field.

$$E_{\text{scat}} \propto E_z \quad (15)$$

For this illustration, the scattered field is equated to the near-field described in Eq. (13).

The exponential term is expanded using a power series

$$E_{\text{scat}}(z, t) = E_0 \left( 1 - \frac{z}{d_0} + \frac{z^2}{2d_0^2} - \dots \right) e^{j(\omega t + \Phi_{\text{nf}})} . \quad (16)$$

The scattered near-field has a phase of  $\Phi_{\text{nf}}$ , and the assumption that the phase of the near-field component does not vary in the z-direction over the oscillation range of the AFM tips is made. The position of the oscillating tip, as described by Eq. (14), is inserted into the scattered electric field in Eq. (16). By expanding and collecting the resulting terms the scattered near-field can be expressed as a Fourier series.

$$E_{\text{scat}}(t) = \sum_{n=0}^2 E_0 A_n \cos(n \omega_d t) e^{j(\omega t + \Phi_{\text{nf}})} . \quad (17)$$

The Fourier coefficients are given by:

$$A_0 = 1 - \frac{a+d}{d_0} + \frac{2d^2 + 4ad + 3a^2}{4d_0^2} \quad (18)$$

$$A_1 = -\frac{a}{d_0} + \frac{a(a+d)}{d_0^2} \quad (19)$$

$$A_2 = \frac{a^2}{4d_0^2} \quad (20)$$

The detected signal in the Michelson interferometer is the interference of the scattered field and the reference field, which is stated as

$$E_{\text{ref}} = E_r e^{j(\omega t + \Phi_{\text{ref}})} . \quad (21)$$

The amplitude of the reference field,  $E_r$ , is adjustable. The phase  $\Phi_{\text{ref}}$  is relative to the scattered near-field and it can be adjusted by moving the mirror in the interferometer's reference arm in Figure 20. The two fields sum in the interferometer to create the output field

$$E_{\text{out}}(t) = E_{\text{ref}}(t) + E_{\text{scat}}(t) , \quad (22)$$

$$E_{\text{out}}(t) = E_r e^{[j(\omega t + \Phi_{\text{ref}})]} + \sum_{n=0}^2 E_0 A_n \cos(n \omega_d t) e^{[j(\omega t + \Phi_{\text{nf}})]} . \quad (23)$$

The MCT does not detect the fields, but their intensity which is given by

$$I_{\text{out}}(t) = E_{\text{out}}(t) \cdot E_{\text{out}}^*(t) . \quad (24)$$

Expanding this expression and collecting the terms, the result can be expressed as the following series

$$I_{\text{out}}(t) = \sum_{n=0}^4 I_n \cos(n \omega_d t) . \quad (25)$$

The first or second harmonic is usually investigated for s-SNOM measurements. The background suppression is greater at higher harmonics at the price of a smaller magnitude of the detected signal [53]. In the following experiment, the second harmonic is recorded, which was the highest harmonic to provide a signal with a sufficiently large magnitude. It is expressed as

$$I_{\text{out},2} = 2E_r E_0 A_2 \cos(\Phi) + 2E_0^2 A_0 A_2 + \frac{E_0^2 A_1^2}{2} . \quad (26)$$

The recorded intensity is modulated by the term  $\Phi = \Phi_{\text{ref}} - \Phi_{\text{nf}}$ , which is the phase difference between the reference and scattered signal. The s-SNOM signal is recorded by a lock-in amplifier that also measures the phase of the detected signal. If the reference field and the scattered near-field are in phase, the detected signal is maximized. If the two fields are out of phase, the detected signal is also maximized, but its phase is reversed by 180°.

In the s-SNOM setup, the Gaussian beam illuminating the sample is large and other parts of the setup are also illuminated. Some of the light is reflected of the tip, its shaft, or the sample. The magnitude of these components does not vary as rapidly in the z-direction as the near-field and therefore do not contribute to the measured intensity at the second harmonic of the tip dither frequency. However, a small part of the reflected light is modulated by the motion of the tip and

contributes to the measured signal. This contribution is approximated as a constant offset to the measured signal when analyzing the measured near-field above the dipole-coupled CPS.

### 3.3 HFSS Simulation of Near-Field Distribution

The near-field measurements are simulated using HFSS. The layout of the simulation volume is shown in Figure 22. For this illustration, the device of interest is a dipole-coupled CPS. The device is composed of gold and it is located at the silicon-air interface, which forms the xy-plane. The axis of the dipole is parallel to the y-axis and the CPS consists of two parallel conductors extending along the x-axis. The CPS in this example is terminated with a short-circuit load, which is a gold strip connecting the two conductors of the CPS. The relative permittivity of gold and silicon at 28.3 THz are listed in Table 2. The material properties are assigned to the appropriate structures in the simulation.

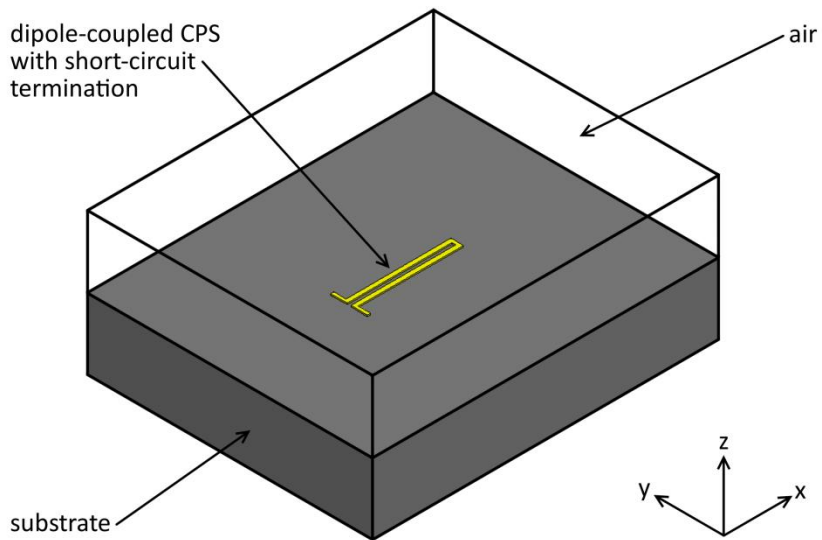


Figure 22: HFSS setup of s-SNOM simulation

The device is illuminated from the air side by a Gaussian beam with a radius of  $13\ \mu\text{m}$  at its focus, where the beam has an electric field strength of  $1\ \text{V/m}$  and is polarized parallel to the

axis of the dipole. The beam is incident onto the device in the  $xz$ -plane, forming a  $60^\circ$  angle with the  $z$ -axis and its focus of the beam is located at the center of the dipole.

The solution volume is terminated with the PML boundary. This ensure that any radiation incident on this boundary will be attenuated, resulting in no back reflections and essentially approximating that the solution volume has infinite extent.

The simulation determines the complex electric field everywhere within the simulation volume. The electric field 20 nm above the dipole-coupled CPS is exported for comparison with the measured data and further analysis.

### **3.4 CPS Characterization**

The use of metallic transmission lines at optical and infrared frequencies has the advantage of a smaller footprint when compared to dielectric waveguides [19, 20] and can potentially reduce the size of integrated optics. Employing metallic transmission lines in antenna designs opens the possibility to separate the detecting element from the antenna. The signal propagates along the transmission line with its phase preserved. Properly designed antenna arrays with interconnects consisting of these transmission lines are phased arrays. The shape the radiation pattern of phased arrays is directional and can be modified by altering the properties of the transmission line interconnects.

Metallic transmission lines have been extensively studied at RF frequencies. Measurements in this frequency range are conducted using a vector network analyzer (VNA), where a wave is launched into the device under test and the device is characterized based on the reflected and transmitted waves [56]. Several types of RF transmission lines could be used at

infrared frequencies. The microstrip consists of a conducting strip that is separated from a ground plane by a dielectric standoff layer and the guided mode is confined inside the dielectric standoff layer. Another popular RF transmission line is the slotline. This is the complementary structure to the microstrip. A conducting sheet with a slot is separated from a ground plane by a dielectric standoff layer and the propagating mode is also confined within the standoff layer.

The CPS is an alternative to these two transmission lines and consists of two conducting strips that are located on a dielectric substrate. This design is chosen for the following experiments, since it is straightforward to fabricate and it can be integrated with planar antenna designs. A cross-sectional view of a CPS is shown in Figure 23.

The experimental characterization of the CPS is essential to develop a better understanding of the transmission line, which can lead to an optimization of its performance. A VNA operating at IR frequencies is not available and a different measurement approach has to be used. In our experiment, the electrical near-field distribution along the CPS at 28 THz is measured using a s-SNOM and the measured near-field distribution is analyzed to determine the attenuation and propagation constant of the CPS.

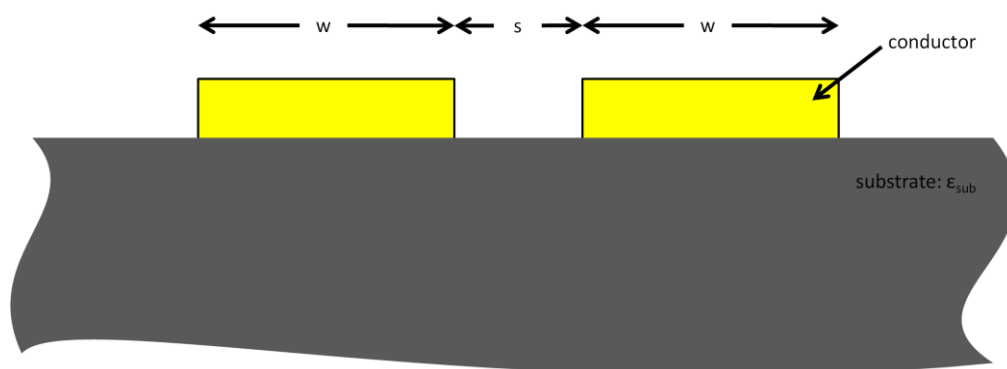


Figure 23: Cross section of a coplanar strip line.

The first part of the experiment is to validate that it is possible to extract the attenuation and propagation constants from the near field data. A low frequency, 10 GHz, CPS is simulated and the constants obtained from the analyzed near-field are compared to the constants derived from an analytical expression and to the ones directly obtained from the HFSS simulation. Excellent agreement in the values gives confidence that this analysis approach is valid. Further, based on simulations, a similar transmission line characterization using near-field analysis has been proposed elsewhere [57].

In the experiment a dipole antenna is used to couple far-field radiation into the CPS. The electromagnetic wave created thusly travels along the transmission line and is reflected at its termination. The reflected wave interferes with the forward propagating one and creates a standing wave. This is measured with the *s*-SNOM and the attenuation and propagation constants of the CPS are determined by fitting the analytical expression of the standing wave to the measured field distribution along the transmission line. Two nominally identical dipole-coupled transmission lines are investigated. One is terminated by an open-circuit load and the other one by a short-circuit load. Ideally, these two different terminations should not influence the attenuation and propagation constants of the transmission line; they will merely shift the locations of the minima and maxima of the standing wave in the near-field distribution.

The incident radiation of the measurement setup is not only illuminating the dipole of the antenna-coupled CPS, but the entire transmission line as well. The geometry of the conductors of the CPS does not allow for the incident radiation to couple into the transmission line. However, this is not the case for the short-circuit load, which is a metal strip connecting the two conductors. This strip is oriented in the same direction as the dipole antenna and it couples some



of the incident radiation into the CPS, creating an additional standing wave. The analytical expression of the standing wave is modified for calibration purposes to take into account this additional source of the standing wave before fitting it to the measured near-field distribution to determine the attenuation and propagation constants of the transmission line.

### 3.4.1 Validation of measurement approach

The purpose of this experiment is to determine the attenuation and propagation constants of a CPS at 28.3 THz. At RF, transmission lines are commonly characterized using a VNA. This technology is not available at IR frequencies and a different measurement approach has to be used. The near-field distribution above the transmission line can be measured using a s-SNOM. To show that the attenuation and propagation constants of the CPS can be determined from the near-field distribution, a RF CPS is analyzed using three different methods.

In the first approach an analytical expression is used to determine the effective dielectric constant of the transmission line. This information is then used to determine the propagation constant of the CPS. The second method is to simulate the transmission line in HFSS, which provides the attenuation and propagation constant of the CPS directly. The third approach is to extract the near-field distribution from the simulated CPS in the second approach. The analytical expression describing the standing wave on the transmission line is fitted to the simulated near-field to determine the attenuation and propagation constants. By showing that the constants characterizing the CPS determined by these three methods agree, the analysis approach using the near-field distribution is validated.

The CPS used for the validation of the near-field characterization approach is operating at 10 GHz, corresponding to a free-space wavelength  $\lambda_0 = 30$  mm. The dimensions of the CPS

layout shown in Figure 23 are  $w = 300 \text{ } \mu\text{m}$ ,  $s = 200 \text{ } \mu\text{m}$ . The substrate is lossless and has a dielectric constant of  $\epsilon_{\text{sub}} = 11.9$ . To further ensure that the transmission line is lossless, the conductors are two dimensional sheets of perfect electric conductors. This CPS is analyzed using three methods outlined in the following sections.

### 3.4.1.1 Analytical method

An analytical expression is used to determine the effective dielectric constant encountered by the guided mode [48]. This expression assumes that the transmission line is lossless.

$$\epsilon_{\text{eff}} = 1 + \frac{\epsilon_{\text{sub}} - 1}{2} \frac{K(k')K(k_1)}{K(k)K(k'_1)} \quad (27)$$

The dielectric constant of the substrate is  $\epsilon_{\text{sub}}$ .  $K(\cdot)$  is the complete elliptic integral of the first kind. The arguments of the elliptic integrals are determined as follows

$$k = \frac{s}{2w+s} \quad (28)$$

$$k' = \sqrt{1 - k^2} \quad (29)$$

$$k_1 = \sinh\left(\frac{\pi s}{4h}\right) / \sinh\left(\frac{\pi(2w+s)}{4h}\right) \quad (30)$$

$$k'_1 = \sqrt{1 - k_1^2} \quad (31)$$

In Eq. (30) the variable  $h$  is the height of the substrate, which in the case of an ideal CPS is infinite. In the calculation this value is equated to  $60 \text{ mm}$ , which corresponds to twice the free-space wavelength. Solving this equation for a set of different values for the substrate height showed that this value did not have any impact on the evaluated value of  $\epsilon_{\text{eff}}$  if  $h$  is larger than the free space wavelength. The guided wavelength is calculated from  $\epsilon_{\text{eff}}$  using  $\lambda_{\text{eff}} = \lambda_0 / \sqrt{\epsilon_{\text{eff}}}$ . The propagation constant is then determined as  $\beta = 2\pi/\lambda_{\text{eff}}$ . Since this analytical

formulation assumes no loss in the transmission line, the attenuation constant  $\alpha$  is zero. The results are summarized in Table 6.

### 3.4.1.2 HFSS simulation method

The HFSS simulation of the low-frequency CPS is different from the previously discussed simulations. The transmission line is not excited by a plane wave, but an electric field is directly applied to its edges at each end of the CPS. The layout of the simulation volume is shown in Figure 24. It consists of a substrate,  $\epsilon_{\text{sub}} = 11.9$ , and a volume of air. The two strips forming the CPS are two-dimensional sheets that are in direct contact with the boundary of the simulation volume. The CPS is 20 mm long and the PEC material property is assigned to it. The material properties are consistent with the ones used in the analytical analysis section to validate the near-field-analysis approach.

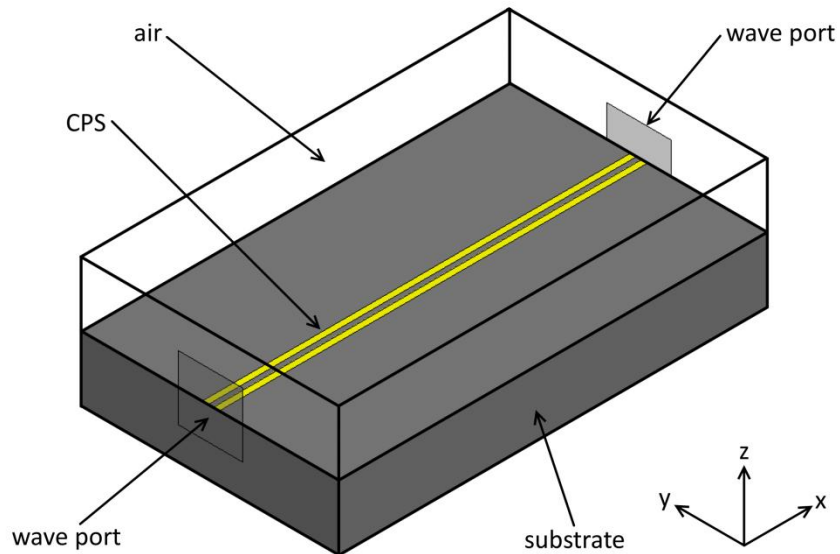


Figure 24: HFSS layout of low-frequency CPS simulation.

The transmission line is excited by two wave ports, one at each end. The port represents the area where energy enters the solution volume. Incident radiation is polarized in the  $y$ -

direction, which coincides with the polarization of the propagating mode along this type of transmission line. The port is a perfect termination for the setup, so that the wave originating from one port is absorbed in the other port and no back reflections occur. In this simulation, both wave ports excite the CPS simultaneously. The two waves travel in opposite directions and interfere with each other creating a standing wave.

The boundaries on the two sides containing the wave ports are assigned the "perfect H" boundary condition. This setup enforces that the electric field entering the CPS is only allowed to be polarized in the yz-plane. All other boundaries of the solution volume are terminated with the radiation boundary.

Simulations using wave ports will determine the propagation and attenuation constants of the transmission line that are in direct contact with them. The effective wavelength of the propagating mode is also evaluated. These simulated properties are summarized in Table 6.

This type of simulation, where a wave port is used to excite a transmission line, does not work at IR frequencies when using realistic material properties and dimensions. The current version of HFSS, v.12.0.1, does not allow a material with a negative real part of the dielectric constant, e.g. gold at 28.3 THz, to be in direct contact with the wave port.

#### *3.4.1.3 Near-field method*

The simulation that determines the attenuation and propagation constants of the CPS also computes the complex electric field everywhere inside the simulation volume. The electric field 50  $\mu\text{m}$  above the CPS is shown in Figure 25. The magnitude of the  $E_y$  and the  $E_z$  field components are plotted, since the s-SNOM setup is capable of selectively measuring either of these field components.

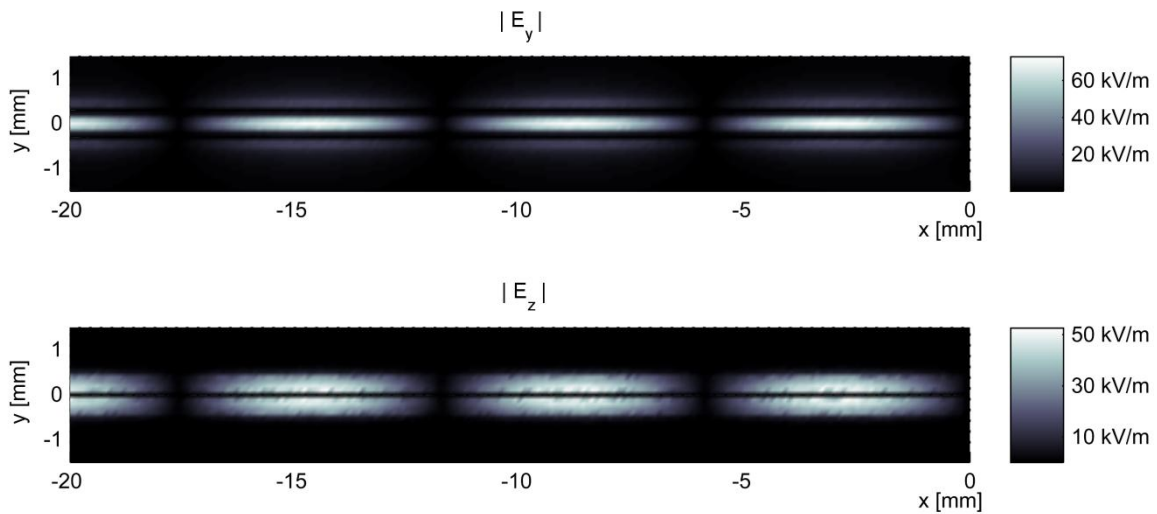


Figure 25: Simulated magnitude of  $E_y$  and  $E_z$  above CPS at 10 GHz.

A cross section of a CPS in Figure 26 illustrates the typical field distribution by plotting the real part of the electric field. The electric field between the two conductors,  $E_y$ , is the guided mode and it is the largest in magnitude. A byproduct of the mode are the  $E_z$  components of the field distribution on top of the conductors.

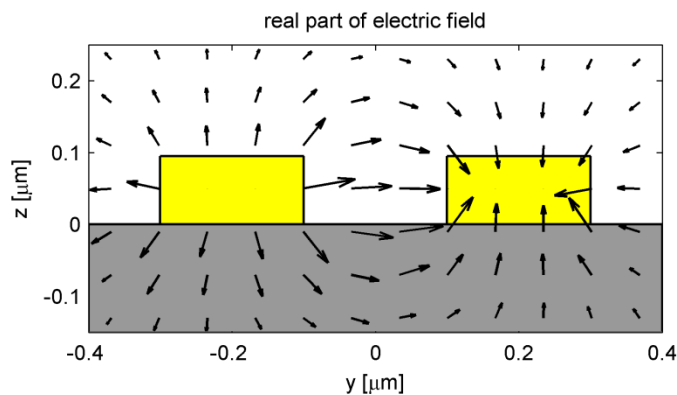


Figure 26: Typical mode structure on CPS.

The standing wave can be expressed analytically as a function of the electric field along the transmission line [13]. It consists of a forward propagating wave, which is reflected at the load and then travels in the opposite direction. It is stated as

$$E(x) = E_0 [e^{-(\alpha+j\beta)x} + \Gamma e^{(\alpha+j\beta)x}], \quad (32)$$

where  $E_0$  is the electric field strength of the propagating wave at the load,  $\alpha$  and  $\beta$  are the attenuation and propagation constants, and  $\Gamma$  is the reflection coefficient. The wave originates at  $x = -\infty$  and propagates in the positive  $x$ -direction. It is reflected at the load, which is located at  $x = 0$ . The reflected wave propagates then in the negative  $x$ -direction. The reflection coefficient determines how much of the incident wave is reflected. An ideal short-circuit termination, for example, has a reflection coefficient of -1, indicating that all of the incident wave is reflected with a  $180^\circ$  phase shift.

The parameters of the standing wave equation are determined by fitting the magnitude of Eq. (32) to the magnitude of the simulated near-field data. In order to determine which field component of the near-field data should be used to determine the attenuation and propagation constants from the fitting procedure, the magnitude of the  $E_y$  component between the two conductors and the magnitude of the  $E_z$  component on top of one of the conductors are plotted in Figure 27.

Analysis of the plotted field distributions show that  $E_y$  and  $E_z$  are proportional to each other. The value of  $E_0$  in Eq. (32) can be thought of as a normalization constant that can relate  $E_z$  to  $E_y$ . The attenuation and propagation constant describing the transmission line can be determined from either field distribution. Only the  $E_z$  component of the field distribution on the CPS is measured with the s-SNOM using commonly available and unmodified AFM tips. The magnitude of this field component is smaller than the  $E_y$  component located between the two conductors of the CPS, but the measurement setup is more straightforward since an unmodified AFM tip can be used.

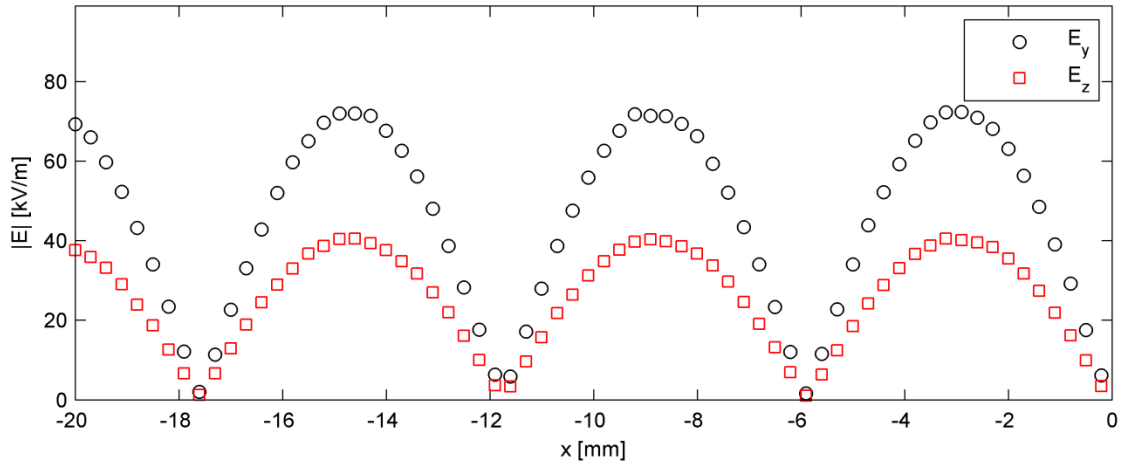


Figure 27: Magnitude of  $E_y$  and  $E_z$  along 10 GHz CPS.

Another interesting aspect of the  $E_z$  field component on top of the two conductors is that they are identical in magnitude, but  $180^\circ$  out of phase. This is illustrated in Figure 28.

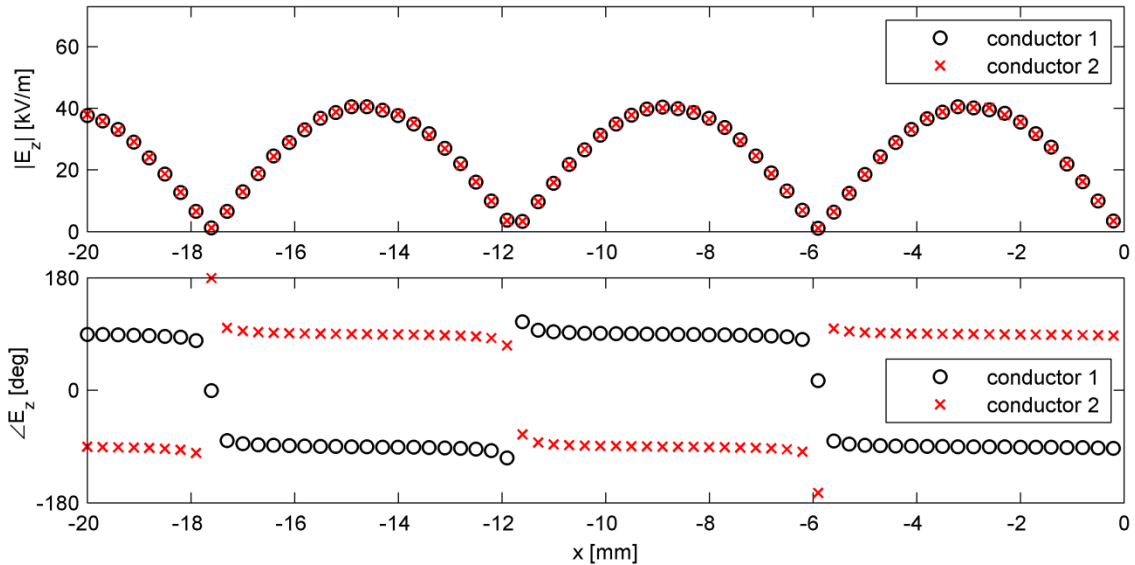


Figure 28: Comparison of magnitude and phase of  $E_z$  on the two conductors of the CPS.

A single s-SNOM measurement of the CPS contains therefore the same information about amplitude and phase that one would otherwise obtain by measuring the investigated device for a second time after introducing a  $180^\circ$  phase delay in the reference beam of the interferometer.

The magnitude of Eq. (32) is fitted to the magnitude of the  $E_z$  field component using a non-linear fitting algorithm that minimizes the sum square of errors. The parameters that are allowed to vary during the fitting process are  $\alpha$ ,  $\beta$ ,  $\Gamma$ , and  $E_0$ . The fit is shown in Figure 29.

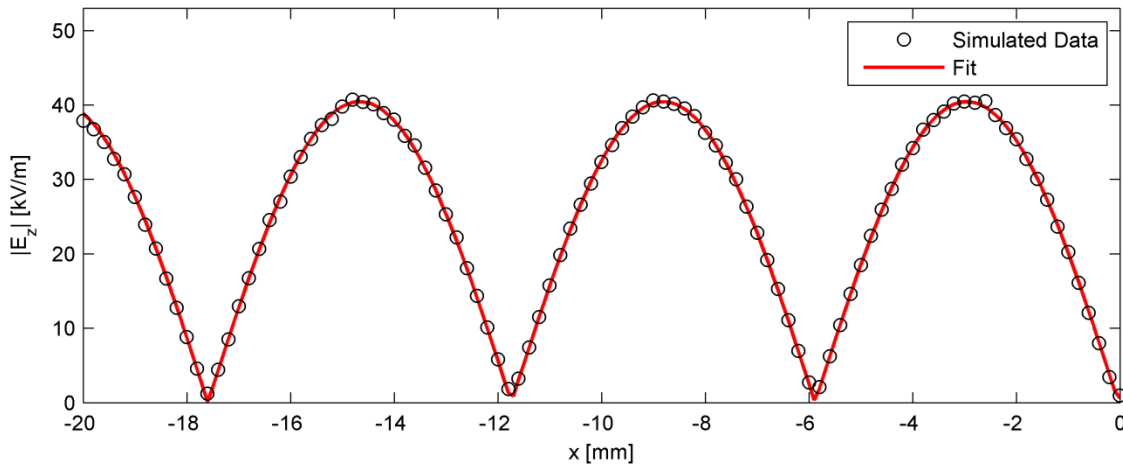


Figure 29: Standing wave equation fitted to simulated near-field.

Table 6 compares the attenuation, propagation constant and the derived effective wavelength of guided mode determined by the three discussed methods. The first one uses an analytical expression describing the effective dielectric constants of the propagating mode. The second one is the simulation of the CPS in HFSS, which directly computes the attenuation and propagation constants of the CPS. The third approach is to analyze the simulated electric near-field above the CPS to determine the properties of the transmission line.

Table 6: Parameters characterizing the 10 GHz CPS.

Method	$\alpha$ (1/m)	$\beta$ (rad/m)	$\lambda_{\text{eff}}$ (mm)
Analytical	0	531.9	11.8
HFSS	0	535.3	11.7
Near-field	$1.4 \cdot 10^{-4}$	536.5	11.7



The values of the attenuation and propagation constant and the effective wavelength determined using the three methods show great agreement. A small value of the attenuation constant is obtained by fitting the standing wave equation to the near-field data. Even though it is non-zero, it is small enough to be ignored when comparing it to the size of the wavelength. This agreement validates the approach of determining the attenuation and propagation constants from near field data and it is therefore applied to measurements of the infrared CPS at 28.3 THz.

#### 3.4.2 Simulation of near-field distribution along infrared CPS

The simulation of the infrared CPS is conducted to establish a model of how to analyze the near-field distribution to determine the attenuation and propagation constant of this transmission line. These values will then be compared to the constants determined from the measured CPS. Two identical CPS will be analyzed; they only differ in the type of their termination. The first transmission line is terminated by an open-circuit load and the second one is terminated by a short-circuit load. Since the CPS are identical, their attenuation and propagation constants should also be the same. The different types of termination merely shift location of the maxima and minima of the standing wave.

The following section discusses the antenna design used to couple far-field radiation into the transmission line to create a propagating mode. This is followed by the analysis of the simulated near-field distributions of the dipole-coupled CPS with the open- and short-circuit terminations.

A dipole antenna is used to couple far-field radiation into the CPS, which is oriented perpendicular to the conductors of the CPS. The incident radiation is polarized parallel to the axis of the dipole and perpendicular to the conductors of the CPS and should therefore only

minimally interact with the conductors directly. The length of the dipole antenna is determined similar to the approach used in Chapter 2.3.1. An isolated dipole is simulated as a radiating antenna and its input impedance is determined as a function of the antenna length. This is plotted in Figure 30. The dipole is located at the interface between silicon and air. It is a 150-nm-wide two-dimensional sheet. The input impedance has no inductive component for a length of 1.8  $\mu\text{m}$ . At this length all of the energy introduced to it at its feed point will be transmitted.

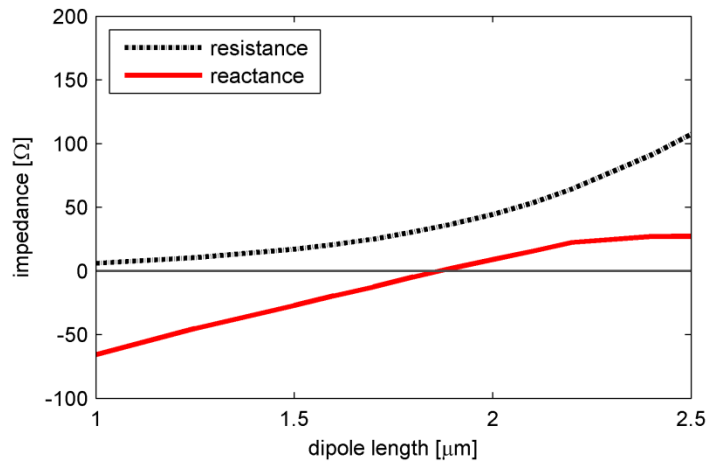


Figure 30: Input impedance of isolated dipole at silicon-air interface.

The simulated length of the dipole is shorter than its calculated length using the effective media formula described in Chapter 2.3.1. The effective half wavelength at a silicon-air interface is 2.1  $\mu\text{m}$ . This formulation does not take into account the finite width of the dipole. The resonance frequency of a wide dipole is shifted to lower frequencies when compared to an infinitely thin dipole of the same length [58]. In order to restore the desired resonance frequency, the length of the dipole antenna has to be reduced.

The length of the CPS is another design consideration. Maximizing its length will simplify the data analysis, since more maxima and minima in the standing wave can be observed. The attenuation of a CPS at IR frequencies is expected to be quite large [22], which will reduce

the visibility of the standing wave and make measurement and analysis more difficult. The final length of 5  $\mu\text{m}$  is selected, since simulations indicate that the magnitude of the standing wave has almost three maxima along the CPS. This should be sufficient for analysis of the measured data.

#### 3.4.2.1 Open-circuit terminated CPS

The first of the two investigated transmission lines is the dipole-coupled CPS that is terminated in an open-circuit load. The conductors of the CPS are 220 nm wide and separated by 110 nm. They are 110 nm thick and like the dipole antenna are also composed of gold. The open-circuit termination is located at the end of the transmission line opposite to the end that is connected to the dipole antenna. The region of the open-circuit termination is left empty. The layout of the device is shown in Figure 31.

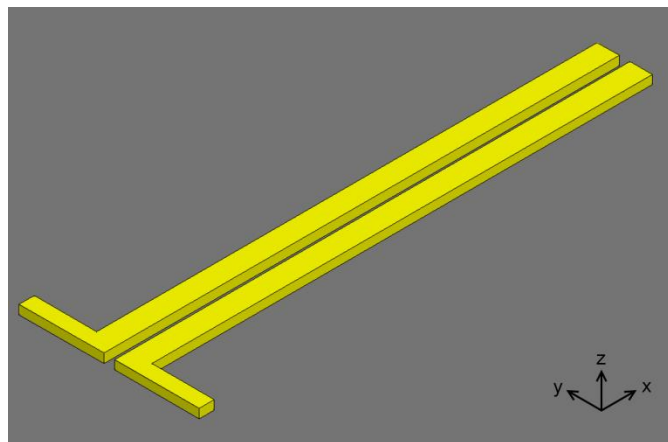


Figure 31: Layout of dipole-coupled CPS with open-circuit termination.

The simulation of this device, as described in Chapter 3.3, determines the complex electric field everywhere inside the simulation volume. The  $E_z$  component 20 nm above one of the two conductors is extracted and Figure 33 shows the magnitude of this component.

The incident beam is illuminating the entire structure of the CPS, not just the dipole. To ensure that the incident beam is not interacting with the transmission line directly and creating field distributions in addition to the standing wave, only the CPS structure is simulated. This layout is shown this in Figure 32.

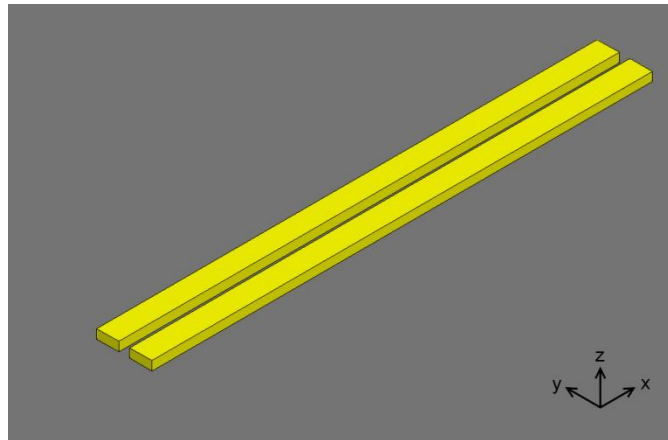


Figure 32: Layout of open-circuit-terminated CPS without dipole antenna.

The simulated field distribution above one of the conductors of the CPS without the dipole antenna is extracted and also plotted in Figure 33. In this plot, the open circuit termination is located at  $x = 0 \mu\text{m}$  and the other end of the CPS that is closest to the dipole is located at  $x = -5 \mu\text{m}$ .

Figure 33 shows that the near-field distribution above the CPS without the antenna is negligible, indicating that only the dipole antenna is coupling far-field radiation into the transmission line. Further, the magnitude of the maxima and minima in the simulated standing wave in the near-field distribution above the dipole-coupled CPS decrease in size as the open-circuit terminated end is approached. This property is consistent with a standing wave pattern along a lossy transmission line.

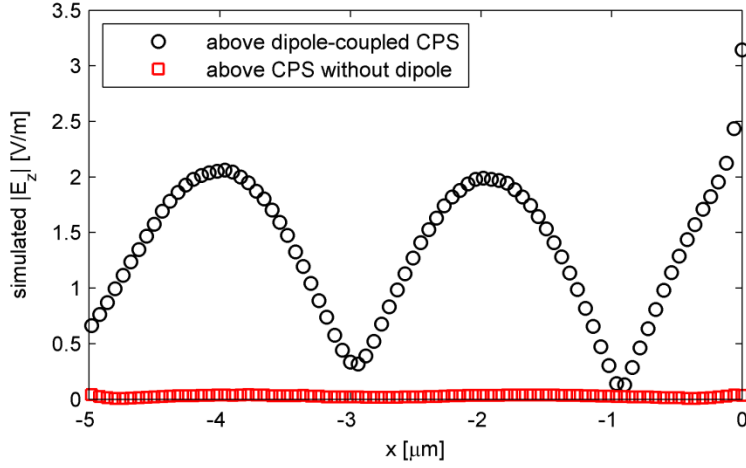


Figure 33: Simulated magnitude of  $E_z$  above one conductor of the open-circuit terminated dipole- and non-dipole-coupled CPS.

The magnitude of the analytical description of the standing wave in Eq. (32) is fitted to the magnitude of the standing wave on the CPS in Figure 34. The parameters that are allowed to vary during the fitting process are  $\alpha$ ,  $\beta$ ,  $\Gamma$ , and  $E_0$ . Their values are summarized in Table 7.

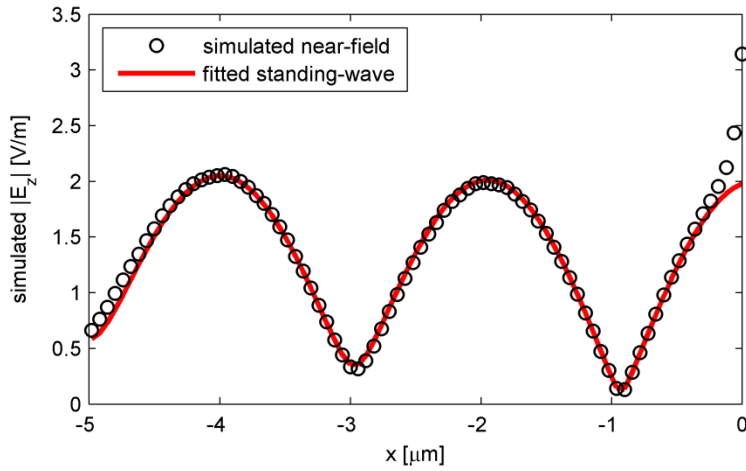


Figure 34: Simulated and fitted standing wave on open-circuited CPS.

### 3.4.2.2 Short-circuit terminated CPS

The second investigated transmission line is the dipole-coupled CPS that is terminated in a short-circuit load. The dimensions of the dipole and transmission line are identical to the open-

circuit terminated one. The end of the CPS opposite to the antenna is shorted by a 150-nm-wide gold strip that is 110 nm tall. The layout is shown in Figure 35.

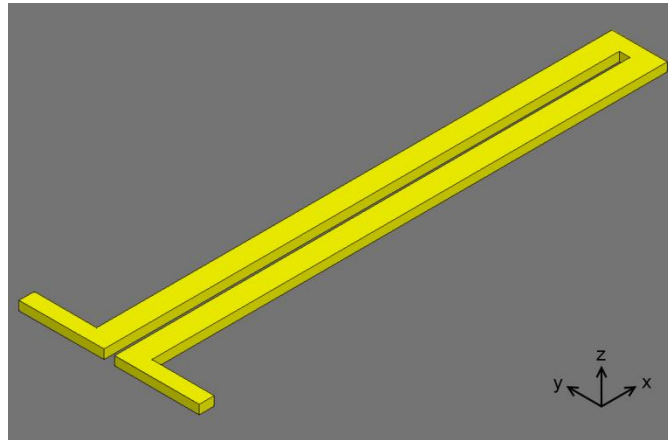


Figure 35: Layout of dipole-coupled CPS with short-circuit termination.

The simulations of the open-circuit-terminated CPS show that the incident radiation does not interact with the conductors of the transmission line. The addition of the short-circuit termination, which is a strip oriented along the same axis as the dipole antenna, changes the layout of the CPS. It is plausible that some of the incident radiation could couple through this termination onto the CPS. To investigate this possibility, the short-circuit terminated CPS without the dipole antenna is simulated. The layout is shown in Figure 36.

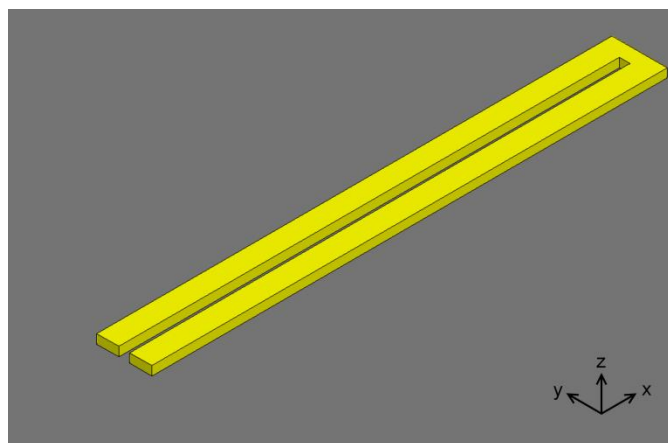


Figure 36: Layout of short-circuit-terminated CPS without dipole antenna.

The electric field 20 nm above the conductors of the dipole-coupled CPS with the short-circuit termination and the identical structure without the antenna is simulated. The magnitude of the  $E_z$  component above one of the conductors for both structures is plotted in Figure 37. The dipole is located at  $x = -5 \mu\text{m}$  and the short-circuit termination is located at  $x = 0 \mu\text{m}$ .

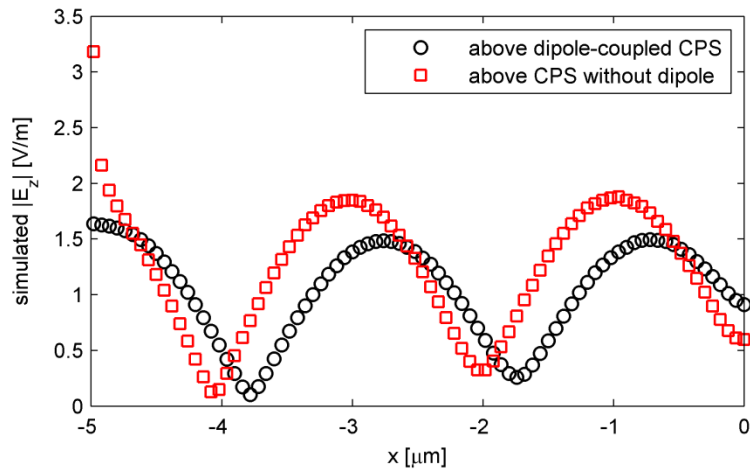


Figure 37: Simulated magnitude of  $E_z$  above one conductor of the dipole- and non-dipole-coupled short-circuit terminated CPS.

The simulated field distribution of the short-circuit terminated dipole-coupled CPS in Figure 37 resembles a standing wave, but the magnitude of the minima is increasing towards the terminated end of the CPS. The source of the additional field distribution is the short-circuit termination, which couples some of the incident radiation into the CPS. This is confirmed by the standing wave on the shorted CPS without the antenna, which is identical in shape to the standing wave on the open-circuit terminated dipole-coupled CPS in Figure 33 after taking into consideration that the source of these two standing waves are located on opposite ends of the transmission line. The identical shape of the standing waves indicates that the two transmission lines can be described by the same attenuation and propagation constants.

The field distribution on the short-circuit terminated dipole-coupled CPS is the summation of the complex electric fields that propagate along the transmission line due to radiation coupling into it through the dipole antenna on one end and through the short-circuit termination on the other end. The interference of these waves creates the field distribution shown in Figure 37. The magnitude of this field distribution is smaller than the magnitude of the standing wave on the non-antenna coupled CPS, since the interference of the two waves on the dipole-coupled CPS with the short-circuit termination is not constructive.

For the short-circuit terminated dipole-coupled CPS, the fields coupling into the transmission line through the dipole antenna create a standing wave that is expressed by Eq. (32). The standing wave that is created by radiation coupling into the transmission line through the short-circuit termination can be described by

$$E(x) = E_s \left[ e^{-(\alpha+j\beta)(5\mu m-x)} + \Gamma e^{(\alpha+j\beta)(5\mu m-x)} \right]. \quad (33)$$

$E_s$  is the magnitude of the standing wave at the location of the dipole antenna.  $\Gamma$  is the reflection coefficient for the wave reflecting off the antenna. The analytical form of the standing wave along the dipole-couple CPS is the summation of the two standing waves, Eq. (32) + Eq. (33), which is fitted to the simulated standing wave. This fit is shown in Figure 38. The parameters that are allowed to vary during the fitting process are  $\alpha$ ,  $\beta$ ,  $\Gamma$  (for both standing waves),  $E_s$  and  $E_0$ . They are summarized in Table 7.

Comparing the fitted equation to the simulated field distributions in Figure 34 and Figure 38 shows that the agreement is good throughout the transmission line, but differences are clearly visible towards the ends of the CPS where it is terminated into the dipole antenna or the load.



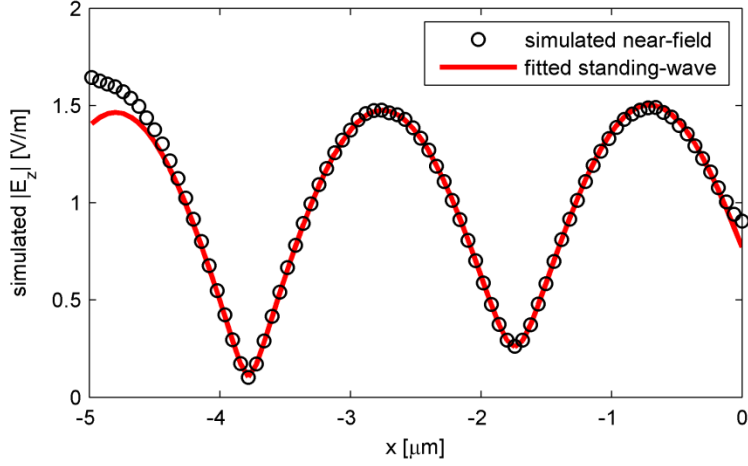


Figure 38: Fitted standing wave on short-circuited CPS.

The most likely cause of these differences is that the analytical expression assumes that the transmission line extends to  $x = -\infty$ , where the forward propagating wave originates. This is not the case for the transmission lines investigated. Due to the short length of the CPS additional reflections of the forward and backward traveling wave can occur at either end of the transmission line. Another discrepancy between the analytical model and the investigated structures is that the load is assumed to be localized at exactly  $x = 0$ . In the simulated or fabricated CPS this cannot be achieved due to the finite extent of the conductors used to create the transmission lines and the load.

Table 7: Parameters determined by fitting standing-wave equation to simulation results.

source of standing wave	reflected at	$\alpha$ ( $\mu\text{m}^{-1}$ )	$\beta$ (rad/ $\mu\text{m}$ )	$ \Gamma $	$\angle\Gamma$	$E_0$	$\angle E_0$
dipole	open	0.06	1.54	1.00	-16.5	1.0	-3.0
dipole	short	0.05	1.54	0.96	188.2	0.83	4.68
short	dipole			0.59	240.0	0.62	6.90

The analytical expression for the standing wave can be expanded to accommodate multiple reflections, which would increase the number of parameters that are varied during the fitting process. In an attempt to obtain the simplest description that fits the near-field data, the analytical model is left unchanged.

During the fitting process of the simulated open-circuit terminated CPS, the magnitude of the reflection coefficient increased to values beyond unity, representing an unrealistic situation. It was therefore limited to unity. The values of the propagation constants show great agreement. The magnitude of the reflection coefficient for an ideal open- or short-circuit load is unity, while their phase is  $0^\circ$  and  $180^\circ$  respectively. The simulated reflection coefficients generally agree with the analytical values, while only the simulated phase of the reflection coefficient of the open-circuit load shows a  $16.5^\circ$  difference, which can be attributed to the finite extent of the load. The attenuation constant of the two simulated transmission lines should be identical, but the parameters determined by the fitting process differ slightly. This is also attributed to the finite extent of the load.

To demonstrate the finite extent of the load, the simulated standing wave of the dipole-coupled open-circuit terminated CPS is fitted several times. In the original fit of the standing wave equation to the simulated near-field distribution, the location of the open-circuit load is assigned to  $x = 0 \mu\text{m}$ , which coincides with the geometrical end of the conductors of the CPS. The simulated near-field distribution is fitted repeatedly while the location of the load is shifted to locations varying around the end of the conductors of the CPS. Table 8 lists the attenuation and propagation constants as well as the magnitude and phase of the reflection coefficient for each location of the load.

Table 8: Fitted standing wave parameter to demonstrate finite extent of load.

Location of load ( $\mu\text{m}$ )	$\alpha$ ( $\mu\text{m}^{-1}$ )	$\beta$ (rad/ $\mu\text{m}$ )	$ \Gamma $	$\angle\Gamma$ (deg)
-0.2	0.065	1.531	1	-53.3
-0.1	0.062	1.534	1	-36.6
0	0.057	1.538	1	-16.5
0.1	0.056	1.539	1	1.4
0.2	0.056	1.544	1	20.5

The variation of the load location and therefore the finite extent of the load has virtually no impact on the size of the propagation constant and the magnitude of the reflection coefficient. The attenuation constant on the other hand is slightly affected by the extent of the finite load. The phase of the reflection coefficient shows an even stronger dependence on the finite extent of the load than the attenuation constant.

### 3.4.3 Device fabrication

A total of four devices are fabricated. The dipole-coupled CPS with the open- and short-circuit termination and the identical transmission lines without antennas are fabricated on a high resistivity (3 - 6 k $\Omega$ ·cm) silicon wafer. The wafer is coated with 400 nm of ZEP 520A-7 electron-beam resist. The pattern of the CPS devices is exposed using a dose of 120  $\mu\text{C}/\text{cm}^2$ , a beam current of 25 nA, and a spot size of 25 nm. The wafer is then developed in ZEP-RD for 90 seconds. The devices are metallized by electron-beam evaporating a 5-nm-thick titanium adhesion layer followed by 105 nm of electron-beam evaporated gold. The excess resist and

metal are lifted off in a methylene chloride bath. AFM topography of the fabricated CPS devices are shown in Figure 39 (a) through (d).

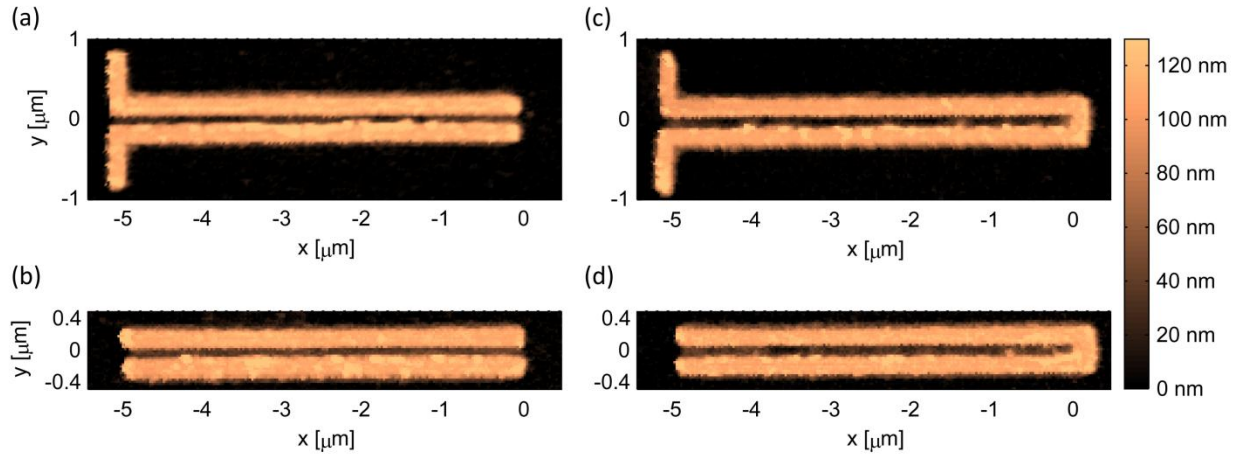


Figure 39: AFM topography of dipole-coupled CPS with (a) open- and (c) short-circuit load. Identically terminated transmission lines without dipole antenna (b) and (d).

### 3.4.4 Measurements

The near-field distribution normal to the silicon-air interface,  $E_z$ , on the four fabricated devices is measured. The recorded s-SNOM signal is plotted for the dipole-coupled open-circuit and short-circuit terminated CPS and the corresponding CPS without antennas in Figure 40.

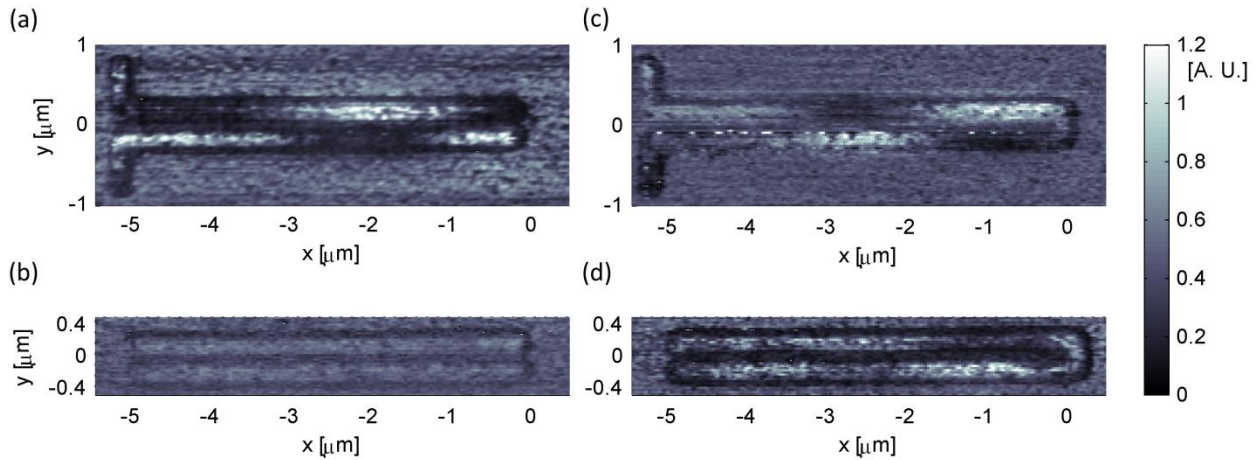


Figure 40: Measured s-SNOM signal on dipole-couple CPS with (a) open- and (c) short-circuit load and corresponding transmission lines without antenna (b) and (d).

In all of the measured near-field distributions, the  $E_z$  field distribution on one conductor is opposite to the field distribution on the other conductor of the CPS. This indicates that the measured  $E_z$  near-field component on the conductors are  $180^\circ$  out of phase, which agrees with the low frequency prediction of the field distribution along this type of transmission line in Chapter 3.4.1.3.

The measured near-field distribution above the open-circuit terminated CPS without the dipole antenna, Figure 40 (b), shows no standing wave pattern, which confirms the simulated near-field distribution in Figure 33. On the other hand, the near-field distribution above the short-circuit terminated CPS without the antenna in Figure 40 (d) indicates that the short-circuit load couples radiation into the transmission line. This has been predicted by simulations shown in Figure 37.

### 3.4.5 Data analysis

The analytical form of the second harmonic intensity signal from Chapter 3.2 is fitted to the measured s-SNOM signal. The analytical form of the s-SNOM signal includes the analytical expression of the standing wave in the near-field distribution. The attenuation and propagation constants of the CPS are determined from this fitting procedure.

Line scans are extracted from the measured data directly above the conductors of the transmission line from Figure 40. Three lines are averaged, and as an example, the result for both conductors of the open-circuit terminated dipole-coupled CPS is shown in Figure 41. The dipole is located at  $x = -5 \mu\text{m}$  and the open-circuit load at  $x = 0 \mu\text{m}$ .

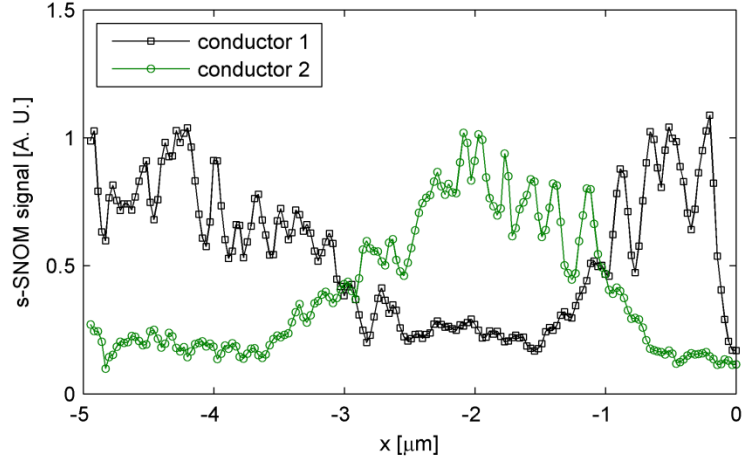


Figure 41: Measured s-SNOM signal on both conductors of dipole-coupled CPS with open-circuit load.

Three assumptions are made to aide in the analysis process. First, the tip-scattered field is equal to near-field,  $E_{\text{scat}}(z) = E_{\text{nf}}(z)$ . These two fields are actually only proportional to each other. However, in this analysis process the absolute magnitude of the fields is not of interest, but only their relative behavior is needed to determine the attenuation and propagation constants. The second assumption is that the near-field can be expressed by the standing wave equation, Eq. (32). Simulations indicate that the near-field distribution along the CPS does indeed appear to be a standing wave. Finally, the third assumption is that the magnitude and phase of the electric field in the reference arm of the interferometer,  $E_r e^{j\Phi_{\text{ref}}}$ , is constant throughout the duration of the measurement.

The detected intensity at the second harmonic of the tip-dither frequency is derived in Chapter 3.2. The analytical form of the detected signal with perfect background suppression is expressed in Eq. (26). However, the background suppression is not ideal and the detected intensity at the second harmonic of the tip-dither frequency is restated here, including a term that describes a constant offset due to some background radiation.

$$I_2 = 2E_r E_{nf} A_2 \cos(\Phi_{ref} - \Phi_{nf}) + 2E_{nf}^2 A_0 A_2 + \frac{E_{nf}^2 A_1^2}{2} + I_{DC} \quad (34)$$

The Fourier coefficients  $A_0 - A_2$  are given in Eq. (18) - (20). To compute these coefficients, the tip's oscillation amplitude,  $a = 20$  nm, the tip's closet distance to the sample,  $d = 5$  nm, and the decay length of the near-field distribution in the z-direction,  $d_0 = 35$  nm, are used.

The parameters of the standing wave equation, Eq. (32), are determined by fitting the analytical output intensity of the interferometer to the measured s-SNOM signal. Since the near-field component on top of the two conductors of the CPS are equal in magnitude, but  $180^\circ$  out of phase, the expected output intensity corresponding to each conductor is expressed as

$$I_{cond.1} = 2E_r E_{nf} A_2 \cos(\Phi_{ref} - \Phi_{nf}) + 2E_{nf}^2 A_0 A_2 + \frac{E_{nf}^2 A_1^2}{2} + I_{DC} \quad (35)$$

$$I_{cond.2} = 2E_r E_{nf} A_2 \cos(\Phi_{ref} - \Phi_{nf} + \pi) + 2E_{nf}^2 A_0 A_2 + \frac{E_{nf}^2 A_1^2}{2} + I_{DC} . \quad (36)$$

The analysis of the measured data begins with the open-circuit terminated dipole-coupled CPS, since the simulations indicate that the near-field distribution is only caused by the incident radiation coupling into the transmission line through the dipole antenna.

#### 3.4.5.1 Open-circuit terminated CPS

The analytical expressions of the s-SNOM signal, Eq. (35) and (36), is fitted to the measured s-SNOM signal on top of the two conductors of the open-circuit terminated dipole-coupled CPS. The near-field distribution used in the two equations is expressed by Eq. (32) and for reference it is restated here

$$E_{nf}(x) = E_0 [e^{-(\alpha+j\beta)x} + \Gamma e^{(\alpha+j\beta)x}] \quad (37)$$

All of the parameters in the standing wave equation are allowed to vary. The fitted second harmonic output of the interferometer and the measured s-SNOM signal is shown in Figure 42.

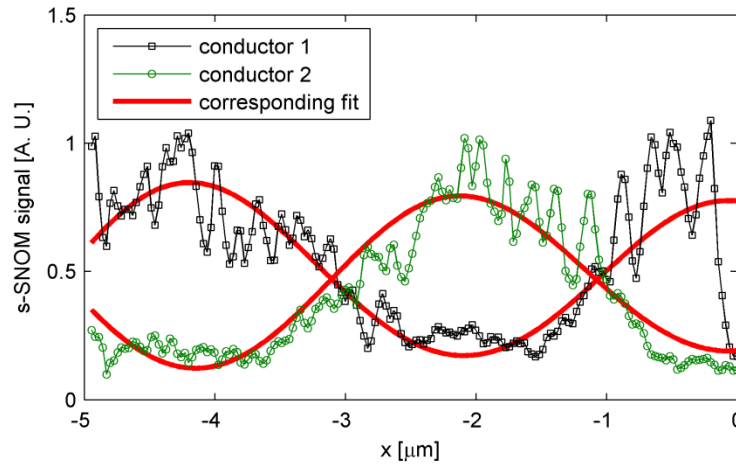


Figure 42: Analytical interferometer output fitted to measured s-SNOM signal.

The parameters of the analytical description of the s-SNOM signal that are determined by the fitting process are summarized in Table 9.

Table 9: Fitting parameters of dipole-coupled open-circuit terminated CPS.

$\alpha$ ( $\mu\text{m}^{-1}$ )	$\beta$ (rad/ $\mu\text{m}$ )	$ \Gamma $	$\angle\Gamma$	$ E_r $	$\angle E_r$	$E_0$	$\angle E_0$	$I_{DC}$
0.11	1.45	0.96	16.51	9.97	173.94	0.13	212.57	0.47

The near-field distribution along the transmission line is determined by the fitting process and it is compared to simulated near-field in Figure 43.

The measured standing wave shows a quicker decay, indicating a larger attenuation constant. The separation between maxima and minima in both standing waves agree, which means that the propagation constants of these two standing waves are similar. The peaks and



valleys in the two standing wave are shifted, which is caused by a difference in the phase of the reflection coefficient.

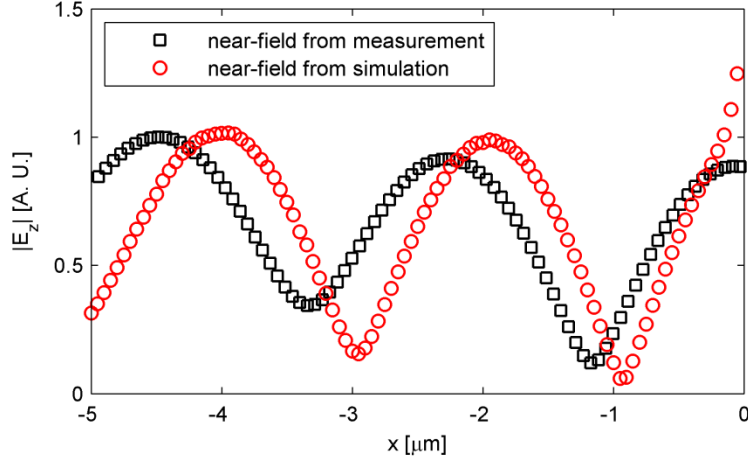


Figure 43: Measured and simulated near-field distribution along open-circuit terminated CPS.

### 3.4.5.2 Short-circuit terminated CPS

A similar procedure is used to determine the attenuation and propagation constants of the short-circuit terminated CPS. The near-field distribution on the dipole-coupled CPS is caused by the incident radiation coupling into the transmission line on one side through the dipole and on the other side through the short-circuit termination. The analytical expression of the near-field distribution is the summation of two standing waves as expressed as

$$E_{\text{nf}}(x) = E_{\text{d}}[e^{-(\alpha+j\beta)x} + \Gamma_{\text{s}} e^{(\alpha+j\beta)x}] + E_{\text{s}}[e^{-(\alpha+j\beta)(5\mu\text{m}-x)} + \Gamma_{\text{d}} e^{(\alpha+j\beta)(5\mu\text{m}-x)}]. \quad (38)$$

The first part of this equation describes the standing wave caused by the incident radiation coupling into the CPS through the dipole antenna. The propagating wave is reflected by the short-circuit termination with a reflection coefficient of  $\Gamma_{\text{s}}$ . The second part of the equation describes the standing wave created by the incident radiation coupling into the

transmission line through the short circuit termination. It is reflected at the location of the dipole antenna with a reflection coefficient of  $\Gamma_d$ .

The analytical expression of the s-SNOM signal, Eq. (35) and (36), are fitted simultaneously to the measured s-SNOM signal above the two conductors of the short-circuit terminated dipole-coupled CPS. The near-field distribution in the analytical expressions of the s-SNOM signal is expressed by Eq. (38).

The resulting fitted analytical expression of the detected intensity at the second harmonic of the tip-dither frequency is compared to the measured s-SNOM signal on the dipole-coupled CPS with the short-circuit termination in Figure 44. The dipole is located at  $x = -5 \mu\text{m}$  and the short-circuit load at  $x = 0 \mu\text{m}$ .

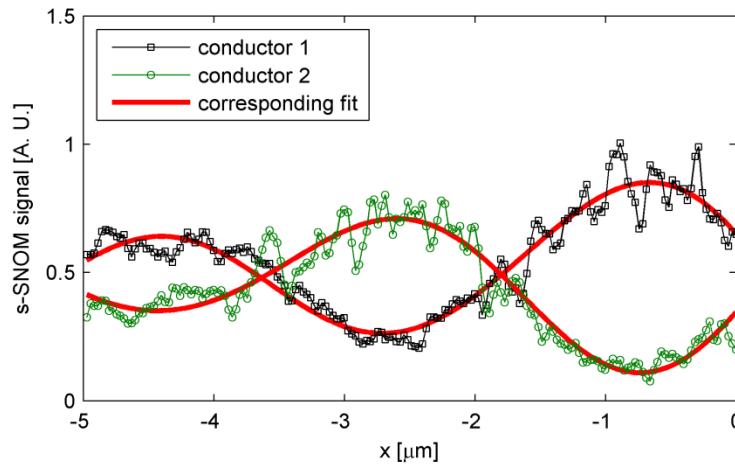


Figure 44: Analytical s-SNOM signal fitted to measurements on dipole-coupled CPS with short-circuit termination.

The parameters describing the two standing waves on the dipole-coupled CPS with the short-circuit termination are determined by the fitting process. They are summarized in Table 10.

Table 10: Fitting parameters of dipole-coupled short-circuit terminated CPS.

Wave coupled into CPS:	$\alpha$ ( $\mu\text{m}^{-1}$ )	$\beta$ (rad/ $\mu\text{m}$ )	$ \Gamma $	$\angle\Gamma$	$ E_0 $	$\angle E_0$	$E_r$	$\angle E_r$	$I_{DC}$
dipole			0.81	175.5	0.20	6.68			
short	0.07	1.43	0.78	179.7	0.33	-4.20	14.2	-21.98	0.47

The near-field distribution on the antenna-coupled CPS, which consists of the two standing waves, is determined by the fitting process and is compared to the simulated near-field distribution in Figure 45.

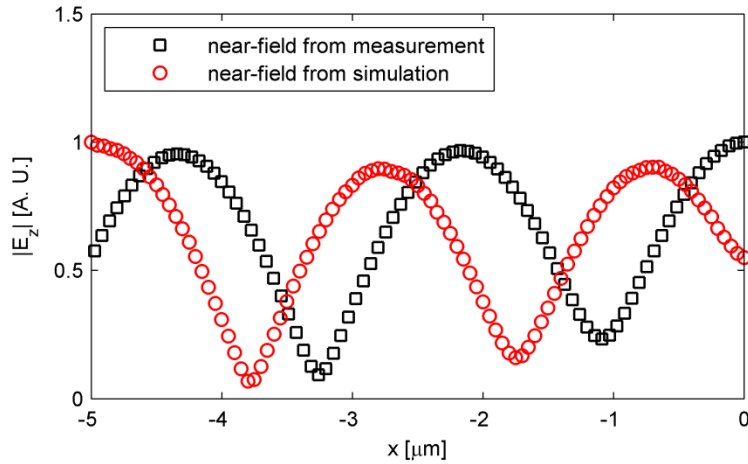


Figure 45: Measured and simulated near-field distribution along short-circuit terminated CPS.

The measured and simulated near-field on the antenna-coupled CPS are quite similar in several aspects. The separation between the minima and maxima in the standing wave pattern of the simulated and measured near-field distributions agree, indicating that the propagation constants are similar. Since this near-field distribution is composed of two standing waves, it is difficult to make assessments about the attenuation constant by merely analyzing the plot. The locations of the minima and maxima are shifted when comparing the simulated and measured

near-field distributions. This is caused by differences in the phase of the reflection coefficients that create the two standing waves.

### 3.4.6 Results

The attenuation and propagation constants of the CPS are determined by fitting the analytical equation describing the standing wave to the measured near-field data. The parameters that characterize the CPS are summarized Table 11.

Table 11: Parameters characterizing the CPS.

CPS	Standing wave	$\alpha$ ( $\mu\text{m}^{-1}$ )	$\beta$ (rad/ $\mu\text{m}$ )	$\lambda$ ( $\mu\text{m}$ )
open load	simulated	0.06	1.54	4.08
	measured	0.11	1.44	4.36
short load	simulated	0.05	1.54	4.08
	measured	0.07	1.45	4.33

The values of the propagation constant and therefore the guided wavelength obtained from the measured and simulated standing waves show good agreement. The attenuation constants show a larger discrepancy, where the measured values are larger than the simulated ones. The surface roughness of the fabricated devices, as seen in the AFM topography in Figure 39, is approximately 15 nm rms, which is much larger than the perfectly flat surfaces used in the simulation. An increase in the surface roughness will increase the attenuation of the propagating wave that is confined to a metal-air interface [59].

Reference [22] studied a similar CPS. The width of the conductors was 200 nm with a separation of 200 nm. The conductors were composed of 100-nm-thick layer of gold located on

a high resistivity silicon wafer. The attenuation of the CPS was determined to be  $0.1 \mu\text{m}^{-1}$  with a propagation constant of  $1.48 \text{ rad}/\mu\text{m}$ , which corresponds to a guided wavelength of  $4.24 \mu\text{m}$ . These values agree well with the attenuation and propagation constants determined from the near-field measurements in Table 11, further confirming that infrared transmission lines can be characterized using near-field measurements.

There are several methods to improve the CPS characterization by measuring and analyzing the near-field distribution. The angle of incidence of the Gaussian beam illuminating the antenna-coupled CPS is  $60^\circ$ . This angle is set by the measurement setup and cannot be adjusted. The radiation pattern of a dipole antenna, which is located at an air-substrate interface, shows a maximum in the direction that is normal to the interface and a minimum in the directions that are parallel to the interface. This type of antenna is therefore not ideal to couple far-field radiation into the CPS under these illumination conditions. A modified antenna design could be used to maximize the received radiation for this angle of incidence.

If the type of the antenna has to remain unchanged, the dipole length could be determined using a different approach. Instead of determining its resonance by analyzing the input impedance of an isolated antenna, the antenna-coupled CPS could be simulated for various dipole lengths while monitoring the expected near-field distribution on the transmission line. The optimum dipole length would be the one that results in the largest field distribution on the CPS. This would correspond to the antenna that most efficiently couples the far-field radiation into the transmission line.

## CHAPTER 4: CONCLUSION

Distributed response effects in infrared detectors were investigated. In particular, two detector configurations were developed that are calibrated to measure only the response component that is associated with the antenna.

The first detector investigated is composed of orthogonal dipole antennas. Two dipoles are oriented perpendicular to each other and the connections of the readout circuit form a Wheatstone bridge. The configuration of the dipole antennas and the readout circuit allows the cancellation of co- and cross-polarized response contributions stemming from the electromagnetic coupling of the signal extraction structures, the heating of the bolometer due to Joule heating caused by the bias current, or the heating of the substrate by laser irradiation. The polarization dependence of the calibrated detector was measured and showed excellent agreement with the analytical prediction.

The second detector investigated consists of a bolometer that is in the shape of a dipole antenna. The lead lines used to bias the device and extract the signal also interact with the incident radiation and contribute to the measured response. A calibration device was developed to measure this contribution. The radiation patterns of several dipole arrays were measured and after subtraction of the lead-line contribution showed excellent agreement with corresponding simulated radiation patterns that omitted the lead lines.

Analyzing the electric field in close proximity of an antenna-coupled detector can reveal the location of structures or components of the device, other than the antenna, that contribute to the measured response. In the final experiment infrared coplanar strip lines were characterized. These infrared transmission lines can play an important role in the design of more complex

detector layouts, such as phased arrays. Far-field radiation is coupled into the transmission line using a dipole antenna. The excited wave travels along the transmission line until it reaches the termination of the line, where it is reflected and propagates in the opposite direction. These two waves interfere and create a standing wave, which was measured using a s-SNOM.

One of the investigated CPS designs is terminated by a short-circuit load, which is a metal strip that is oriented in the same direction as the dipole antenna. This metal strip couples far-field radiation into the transmission line in addition to the dipole antenna. This additional source has been calibrated in the transmission line characterization process by including it in the analytical expression that describes the near-field distribution on the CPS.

The attenuation and propagation constants of the transmission line are determined by fitting the analytical form of the standing wave to the measured data. The measured propagation constants agree with the simulated ones, while the measured attenuation constants are larger than the simulated ones. This is attributed to the larger surface roughness of the fabricated samples when compared to the simulated transmission lines.

## CHAPTER 5: FUTURE WORK

The response only caused by the antenna in an antenna-coupled detector was measured using the following generalized approach. The measured quantity is a summation of a desired quantity, the antenna response, and some undesired quantities, for example the lead-line-response contribution. The measurement of only the desired quantity is not possible, but by properly designing the experiment, the undesired quantities can be measured. The desired quantity is then determined by computing the difference of the two measurements.

This approach can be used to shape the radiation pattern of an antenna or an antenna array. Measuring the radiation patterns of two properly designed devices and computing their difference could result in a narrower radiation pattern than what could be achieved by either of the two individual devices. Using this method, not only the width of the main beam of the radiation pattern but also its tilt angle could be modified.

The characterization of a single infrared coplanar strip line by measuring and analyzing the spatial near-field distribution extending along the transmission line has been demonstrated. This characterization process is still in its infancy and several improvements can be made.

The first step is the optimization of the antenna design to facilitate better coupling of incident radiation into the transmission line. The resulting field distribution will have a larger magnitude, which would enable the measuring of longer transmission lines. The standing wave pattern on longer transmission lines contains more peaks and valleys, which can remove uncertainties in the analysis of the measured data and result in more reliable values of the attenuation and propagation constants.



Several CPS layouts should be characterized once the measurement procedure has been improved. The separation, width, and height of the conductors forming the CPS, as well as the substrate material should be varied. The goal of these measurements is to minimize the attenuation of the signal propagating along the transmission line.

Other types of transmission lines should also be analyzed. The microstrip line is suggested to have lower loss at infrared frequencies than the coplanar strip line [22]. The analysis of this transmission lines should be possible using a s-SNOM, since it was demonstrated that it is not necessary to measure the guided mode directly. The fringing fields caused by the guided mode contain enough information to characterize the transmission line.

The goal of the transmission line characterization is to determine a design that has minimal loss and an optimized connection to the antenna. The integration of these optimized transmission lines have a potential impact on improved performance of future infrared detectors.

## **APPENDIX: RADIATION PATTERN MEASUREMENT**

The measurement of radiation patterns of infrared antenna-coupled detector is one method to characterize and validate the antenna design. The measurement setup is shown in Figure 1. During the radiation pattern measurement, the device is mounted on a goniometer which is rotated with respect to the incident radiation. The movement of the goniometer has five degrees of freedom. The device can be rotated and tilted and positioned along x, y, z with respect to the axis of rotation. In addition to the internal movements, the goniometer can be repositioned externally along the x, y, z directions. This external movement repositions the device and the axis of rotation simultaneously; their position relative to each other does not change.

To accurately measure the radiation pattern it is important that throughout the rotation of the device, its location always coincides with the axis of rotation and the focus of the incident laser beam. This ensures that throughout the measurement the device is illuminated by a constant irradiance. In this procedure, only the positioning of the device in the xz-plane is considered. This alignment is sufficient to measure a radiation pattern in the same plane. A graphical representation of the top view of the goniometer is shown in Figure 46.

The rotational axis of the goniometer is represented as a cross at (0,0). It forms the origin of the internal coordinate system along which the device can be moved and rotated about. The laser beam, propagating in the z-direction, and its waist are shown. For the purpose of the illustration, a large diameter beam with exaggerated divergence is shown. Its focus is located at  $(z_f, x_f)$ . The external goniometer movement will simultaneously reposition the axis of rotation and the device with respect to the focus of the laser beam.

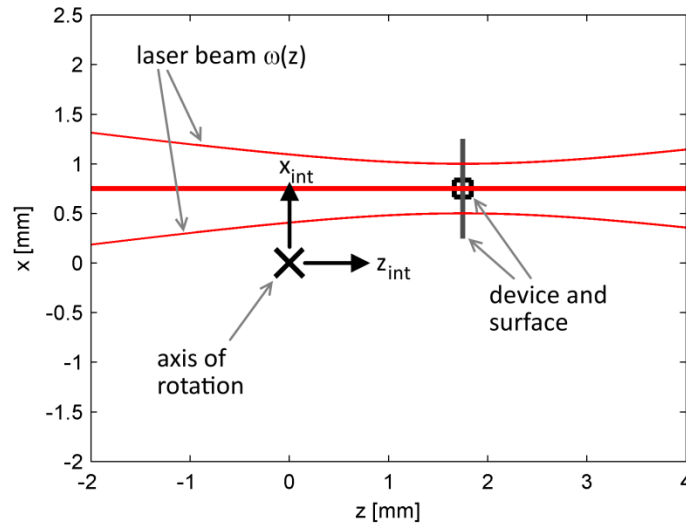


Figure 46: Top view of the goniometer indicating the location of the device, axis of rotation, and the laser beam.

The device, indicated by the black square, is mounted on the goniometer. The gray line shows the surface of the substrate on which the device is fabricated. It is parallel to the internal x-axis and indicates the rotation of the device. In Figure 46 the rotation is set to  $\theta = 0^\circ$ , and the position of the device is adjusted along the internal axes until its response is maximized. This occurs when the location of the device coincides with the focus of the laser beam, i.e.  $(z_d, x_d) = (z_f, x_f)$ .

### A.1 Alignment Process for Internal z-Axis

Initially, the device is only aligned at  $\theta = 0^\circ$ . A radiation pattern measurement would not be accurate, since rotating the device moves it away from the laser beam. The maximum amount of irradiance is illuminating the device only at broadside. This is illustrated in Figure 47 (a) and (b).

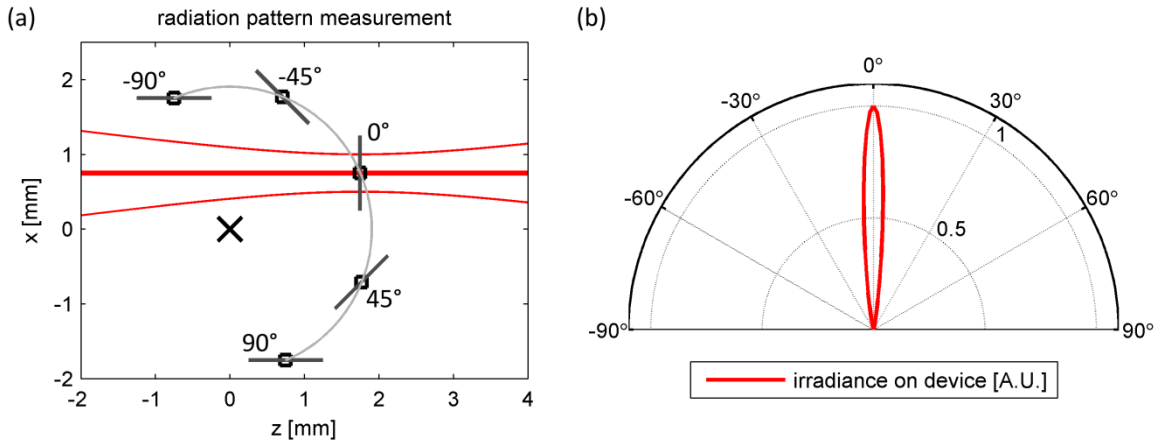


Figure 47: Radiation pattern measurement of misaligned device in x and z.

The alignment process begins by removing the offset in the z-direction between the device and the axis of rotation. A geometrical representation of the device's location with respect to the laser the axis of rotation is shown in Figure 48.

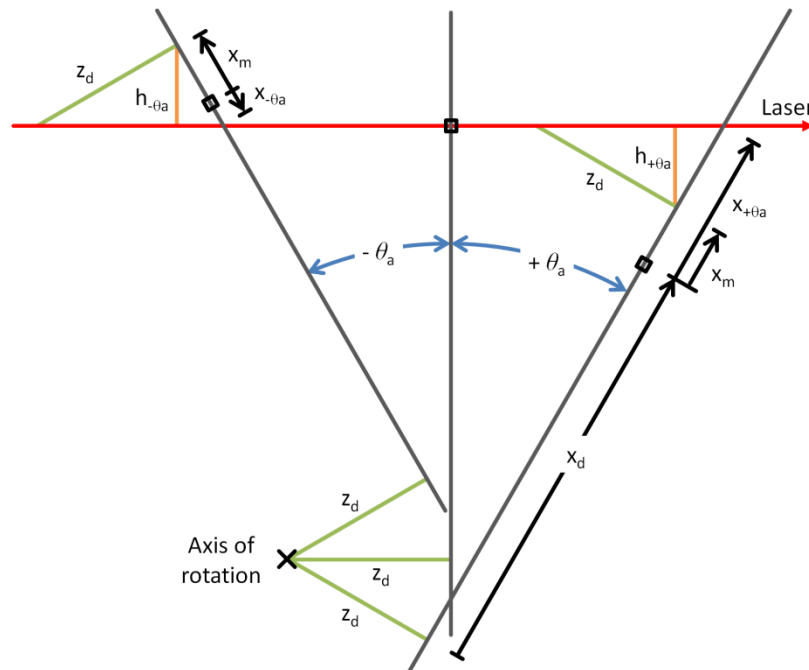


Figure 48: Geometrical representation of misaligned device in x and z is shown for  $\theta = \pm \theta_a^\circ$  and  $\theta = 0^\circ$ .

The device, indicated as a square, is located at  $(z_d, x_d)$  for three different angular rotations:  $\theta = \pm \theta_a$ , and  $\theta = 0^\circ$ . The device is misaligned in both x and z directions. Since  $h_{+\theta_a} = h_{-\theta_a}$ , it can be shown that

$$x_m = \frac{x_{+\theta_a} + x_{-\theta_a}}{2}. \quad (39)$$

If the device is positioned at  $(z_d, x_d + x_m)$  and rotated to either  $\theta = -\theta_a$ , or  $\theta = +\theta_a$ , its response will be maximized when it is displaced along the internal z-axis by  $-z_d$  to its new location at  $(0, x_d + x_m)$ .

In practice, the rotation is set to  $\theta = 0^\circ$  and the device is located at the focus of the laser beam. The goniometer is rotated to  $\theta = +\theta_a$  and the device is adjusted along the internal x-direction until its response is maximized. This occurs when the device intercepts the center of the laser beam and a maximum of irradiance is illuminating it. The direction and distance the device was moved is  $x_{+\theta_a}$ . After restoring the device to its original position the goniometer is rotated to  $\theta = -\theta_a$  and  $x_{-\theta_a}$  is determined similarly. These two steps are illustrated in Figure 49 for  $\theta_a = 40^\circ$ .

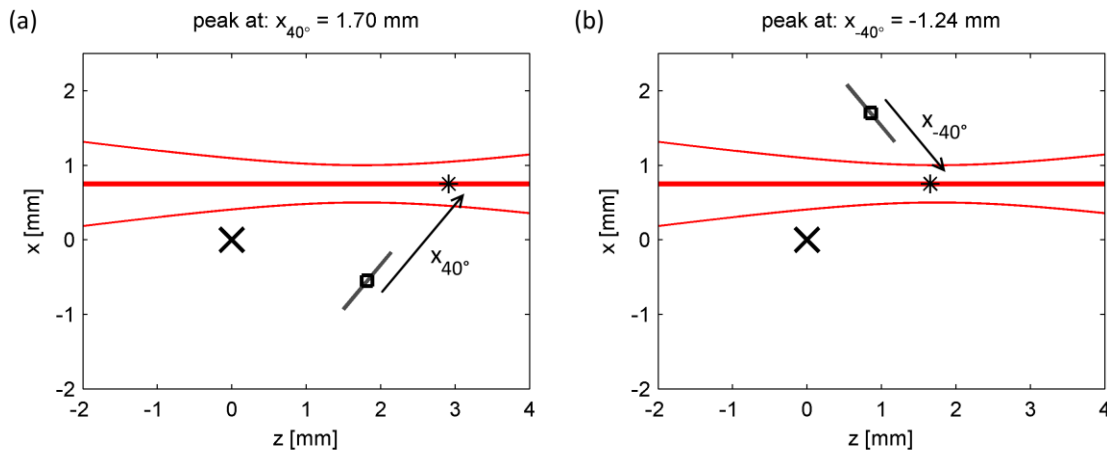


Figure 49: Position along internal x-axis to maximize response of device is determined for (a)  $\theta = 40^\circ$  and (b)  $\theta = -40^\circ$ .

The device location where its response is maximized is indicated by an asterisk. Both  $x_{+\theta_a}$  and  $x_{-\theta_a}$  are shown. While still rotated to  $\theta = -\theta_a$ , the device is moved by the distance  $x_m$ , which is calculated using Eq. (39). The device is located at  $(z_d, x_d+x_m)$  as shown in Figure 50 (a). The original device location is indicated by a gray circle and the new location is marked by the black square.

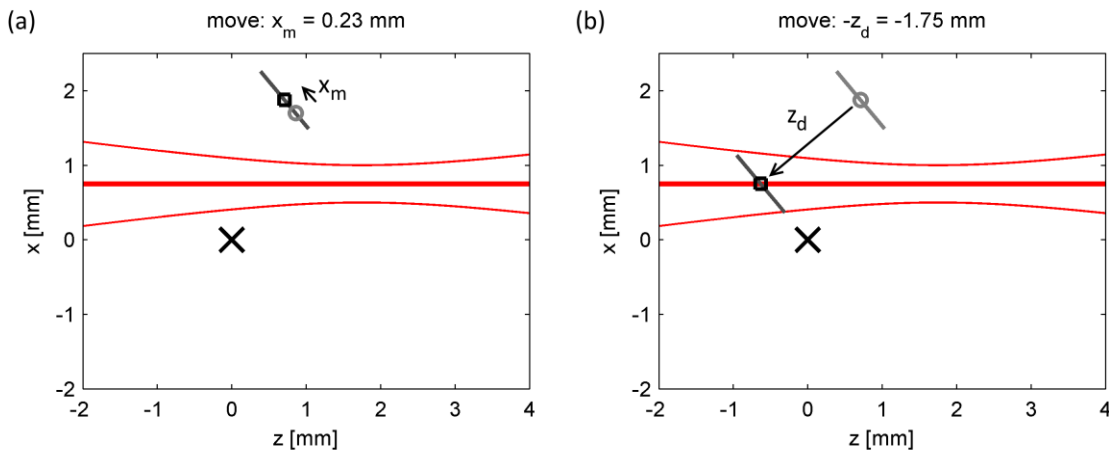


Figure 50: Adjusting (a) x and (b) z position of device.

The device is now moved along the internal z-axis until its response is maximized. As shown in Figure 48, this corresponds to the distance  $-z_d$ . The new device location, marked by square, is  $(0, x_d+x_m)$ . Its previous position is indicated with a gray circle in Figure 50 (b).

### A.2 Alignment Process for Internal x-Axis

The device is intercepting the laser beam at two angular locations,  $\theta = \pm\theta_a$ . Now, the rotation of the device would move it in and out of the beam twice. At this point, the irradiance illuminating the device is still dependent on the angle of incidence and the measured radiation pattern is not accurate as shown in Figure 51.

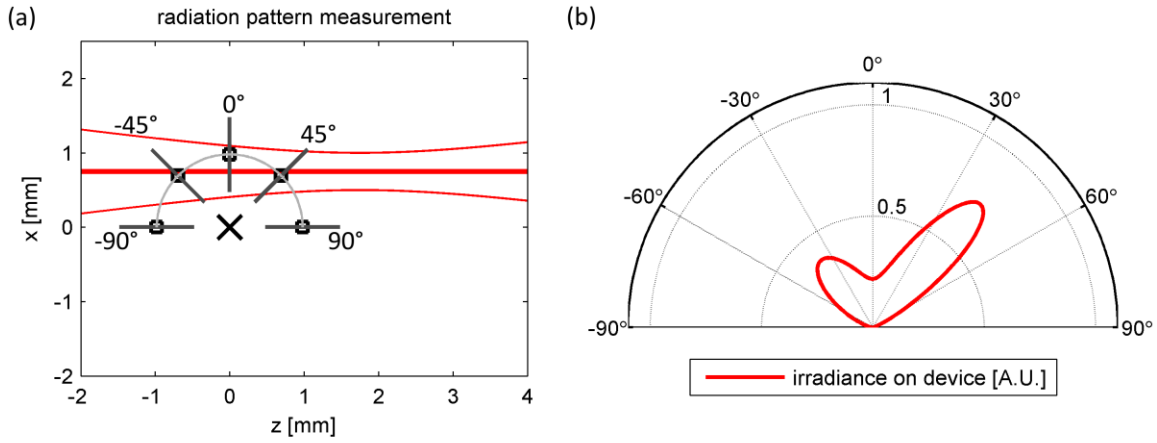


Figure 51: Radiation pattern measurement of misaligned device in x.

Figure 52 shows the geometrical representation of the location of the device with respect to the axis of rotation and the laser. The device is only misaligned in the x-direction.

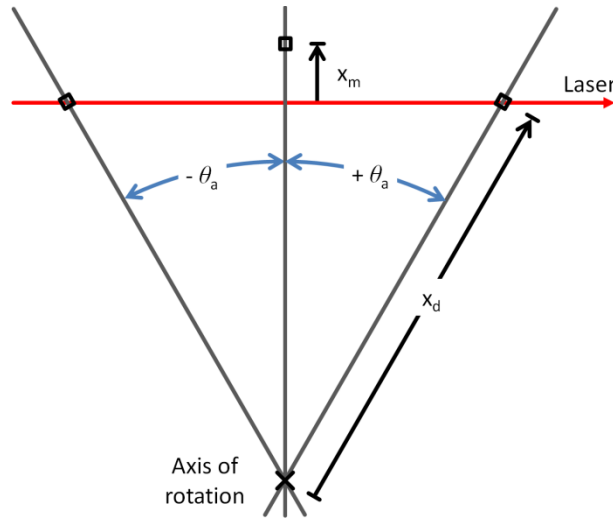


Figure 52: Geometrical representation of a misaligned device in the x direction is shown for  $\theta = \pm \theta_a$  and  $\theta = 0^\circ$ .

Figure 52 shows the laser beam intercepting the device at  $\theta = \pm \theta_a$ . The displacement of the device from the rotational axis is calculated as

$$x_d = x_m \left( \frac{\cos \theta_a}{1 - \cos \theta_a} \right). \quad (40)$$



The device is rotated back to  $\theta = 0^\circ$  where it is moved along the internal x-axis until its response is maximized. This distance is equal but opposite in direction to  $x_m$ , which was calculated during the internal z-axis alignment process. This is illustrated in Figure 53 (a). After completing this measurement, the device is moved back to its previous location  $(0, x_d + x_m)$ .

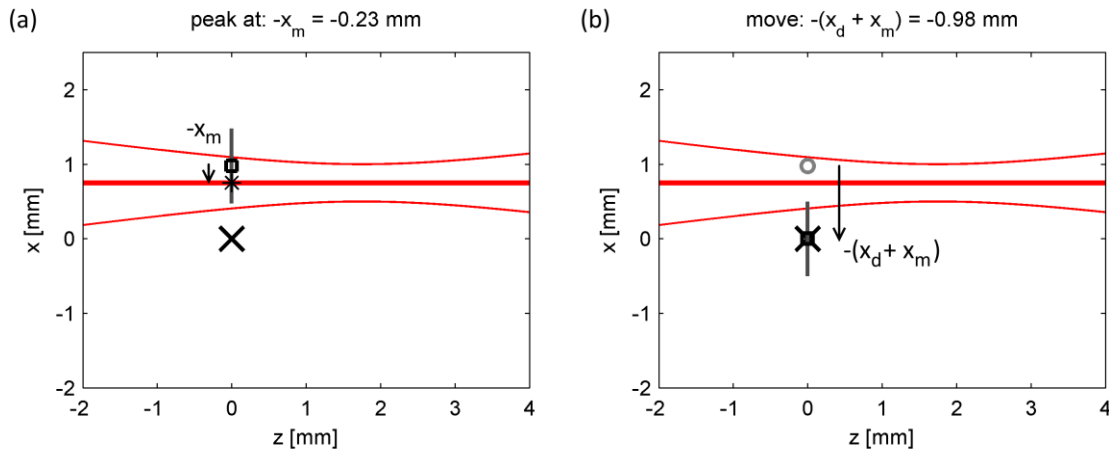


Figure 53: (a) Determine position along internal x-axis to maximize response of device at  $\theta = 0^\circ$  and (b) adjusting device's location to coincide with axis of rotation.

Using Eq. (40),  $x_d$  can be calculated and the device is moved by  $-x_d - x_m$  along the internal x-axis to its new position  $(0, 0)$ . The device and the axis of rotation are co-aligned as shown in Figure 53 (b).

### A.3 Alignment Process for External Goniometer Position

When the device is rotated, its position in space will no longer shift, since the device and the axis of rotation are co-aligned. The final part of the alignment process is to move the axis of rotation along with the device to the focus of the laser. The goniometer is moved along its external x-axis, repositioning the axis of rotation and the device relative to the laser beam, until

the device's response is maximized. This corresponds to a distance of  $x_f$ , as shown in Figure 54

(a).

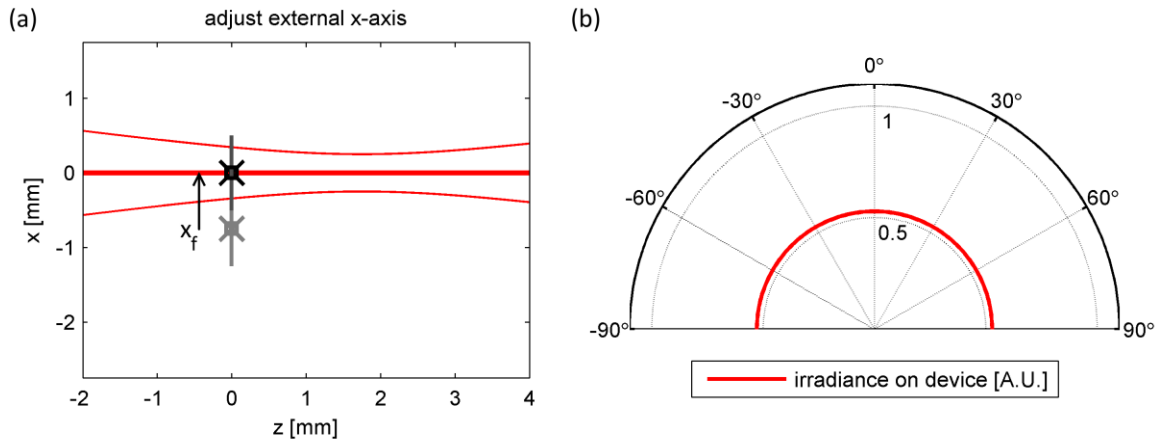


Figure 54: External goniometer adjustment (a) along external x-axis and (b) resulting irradiance illuminating device during measurement.

The device has not moved relative to the axis of rotation and is therefore still located at (0,0). The location of the focus is now located at  $(z_f,0)$  with respect to the device. At this point, a radiation pattern can be measured. A small amount of defocus will not alter the shape of the radiation pattern much. For example, displacing the device by  $\pm 1.3$  mm along the z-axis from the focus that is 230  $\mu\text{m}$  in diameter, will still illuminate the device with 90 % of the irradiance. This measured pattern is useful if only the shape of the radiation pattern is of interest. The absolute magnitude of the response cannot be measured, since the actual irradiance on the device is not known.

The goniometer is moved along the external z-axis until the response of the device is further maximized. This occurs when the device and focus are co-aligned. Figure 55 (a) shows that the device, axis of rotation, and focus are located at (0,0). If the device is rotated, it will remain in the focus of the laser and a radiometrically accurate radiation pattern can be measured

since at all times throughout the device rotation, it is illuminated by the maximum amount of irradiance as shown in Figure 55 (b).

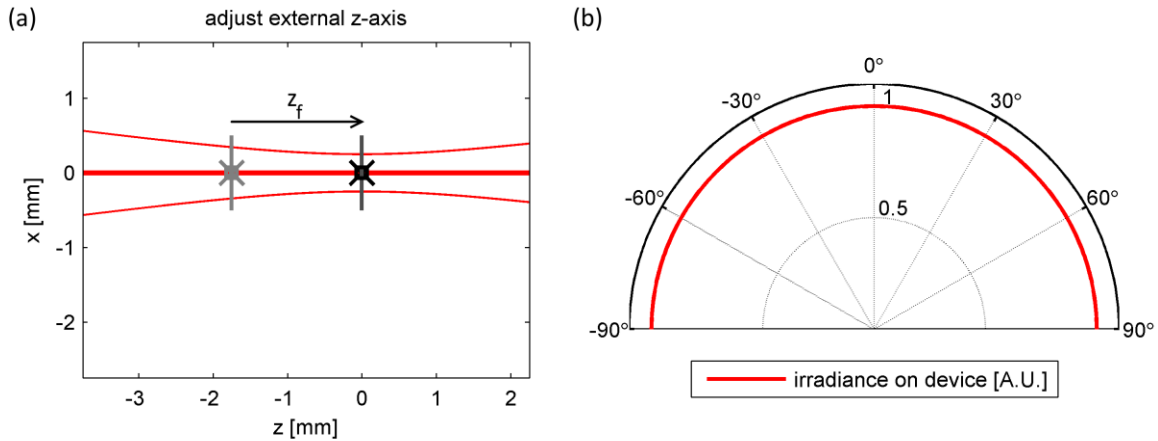


Figure 55: (a) External goniometer adjustment along external z-axis and (b) resulting irradiance illuminating device during measurement (b).

This alignment procedure assumes that the goniometer and device can be moved perfectly parallel and perpendicular with respect to each other and the laser beam. In a lab setup, such precision is difficult to achieve and the axis of the goniometer will be slightly tilted with respect to the laser. Consequently, if the position of the goniometer or the device is adjusted along the x- or z-direction, a small shift in the z- or x-direction will be introduced. After completing this alignment procedure, the axis of rotation, the device, and the laser beam will be nearly, but not quite, co-aligned. Repetition of this alignment procedure will minimize this error.

When the device is mounted in the goniometer, a small amount of tilt could be introduced, causing the substrate surface on which the device is fabricated to not be parallel to the goniometer's internal x-axis. This misalignment has no impact on the alignment procedure and the device will be co-aligned with the axis of rotation and the focus of the laser beam. However, the measured pattern will be tilted. This problem is solved by co-aligning a visible

HeNe laser with the CO<sub>2</sub> laser. By observing back reflections, it is possible to ensure that the substrate surface is perpendicular to the laser beam and therefore parallel to the internal x-axis of the goniometer.

The CO<sub>2</sub> laser power exhibits small fluctuations with time. During this alignment procedure the response of the device is used to determine the optimum position of the device. The laser power fluctuations may cause the device to indicate a maximum response when it is not positioned at the center of the laser beam. In this case, a reference power meter should be used to monitor the power fluctuations. If the responsivity of the device is linear, the measured response can be divided by the reference power. This normalized response should be used throughout the alignment procedure.

## LIST OF REFERENCES

1. W. Herschel, "Experiments on the solar, and on the terrestrial rays that occasion heat; with a comparative view of the laws to which light and heat, or rather the rays which occasion them, are subject, in order to determine whether they are the same, or different. Part I," *Phil. Trans. R. Soc. Lond.* **90**, 293-326 (1800).
2. E. L. Dereniak and G. D. Boreman, *Infrared Detectors and Systems* (Wiley, New York, 1996).
3. P. Capper and C. T. Elliott, *Infrared Detectors and Emitters: Materials and Devices* (Kluwer Academic, Boston, 2001).
4. S. P. Langley, "The Bolometer," *Nature* **25**, 14-16 (1881).
5. P. L. Richards, "Bolometers for infrared and millimeter waves," *J. Appl. Phys.* **76**, 1-24 (1994).
6. D. R. Lide, *CRC Handbook of Chemistry and Physics*, 84 ed. (CRC Press, Boca Raton, FL, 2003).
7. C. A. Balanis, *Antenna Theory: Analysis and Design*, 2nd ed. (Wiley, New York, 1997).
8. S. E. Schwarz and B. T. Ulrich, "Antenna-coupled infrared detectors," *J. Appl. Phys.* **48**, 1870-1873 (1977).
9. L. M. Matarrese and K. M. Evenson, "Improved coupling to infrared whisker diodes by use of antenna theory," *Appl. Phys. Lett.* **17**, 8-10 (1970).
10. B. L. Twu and S. E. Schwarz, "Properties of infrared cat-whisker antennas near 10.6  $\mu\text{m}$ ," *Appl. Phys. Lett.* **26**, 672-675 (1975).

11. B. L. Twu and S. E. Schwarz, "Mechanism and properties of point-contact metal-insulator-metal diode detectors at 10.6  $\mu\text{m}$ ," *Appl. Phys. Lett.* **25**, 595-598 (1974).
12. T. L. Hwang, S. E. Schwarz, and D. B. Rutledge, "Microbolometers for infrared detection," *Appl. Phys. Lett.* **34**, 773-776 (1979).
13. E. Hecht, *Optics*, 4th ed. (Addison-Wesley, Reading, Mass., 2002).
14. Y. Inouye and S. Kawata, "Near-field scanning optical microscope with a metallic probe tip," *Opt. Lett.* **19**, 159-161 (1994).
15. R. Bachelot, P. Gleyzes, and A. C. Boccara, "Near-field optical microscope based on local perturbation of a diffraction spot," *Opt. Lett.* **20**, 1924-1926 (1995).
16. M. Schnell, A. Garcia-Etxarri, A. J. Huber, K. Crozier, J. Aizpurua, and R. Hillenbrand, "Controlling the near-field oscillations of loaded plasmonic nanoantennas," *Nat. Photon.* **3**, 287-291 (2009).
17. P. Bharadwaj, B. Deutsch, and L. Novotny, "Optical antennas," *Adv. Opt. Photon.* **1**, 438-483 (2009).
18. M. Schnell, A. Garcia-Etxarri, A. J. Huber, K. B. Crozier, A. Borisov, J. Aizpurua, and R. Hillenbrand, "Amplitude- and phase-resolved near-field mapping of infrared antenna modes by transmission-mode scattering-type near-field microscopy," *J. Phys. Chem. C* **114**, 7341-7345 (2010).
19. A. Yariv, *Optical Electronics in Modern Communications*, 5th ed. (Oxford University Press, New York, 1997).
20. D. M. Pozar, *Microwave Engineering*, 3rd ed. (J. Wiley, Hoboken, NJ, 2005).

21. A. Alù and N. Engheta, "Optical nanotransmission lines: synthesis of planar left-handed metamaterials in the infrared and visible regimes," *J. Opt. Soc. Am. B* **23**, 571-583 (2006).
22. T. Mandviwala, "Transmission Lines for IR Signal Routing," (University of Central Florida, Orlando, Fla, 2006).
23. T. A. Mandviwala, B. A. Lail, and G. D. Boreman, "Characterization of microstrip transmission lines at IR frequencies - modeling, fabrication and measurements," *Microw. Opt. Techn. Lett.* **50**, 1232-1237 (2008).
24. C. T. Middlebrook, P. M. Krenz, B. A. Lail, and G. D. Boreman, "Infrared phased-array antenna," *Microw. Opt. Techn. Lett.* **50**, 719-723 (2008).
25. P. M. Krenz, J. Alda, and G. Boreman, "Orthogonal infrared dipole antenna," *Infrared Phys. Technol.* **51**, 340-343 (2008).
26. P. M. Krenz, B. A. Lail, and G. Boreman, "Calibration of lead-line response contribution in measured radiation patterns of infrared dipole arrays," *IEEE J. Sel. Top. Quantum Electron.* (accepted).
27. P. M. Krenz, B. Slovick, J. Bean, and G. Boreman, "Alignment procedure for radiation pattern measurements of antenna-coupled infrared detectors," *Opt. Eng.* **49**, 033607 (2010).
28. A. Tanaka, S. Matsumoto, N. Tsukamoto, S. Itoh, K. Chiba, T. Endoh, A. Nakazato, K. Okuyama, Y. Kumazawa, M. Hijikawa, H. Gotoh, T. Tanaka, and N. Teranishi, "Infrared focal plane array incorporating silicon IC process compatible bolometer," *IEEE Trans. Electron Devices* **43**, 1844-1850 (1996).

29. E. N. Grossman, J. A. Koch, C. D. Reintsema, and A. Green, "Lithographic dipole antenna properties at 10  $\mu\text{m}$  wavelength: comparison of method-of-moments predictions with experiment," *Int. J. Infrared Milli.* **19**, 817-825 (1998).
30. Ansoft-LLC, *An Introduction to HFSS: Fundamental Principles, Concepts, and Use* (Pittsburgh, 2009).
31. M. E. Mills, P. Townsend, D. Castillo, S. Martin, and A. Achen, "Benzocyclobutene (DVS-BCB) polymer as an interlayer dielectric (ILD) material," *Microelectron. Eng.* **33**, 327-334 (1997).
32. J. Ginn, D. Shelton, P. Krenz, B. Lail, and G. Boreman, "Altering infrared metamaterial performance through metal resonance damping," *J. Appl. Phys.* **105**, 074304 (2009).
33. J. Ginn, B. Lail, D. Shelton, J. Tharp, W. Folks, and G. Boreman, "Characterizing infrared frequency selective surfaces on dispersive media," *ACES Journal* **22**, 184-188 (2007).
34. J. Alda, C. Fumeaux, M. A. Gritz, D. Spencer, and G. D. Boreman, "Responsivity of infrared antenna-coupled microbolometers for air-side and substrate-side illumination," *Infrared Phys. Technol.* **41**, 1-9 (2000).
35. I. Codreanu and G. D. Boreman, "Influence of dielectric substrate on the responsivity of microstrip dipole-antenna-coupled infrared microbolometers," *Appl. Opt.* **41**, 1835-1840 (2002).
36. J. Alda, C. Fumeaux, I. Codreanu, J. A. Schaefer, and G. D. Boreman, "Deconvolution method for two-dimensional spatial-response mapping of lithographic infrared antennas," *Appl. Opt.* **38**, 3993-4000 (1999).



37. C. Fumeaux, W. Herrmann, F. K. Kneubühl, and H. Rothuizen, "Nanometer thin-film Ni-NiO-Ni diodes for detection and mixing of 30 THz radiation," *Infrared Phys. Technol.* **39**, 123-183 (1998).
38. C. Fumeaux, J. Alda, and G. D. Boreman, "Lithographic antennas at visible frequencies," *Opt. Lett.* **24**, 1629-1631 (1999).
39. H. Kazemi, K. Shinohara, G. Nagy, W. Ha, B. Lail, E. Grossman, G. Zummo, W. R. Folks, J. Alda, and G. Boreman, "First THz and IR characterization of nanometer-scaled antenna-coupled InGaAs/InP Schottky-diode detectors for room temperature infrared imaging," in *Infrared Technology and Applications XXXIII*, (SPIE, 2007), 65421J-65424.
40. M. Born and E. Wolf, *Principles of Optics: Electromagnetic Theory of Propagation, Interference and Diffraction of Light*, 7th ed. (Cambridge University Press, Cambridge, 1999).
41. C. Fumeaux, M. A. Gritz, I. Codreanu, W. L. Schaich, F. J. González, and G. D. Boreman, "Measurement of the resonant lengths of infrared dipole antennas," *Infrared Phys. Technol.* **41**, 271-281 (2000).
42. C. R. Brewitt-Taylor, D. J. Gunton, and H. D. Rees, "Planar antennas on a dielectric surface," *Electron. Lett.* **17**, 729-731 (1981).
43. G. J. Borse, *Numerical Methods With MATLAB: A Resource For Scientists And Engineers* (PWS Publishing, Boston, 1997).
44. L. Yanwei, A. J. Grenville, P. Yong, and H. S. Tiehan, "Generalized theory and application of Stokes parameter measurements made with a single photoelastic modulator," *J. Appl. Phys.* **100**, 063537 (2006).

45. J. S. Tharp, J. M. Lopez-Alonso, J. C. Ginn, C. F. Middleton, B. A. Lail, B. A. Munk, and G. D. Boreman, "Demonstration of a single-layer meanderline phase retarder at infrared," *Opt. Lett.* **31**, 2687-2689 (2006).
46. B. A. Lail, C. T. Middlebrook, P. M. Krenz, and G. D. Boreman, "Infrared dipole-coupled bolometer response on a hemispherical silicon immersion lens," *Infrared Phys. Technol.* **52**, 89-96 (2009).
47. M. Specht, J. D. Pedarnig, W. M. Heckl, and T. W. Hänsch, "Scanning plasmon near-field microscope," *Phys. Rev. Lett.* **68**, 476-479 (1992).
48. B. C. Wadell, *Transmission Line Design Handbook* (Artech House, Boston, 1991).
49. M. Rang, A. C. Jones, F. Zhou, Z.-Y. Li, B. J. Wiley, Y. Xia, and M. B. Raschke, "Optical near-field mapping of plasmonic nanoprisms," *Nano. Lett.* **8**, 3357-3363 (2008).
50. R. L. Olmon, P. M. Krenz, A. C. Jones, G. D. Boreman, and M. B. Raschke, "Near-field imaging of optical antenna modes in the mid-infrared," *Opt. Express* **16**, 20295-20305 (2008).
51. T. Taubner, R. Hillenbrand, and F. Keilmann, "Performance of visible and mid-infrared scattering-type near-field optical microscopes," *J. Microsc.* **210**, 311-314 (2003).
52. M. B. Raschke, L. Molina, T. Elsaesser, D. H. Kim, W. Knoll, and K. Hinrichs, "Apertureless near-field vibrational imaging of block-copolymer nanostructures with ultrahigh spatial resolution," *ChemPhysChem* **6**, 2197-2203 (2005).
53. B. Knoll and F. Keilmann, "Enhanced dielectric contrast in scattering-type scanning near-field optical microscopy," *Opt. Commun.* **182**, 321-328 (2000).

54. K. G. Lee, H. W. Kihm, J. E. Kihm, W. J. Choi, H. Kim, C. Ropers, D. J. Park, Y. C. Yoon, S. B. Choi, D. H. Woo, J. Kim, B. Lee, Q. H. Park, C. Lienau, and D. S. Kim, "Vector field microscopic imaging of light," *Nat. Photon.* **1**, 53-56 (2007).
55. A. C. Jones, R. L. Olmon, S. E. Skrabalak, B. J. Wiley, Y. N. N. Xia, and M. B. Raschke, "Mid-IR plasmonics: near-field imaging of coherent plasmon modes of silver nanowires," *Nano. Lett.* **9**, 2553-2558 (2009).
56. M. Hiebel, *Fundamentals of Vector Network Analysis*, 1st ed. (Rohde & Schwarz, Munich, 2007).
57. J.-S. Huang, T. Feichtner, P. Biagioni, and B. Hecht, "Impedance matching and emission properties of nanoantennas in an optical nanocircuit," *Nano. Lett.* **9**, 1897-1902 (2009).
58. M. Kominami, D. Pozar, and D. Schaubert, "Dipole and slot elements and arrays on semi-infinite substrates," *IEEE Trans. Antennas Propag.* **33**, 600-607 (1985).
59. D. L. Mills and A. A. Maradudin, "Surface corrugation and surface-polariton binding in the infrared frequency range," *Phys. Rev. B* **39**, 1569 (1989).